Superconducting phase coherent electron transport in nano-engineered ferromagnetic vortices

by

Richard Marsh

Department of Physics
Royal Holloway University of London

This thesis is submitted for the degree of
Doctor of Philosophy

September 2012

I, Richard Marsh, hereby declare that the work presented in this thesis for the examination of the degree of Doctor of Philosophy is my own, and work derived from other sources is clearly indicated.

Signed

Richard Marsh
September 2012

Abstract

This thesis presents an experimental study of the superconducting proximity effect in sub-micrometer sized ferromagnetic discs. Such discs belong to a class of mesoscopic ferromagnets intermediate between microscopic magnets with dimensions below about 10nm that behave as single giant spins and macroscopic structures that are larger than approximately 1μm where domains are formed to minimise stray fields. The magnetic structure of mesoscopic magnets is strongly dependent on their geometric shape, allowing for purposeful engineering of magnetic structures using modern lithographic techniques. The ground magnetic state of mesoscopic ferromagnetic discs is the magnetic vortex where unusual time-asymmetric triplet superconductivity is predicted to exist and survive up to the non-magnetic coherence length $\xi_T = \sqrt{\frac{\hbar D}{2\pi k_B T}}$ that is orders in magnitude larger than the ferromagnetic singlet coherence length $\xi_F = \sqrt{\frac{\hbar D}{2\pi k_B T_{Curie}}}$ (D is the electron diffusion coefficient). Magnetic Force Microscopy (MFM) was used to directly study the magnetic structure of the discs. To detect the proximity effect in the vortices, Andreev interferometers were used with normal parts replaced with mesoscopic ferromagnetic discs in the magnetic vortex state. The samples were fabricated using electron-beam lithography and a modified shadow evaporation technique developed within this project, allowing the whole structure to be made with highly precise alignment, without breaking vacuum and avoiding redundant ferromagnetic elements disturbing the magnetic vortices. Observations were made of superconducting phase periodic oscillations in the conductance of the Andreev interferometers described by the formula $\delta R_F = -\delta R_{0F}(1 + cos\varphi)$, where $\varphi = \frac{2\pi\Phi}{\Phi_0}$ is the superconducting phase difference, $\Phi_0 = \frac{h}{2e}$ is the flux quantum, and Φ is the magnetic flux through the area of the superconducting loop. Such oscillations provide unambiguous evidence of phase coherent electron transport through the ferromagnetic vortex. Finally, further experiments are discussed that would provide a more detailed understanding of the long range proximity effect in SFS junctions.

Acknowledgements

I am very grateful to everyone that helped me throughout my time at Royal Holloway. In particular, I would like to offer my sincere thanks to my supervisor Professor Victor T Petrashov for this fantastic opportunity, and for the continued help and guidance throughout this thesis. Your patience and timeless clear explanations have really made working with you a fascinating experience. I also owe a huge thanks for all the support I have had throughout this project from Dr Rais Shaikhaidarov and Dr Chris Checkley; your assistance both in and out the lab has been invaluable.

I am grateful for the help from the technical staff including Mr Mass Venti, Mr Andy Alway, Mr Ian Murray, Mr Howard Moore and Mr Francis Greenough for their help whenever needed in such a variety of jobs. I also appreciate the assistance from my moderator and advisor; Dr James Nicholls and Dr Stewart Boogert for their challenging questions and constructive comments at the end of every year.

I would like to acknowledge the collaboration with Dr Mikhail Kalenkov and Professor Andrei Zaikin for the theoretical contributions to this thesis, and I really appreciate the help from Dr Boris Gribkov and Dr Olga Kazakova for their knowledge and expertise in magnetic force microscopy and for helping to obtain the MFM images for this thesis. I would also like to thank Dr Roland Grein and Dr Matthias Eschrig for their help in confirming some of the particularly challenging theoretical concepts.

I would like to thank my friends that helped to make my time as a PhD student so enjoyable, for the amazing discussions within the department, and for the friendship and participation in whichever activity we set our mind to outside. My experience would not have been the same without Simon Schmidlin, Stephen Pelling, David Pavitt, Chris Harrison, Ray Davis, George Nichols, Lev Levitin, Dan Porter, Dan Hayden, Aya Shibahara, Connor Shelly, James Wells, Rob Cantrill, Kris Kent and Paco.

I would like to thank Mr Graham Fisher and Mr Craig Lucas for your friendship and amazing entertaining skills; Dr Jan Bruin and Dr Lara Torralbo for the advice

whenever needed, and Miss Sarah Robinson for her awesome proof reading skills. My secondary school physics and maths teachers Dr Price and Mr Holdaway deserves a special thanks for their passionate and interesting teaching style that played such a large role in inspiring me to continue my physics career.
Finally I owe a massive thanks to my family for everything over the past 27 years. Your advice and continued support has been nothing short of inspirational and to you, I dedicate this thesis.

Contents

List of Figures

Chapter 1

Introduction

This project benefits from working closely with both ferromagnetism and superconductivity; two remarkable subjects that have fascinated physicists since their discovery, not just because of the huge variety of uses and their future potential, but also due to the intriguing fundamental nature of both phenomena. It is worth noting the vast progression due to the exploitation of ferromagnetic properties over thousands of years, from the use of lodestone in early navigation, to the invaluable use in hard drives today, to the future opportunities in nanomagnetism [22] including the role of ultra strong permanent magnets in the making of more efficient and compact motors, the use of ultra high density media in information storage, the development of magnetic random access memory (MRAM) for instant boot up computers, and even the use of magnetic vortices for targeted cancer-cell destruction [23].

The discovery of superconductivity in 1911 was significant as it helped the transition from the classical to quantum mechanical view of the universe. However, it is the complex phenomena generated by the directly antagonistic properties at the interface of a conventional spin-singlet superconductor where the Cooper pairs are formed from electrons with anti-parallel spin alignment [24] [25], and a ferromagnet which favours electrons spins with a parallel alignment which makes this project so interesting.

Traditionally, the supercurrent penetration into a ferromagnet was thought to have been just a few nanometers due to the differential action of the ferromagnetic ex-

change field creating a spatially varying phase resulting in the oscillatory damping of the critical current. This thesis will outline the contributions to the explanation of the long range proximity effect by analysing quantum coherence effects in a ferromagnetic material that is up to two orders of magnitude longer than traditional superconductor/ferromagnetic/superconductor (SFS) systems.

The background section will introduce the previous results of SFS structures, followed by the exploration of the experiments which led to the theoretical models of spin-triplet pairing in which Cooper pairs are formed with parallel spin alignment that are insensitive to ferromagnetic exchange fields, leading to the coherence length decaying on the same length scale as spin-singlet pairs in a normal metal. This section will also explain some key experiments published recently which are endeavoring to confirm these ideas, followed by the introduction of the theoretical calculations of the critical current based on a ferromagnetic vortex in the SFS setup used in this project.

The fabrication section will discuss the techniques used to create the varying samples, highlighting the solution to the many problems encountered including an effective and unique modification to the shadow evaporation technique which has proved to be a powerful tool that shows great potential for future structures fabricated on the nanoscale.

The final sections will discuss the results taken from the variety of samples made, including the analysis of a flux biased quantum interference device which shows unambiguous evidence of superconducting phase periodic conductance oscillations due to the long range penetration of the triplet component of superconductivity that is generated due to the presence of an inhomogeneous magnetic structure at the interface of the superconductor and the ferromagnet.

Chapter 2

Background

This chapter starts with an introduction to ferromagnetism including the associated interactions, the idea of spontaneous magnetisation and domain formation. This is followed by an overview of modern developments in the field of mesoscopic ferromagnetism, including various inhomogeneous arrangements and an explanation of the magnetic vortex. It then progresses to the introduction of superconductivity and the associated phenomena, including the relation to the superconducting proximity effect in normal metals and its use in superconducting interference devices. This section then explains the traditional view of the proximity effect in ferromagnets, along with experiments revealing a particularly high superconductor induced conductance that lead to the revolution in this topic. The important theoretical contributions are discussed, followed by a set of interesting experiments which endeavour to verify this long range effect. Finally, this section explains the motivation for this thesis, including the theoretical prediction specifically involving the long range proximity effect in a magnetic vortex.

2.1 Ferromagnetism

Ferromagnetic materials have fascinated scientists since the first discovery of the material Fe_3O_4 called lodestone thousands of years ago. Ferromagnetism stands out as most materials are magnetically inactive, not because the individual atomic magnetic moments are too weak but because the moments are randomly oriented, even after the application of an external magnetic field. Ferromagnetism occurs when the atomic moments become globally ordered, which is unusual as the action of the field aligning the moments is normally overcome by the thermal disordering effect.

2.1.1 Interactions

Understanding the different types of magnetic interaction is a fundamental part of studying long range ferromagnetic order. The important interactions to note include:

Magnetic dipolar interaction

The energy of two magnetic dipoles μ_1 and μ_2, depends on their separation $\mathbf{r}$ and their degree of mutual alignment [26], represented by:

$$E = \frac{\mu_0}{4\pi r^3}\left[\mu_1 \cdot \mu_2 - \frac{3}{r^2}\left(\mu_1 \cdot \mathbf{r}\right)\left(\mu_2 \cdot \mathbf{r}\right)\right] \tag{2.1.1}$$

where $\mu_0 = 4\pi \times 10^{-7}$ is the magnetic permeability of free space. Considering two moments each of $\mu = \mu_B$ ($\mu_B = \frac{e\hbar}{2m_e}$) separated by $r = 1\mathring{A}$ the magnitude of this effect is calculated to be approximately 10^{-23}J which is equivalent to approximately 1K in temperature. Ferromagnetic materials order at much higher temperatures, so the magnetic dipolar interaction is too weak to account for the ordering of most magnetic materials.

The exchange interaction

Classical physics cannot explain ferromagnetism fully. Quantum mechanics has been needed to predict the existence of interactions between magnetic moments of neighbouring atoms causing the moments to align [27]. The mechanism of the exchange interaction originally proposed by Heisenberg in 1928 involves forces that are electrostatic in origin but due to the constraints imposed by the Pauli exclusion principle are equivalent to a very large coupling between the electron spins of the type:

$$W = -2J_{ex}\mathbf{s}_i.\mathbf{s}_j \tag{2.1.2}$$

J_{ex} is the exchange energy and is dependent on the angle between the two spin vectors. For two separate atoms with total spin vectors $\mathbf{S}_i$ and $\mathbf{S}_j$ the total interaction energy is:

$$W = -2J_{ex}\mathbf{S}_i.\mathbf{S}_j \tag{2.1.3}$$

which depends only on the relative orientation of the two total spin vectors. An immediate result from equation 2.1.3 is that the exchange interaction is reduced to zero for any closed shell of electrons, as then $\mathbf{S} = 0$. Therefore only partly filled shells are responsible for permanent magnetic dipole moments in atoms and ions. For an ion for example in the 4f group, the angular momentum $\mathbf{J}$ is a constant of the motion and therefore the projection of $\mathbf{S}$ onto $\mathbf{J}$ is a constant. The components of $\mathbf{S}$ normal to $\mathbf{J}$ precess rapidly so their contribution to the scalar product $\mathbf{S}_i.\mathbf{S}_j$ is zero on a time average. From the equivalence $\mathbf{L}+2\mathbf{S} \equiv g\mathbf{J}$ (where g is the Landé g factor), $\mathbf{L} + \mathbf{S} \equiv \mathbf{J}$. Therefore for a pair of ions:

$$W = -2J_{ex}\mathbf{S}_i.\mathbf{S}_j = -2J_{ex}(g-1)^2\mathbf{J}_i.\mathbf{J}_j = -2J'_{ex}\mathbf{J}_i.\mathbf{J}_j \tag{2.1.4}$$

which gives a coupling of the angular momentum vectors in the same form as 2.1.3 with a modified value of the apparent exchange energy. In a solid, each magnetic ion is surrounded by other magnetic ions with each of which it will have

an exchange interaction. The total interaction will therefore be a sum of the terms taken over all pairs of ions. The energy for atom i is therefore:

$$W_i = -2\mathbf{J}_i . \sum_j J'_{ex\,ij}\mathbf{J}_j \tag{2.1.5}$$

The magnetic dipole moment of each ion is proportional to the angular momentum $\mathbf{J}$, since $\mathbf{m} = g\mu_B\mathbf{J}$ so the exchange energy can be expressed in terms of the dipole moments giving:

$$W_i = -2\left(\frac{\mathbf{m}_i}{g\mu_B}\right) . \sum J'_{ex\,ij}\left(\frac{\mathbf{m}_j}{g\mu_B}\right) \tag{2.1.6}$$

In a ferromagnet or a paramagnet in an external field, each ion will have an average dipole moment in the direction of the magnetisation, together with fluctuating components in other directions whose time average is zero. In summing over the interaction with neighbouring ions, the fluctuating components will average out. To a fair approximation, the vector sum over the neighbouring dipole moments can be replaced by a sum over the average moment per neighbour $\bar{\mathbf{m}}_j$ and assuming that the only important interaction is with z equidistant neighbours, each with the same interaction energy J'_{ex}, then:

$$\begin{aligned} W &= -2\left(\frac{\mathbf{m}}{g\mu_B}\right) . \sum J'_{ex}\left(\frac{\bar{\mathbf{m}}_j}{g\mu_B}\right) \\ &= -2\left(\frac{\mathbf{m}}{g\mu_B}\right) . \left(\frac{z\bar{\mathbf{m}}}{g\mu_B}\right) J'_{ex} \\ &= -\left(\frac{2zJ'_{ex}}{ng^2\mu_B^2}\right)\mathbf{m}.\mathbf{M} \\ &= -\mathbf{m}.\mathbf{B}_{int} \end{aligned} \tag{2.1.7}$$

The subscript i has been dropped as all ions are identical and the energy is the same for each, and the mean moment per ion is replaced by the magnetisation $\mathbf{M} = n\bar{\mathbf{m}}$ where n is the number of ions per unit volume. The result is an equation formally identified with the potential energy of a dipole $\mathbf{m}$ in a field:

$$\mathbf{B}_{int} = \left(\frac{2zJ'_{ex}}{ng^2\mu_B^2}\right) = \lambda\mathbf{M} \tag{2.1.8}$$

The effect of the exchange forces can be represented by an effective 'internal field' of flux density $\mathbf{B}_{int}$, which is proportional to the intensity of the magnetisation. This concept was first introduced by Weiss and is explained further in the spontaneous magnetisation subsection below.
Quantum theory explains why there are so few ferromagnetic elements. For a material to be ferromagnetic a large enough atomic magnetic moment must exist, and few electronic configurations permit this. For ferromagnets, the coupling energy must have a sign that would be energetically favourable to make the moments parallel, and finally this energy must be great enough compared to the energy of thermal agitation k_BT for the alignment of moments to remain at room temperature.

Magnetocrystalline anisotropy

Along certain crystallographic directions, it is easier to magnetise a crystal (known as the direction of easy magnetisation) and is harder along other axes. The excess energy required to magnetise the substance in the hard direction is called the magnetocrystalline or anisotropy energy, and is therefore larger in lattices of low symmetry such as cobalt with its hexagonal structure and smaller in lattices of high symmetry such as nickel (fcc structure) and iron (bcc structure). The anisotropy energy arises from the spin-orbit interaction and the partial quenching of the angular momentum. It is clear that the anisotropy energy cannot arise from the exchange interaction, as the exchange interaction depends only on the mutual orientation of the dipoles and not the angle which they make with the crystal axis.

2.1.2 Spontaneous magnetisation

Better alignment can be achieved by lowering the temperature or increasing the size of the applied magnetic field, however ferromagnetic materials such as nickel, cobalt and iron have a net magnetisation at room temperature and in zero field, so the cause of the atomic moment alignment is the first obvious question to ask. In 1910 P. Weiss suggested the theory for ferromagnetism, and suggested there was a much stronger magnetic field created by the material which Weiss called

the molecular field, however due to the nature of metallic materials a more correct nomenclature is the mean field approximation. The molecular field is parallel to the direction of the magnetisation **M**, and **H** is proportional to the magnetisation M (defined as the magnetic moment per unit volume). The effective field in the solid is therefore $H + \lambda M$ (λ is a constant, independent of temperature) which when combined with Curie's law:

$$\mathbf{M} = \frac{C\mathbf{B}}{T} \tag{2.1.9}$$

gives

$$\frac{M}{H + \lambda M} = \frac{C}{T} \tag{2.1.10}$$

which can be re arranged to give the Curie-Weiss law:

$$\chi = \frac{M}{H} = \frac{C}{T - \lambda C} = \frac{C}{T - T_C} \tag{2.1.11}$$

where **B** is the magnetic field, T is the absolute temperature, C is the material specific Curie constant, χ is the magnetic susceptibility (a dimensionless proportionality constant that indicates the degree of magnetisation of a material in response to an applied magnetic field) and $\lambda C = T_C$, the Curie temperature. The Curie temperature or Curie point is the temperature above which the spontaneous magnetisation vanishes. It separates the disordered paramagnetic phase when $T > T_c$ from the ordered ferromagnetic phase when $T < T_C$.

From the Curie-Weiss law, the susceptibility has a singularity when $T = T_C$. This means at this temperature and below, if the external field tends to zero the magnetisation can be non zero which gives rise to the spontaneous magnetisation of ferromagnetic materials. The Currie temperature is material specific, as shown for Nickel, Cobalt and Iron in table 2.1, and plays an important role in the theory described in the later subsection.

Table 2.1 shows the Curie temperature of nickel which is an approximation of the temperature at which the interaction between neighbouring nickel ions is of the order $k_B T$, whereas the magnetic interaction of two atomic dipoles at this distance

Metal	Curie Temperature (K)
Nickel	631
Iron	1043
Cobalt	1394

Table 2.1: Curie temperature for Nickel, Iron and Cobalt

would be equivalent to $k_B T$ with T less than 1K.

2.1.3 Domains

If a ferromagnetic material in the atomic scale contains magnetic moments which are aligned parallel to each other, it seems contradictory that it is possible for a ferromagnet to have no overall magnetic moment in zero field at room temperature. This problem was tackled by Weiss, suggesting the idea of dividing the material into regions called domains of at least a few microns in size. Internally, the magnetisation in each domain is saturated but the directions of magnetisation of each domain vary so the magnetic moment of the bulk crystal is zero. This idea was later validated with the Bitter experiment by using a polished surface of iron covered with a think layer of liquid that contained a suspension of fine magnetic particles [28]. At the boundary of two domains with different orientations, near the surface of the metal there exists a magnetic field localised along the wall. This field attracts the particles making the domains visible as seen in figure 2.1.

Figure 2.1: Image highlighting large grain domain formation on an iron based sample using the Bitter technique with a magnification of approximately x2

Landau and Lifshitz showed that the domain structure is a natural consequence of the various contributions to the energy; the exchange, anisotropy and magnetic

dipolar interaction of a ferromagnetic material. The stray magnetic field created by the magnetised domains outside the material has a certain energy with the density proportional to $\mathbf{B}^2$, and the domains are arranged to minimise this energy. Figure 2.2 (a) shows a structure with a single domain. As a consequence of the magnetic 'poles' formed on the surfaces of the crystal, this arrangement will have a high magnetostatic energy. This energy can be halved (and further reduced to approximately $\frac{1}{n}$ by dividing this into n domains) by arranging the domain into two anti-parallel domains, and therefore reducing the spatial extension of the field as in figure 2.2 (b). With certain arrangements the domains can be formed so the lines of magnetic field emerging into the region outside the material are turned back into the interior, therefore producing no external field and reducing the magnetic energy such as in figure 2.2 (c), and is called the domains of closure.

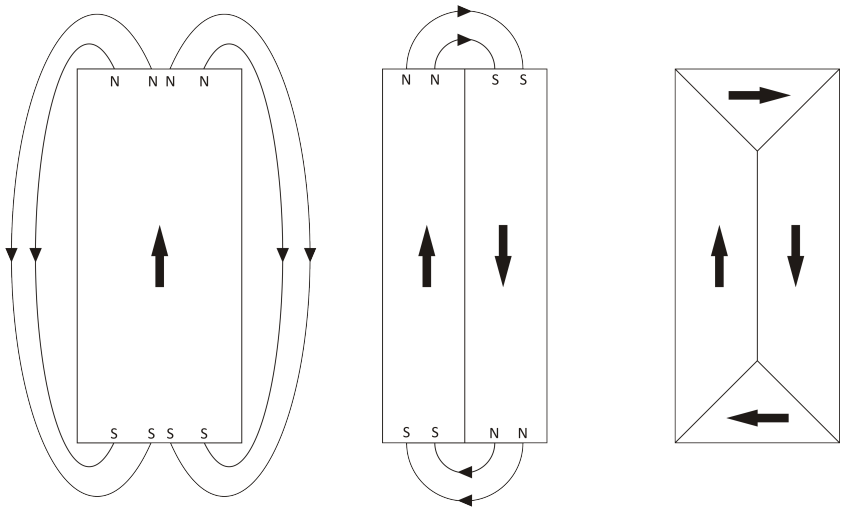

Figure 2.2: Figure showing variations in domain arrangement with associated stray field, including the single domain, double domain, and closure domain.

The transition layer that separates adjacent domains magnetised in different directions is called the domain wall. The change in spin directions between domains does not occur instantly across a single plane, but takes place gradually over many atomic planes as the exchange energy is lower when the change is distributed over many spins. The wall would thicken without limit in the absence of the anisotropic energy which acts to limit the width of the transition layer. The spins contained within the wall are largely directed away from the axes of easy magnetisation so there is an anisotropy energy associated with the wall, roughly proportional to the

wall thickness. Within the magnetic domains of a ferromagnet, the magnetisation lying along the easy direction is energetically favourable, but in the wall it will have to rotate and the component will lie across the hard axis which will cost energy.

The domain wall has a finite thickness extending over a number of atoms whose spins change gradually in direction. The most common type of wall is the Bloch wall in which the magnetisation rotates in a plane parallel to the plane of the wall. Another possible configuration is the Néel wall, in which the magnetisation rotates in a plane perpendicular to the plane of the wall. The type of wall formed is dependent on the magnetostatic energy, with the Bloch wall being favoured in the bulk as it leads to a smaller dipolar energy, and the Néel wall being favoured in thin films where there is a dipolar energy cost to rotate the spins out of the plane of the film. The volume occupied by the domains of closure decreases as the width of the domain decreases, and the anisotropy energy therefore tends to reduce the domain size, while the wall energy tends to increase it. The optimum domain size is determined by a compromise between these two effects. In the same way that the size of the domain wall is a balance between the exchange and anisotropy energy, the formation of a domain is a balance between the cost of the demagnetising field and the cost of a domain wall. For nickel, the number of atoms in the thickness of the wall is in the order or 100 and the thickness of the wall is a few tens of nanometers [29].

2.2 Inhomogeneous magnetic structures

Recent developments in fabrication and imaging technology have enabled the study some interesting ferromagnetic structures when limited to the mesoscopic scale. A few of these inhomogeneous structures have been used recently in the search for the long range proximity effect which are discussed in the later subsection, however the various magnetisations with their associated advantages and disadvantages are discussed below.

2.2.1 Intrinsic inhomogeneous magnetic structures

Holmium is an appealing material to use as it has an intrinsic inhomogeneous structure, the conical magnetic ordering produces a net ferromagnetic component in the c-axis, and its magnetic properties are robust even in thin films. Figure 2.3 shows the magnetic structure of holmium, revealing its conical shape with the magnetisation **M** rotating by 30^o per atomic plane and at an angle of 80^o to the c-axis with a net moment of 1.7 μ_B per atom. The biggest issue with holmium in the search for the proximity effect, is its inability to change the magnetisation in situ, which would be a powerful tool considering the importance of the magnetisation on triplet formation.

The inhomogeneous ferromagnet used for the experiment by Keizer *et al.* [2] involved a layer of CrO_2 which is well known for its use in magnetic recording tapes. The important feature used for this experiment is that the magnetic behaviour has been shown to be single domain like, even for macroscopic films. The band structure of this material is shown in figure 2.4 and shows that the electronic transport is metallic for the spin-up electrons, and insulating for the spin-down electrons. It is the nature of this structure that suggests the singlet to triplet conversion occurs at the S/F interface.

Another form of inhomogeneity mentioned involved the multi-layered samples used in figure 2.25 from a later subsection. This experiment involved two sources of non collinear magnetisation; between the adjacent layers of PdNi and the non collinear magnetisation between the PdNi layer and the cobalt layer. The domain size of PdNi is not yet known, however it is thought that the competition between the out of plane magnetocrystalline anisotropy and the in plane shape anisotropy of thin films can lead to stripe domains and therefore to non-collinear magnetisation between neighbouring domains. The benefit of this structure, is the comparison to the s/f'/f/f'/s junctions suggested by [15], and the potential of variations in the relative layer magnetisations.

It is important to note that despite not being shown in experiment yet, it has been suggested that any spin active interface between a superconductor and a ferromagnet can generate the spin triplet correlations [30], however the magnetisation from

the domain wall from cobalt is not enough to produce a significant amount of triplet correlations.

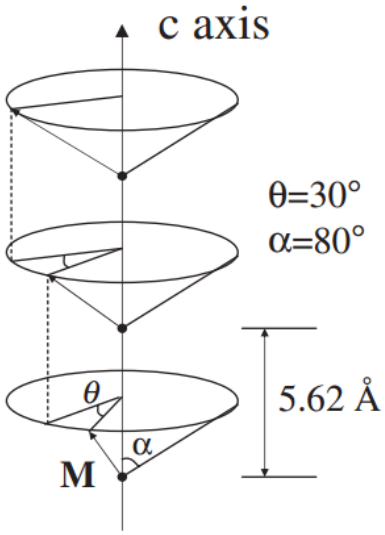

Figure 2.3: Magnetic structure of holmium as used in [1] showing the intrinsically inhomogeneous structure below the Curie temperature of 21K.

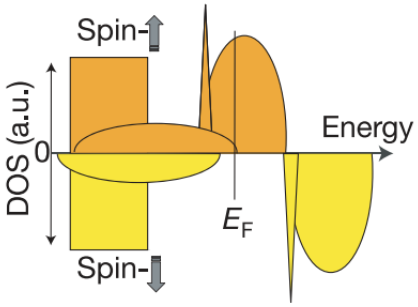

Figure 2.4: Spin dependent density of states (DOS) for CrO_2 taken from [2]

2.2.2 Mesoscopic ferromagnetism: the magnetic vortex

Recent progressions in nanotechnology have lead to the observation of an interesting magnetic structure when a ferromagnetic sample is reduced to the mesoscopic scale. These samples are intermediate between microscopic samples with dimensions below 10nm that behave as single giant spins and macroscopic samples above approximately 1μm where the ferromagnetic sample will form domains to reduce

the magnetostatic energy at the cost of a domain wall. As a result of the competition of the dipole, exchange, and anisotropy contribution to the energy, the magnetic structure of mesoscopic magnets is strongly dependent on their shape. This enables the magnetisation of samples to be engineered using modern lithographic techniques, with the ground magnetic state of mesoscopic discs being the ferromagnetic vortex, a schematic diagram of which can be seen in figure 2.5. The spins lie in plane, changing directions gradually so lost exchange energy is minimised and to cancel the total dipole energy. At the centre of the disc the distance between opposite spins decreases greatly when confined in plane, so the magnetisation of the core will turn out of plane so that the spins are parallel to the plane normal as a result of the short range exchange interaction. The vortex with its intriguing core has been predicted theoretically for many years, but only observed experimentally after recent advances in technology as the width of the core is approximately 10nm. The first observation was in 2000 [4] using a magnetic force microscope (MFM) on permalloy ($Ni_{80}Fe_{20}$) discs up to 1μm in size, and shows clear evidence for the existence of a vortex spin structure with the perpendicular core as seen in figure 2.6. The MFM suffers restrictions from the lateral resolution of approximately 20nm which is larger than the vortex core; the magnetic stray field of the tip can interfere with the disc; and the sensitivity is restricted to the out of plane component of the stray field gradient. The paper by Wachowiak *et al* [3] uses spin polarised scanning tunneling microscopy (SP-STM) on iron islands to probe the core itself. All three problems are avoided, as the SP-STM can resolve structures down to the atomic scale, any dipolar interaction between tip and sample can be avoided with the use of anti-ferromagnetic probe tips, and by varying the thickness of the anti-ferromagnetic layer the tips can be prepared with in plane or out of plane sensitivity so they can probe the core with one orientation, or reveal lateral width, shape, and magnetic field dependence with the other. The core orientation being either up or down is energetically equivalent so is randomly distributed, and is an interesting structure showing promising signs for being a candidate for future non volatile data storage devices [3]. It is important to note a single domain will form when the disc thickness is a lot smaller than the disc

diameter, which has been shown experimentally with discs just a few nanometers thick [31].

Studies on the stability of a magnetic vortex shows the significance of two characteristic length scales. The first dimension to note is the single domain radius R_{EQ}, which is the radius of the ferromagnetic cylinder where the energy of the uniformly magnetised state is the same as the vortex state. If the cylinder has a radius less than R_{EQ}, the uniformly magnetised state has a lower energy, however metastable vortices may form.

The second dimension to note is the absolute single domain radius R_S in which the vortex state is strictly prohibited if the cylinders' radius is below this value. The rigorous calculation of R_S is currently beyond the possibilities of analytical methods, however estimations are made by considering a cylinder in the vortex state and decreasing the radius until the largest absolute single domain radius is reached. These dimensions are considered in terms of the exchange length, L_E, which is the length scale over which the direction of the magnetisation does not change significantly, as the exchange energy is the dominant component and can be calculated as approximately 10nm using $L_E = \sqrt{\frac{2A}{\mu_0 M_S^2}}$ (where $A = 9 \times 10^{-12} JM^{-1}$ is the exchange constant [32], $\mu_0 = 4\pi \times 10^{-7} \mathrm{H}m^{-1}$ and $M_S = 5 \times 10^5 Am^{-1}$ is the saturation magnetisation of nickel).

The stability of the vortex has been considered both theoretically [33] [34] and experimentally [35] [36] [37] and the corresponding magnetic phase diagrams show the discs used within this project are clearly above this limit.

The vortices not only have a fascinating magnetic structure, but are a promising candidate for future non volatile data storage devices, and are predicted to observe novel transport properties [38] [39]. The biggest benefit of this magnetic structure in comparison with the samples discussed above in terms of this topic, is the ability to change the magnetisation by applying an external magnetic field, meaning the disc can be in one of two magnetic states at zero field. This property is discussed in the next subsection and will play a critical role in the results chapter.

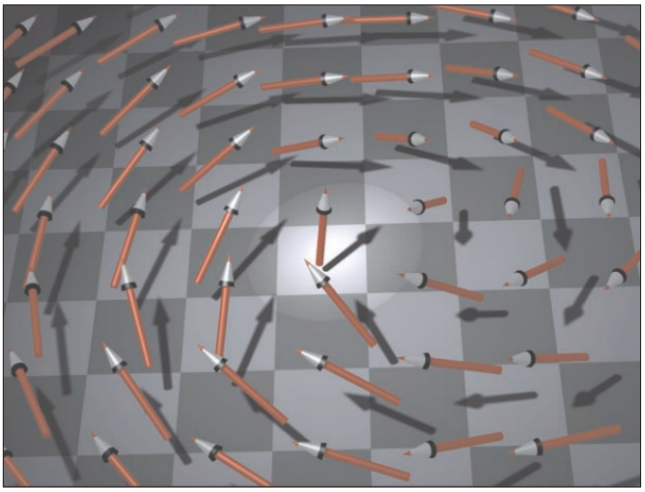

Figure 2.5: Schematic of a vortex core taken from [3]. The important features to note is the curling magnetisation parallel to the plane of the disc, and the highlighted core in the centre with perpendicular magnetisation.

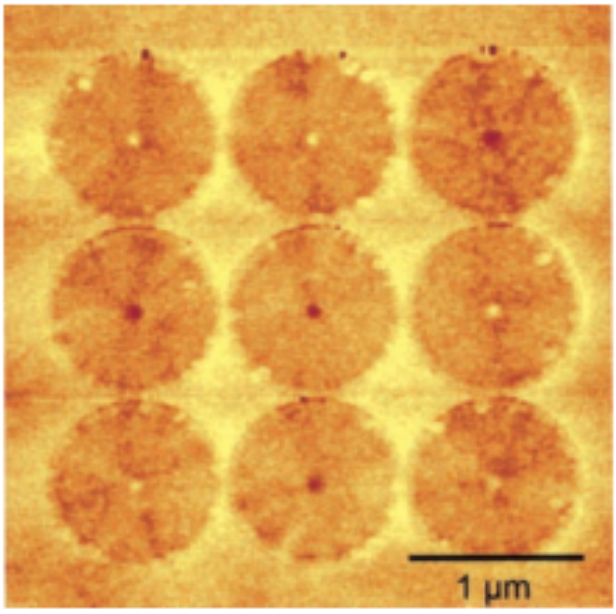

Figure 2.6: MFM images taken from [4] of an array of ferromagnetic discs made of permalloy 1μm in diameter and 50nm thick.

2.2.3 Mesoscopic ferromagnetism: the magnetic antivortex

As the magnetic structure of mesoscopic magnets is strongly dependent on their shape, the nanoengineering of various magnetic structures using modern nanolithography techniques opens the potential to investigate many SFS structures

such as the topological counterpart to the vortex; the ferromagnetic antivortex. The first single antivortex state nanomagnets suitable for measurement came from samples fabricated at Royal Holloway in the form of cobalt crosses with 1μm branches and 40nm thick [5]. Further micro modeling (see subsection below) and MFM imaging revealed the new structure which is shown in figure 2.8 and 2.7. This stable formation was realised on asymmetric crosses during magnetisation reversal in an external magnetic field.

To realise the antivortex state, a strong ($63.7 \times 10^3 Am^{-1}$) magnetic field was applied along the nonsymmetrical diagonal of the cross, forming quasiuniform magnetisation. A weak reversed magnetic field of $19.9 \times 10^{-3} Am^{-1}$ was applied which then transitioned the structures into the antivortex state with a characteristic four-pole symmetry. Increasing the external magnetic field revealed the transition to antivortex states on all of the structures, as shown by the steps in figure 2.7 (b).

The antivortex is an interesting magnetic structure, and is expected to show unusual transport properties in an applied magnetic field including the relatively new phenomenon of the topological Hall effect [40], and shows promise for investigations of transport peculiarities and magnetodynamical phenomena specific to inhomogeneous magnetic systems. This structure is particularly interesting as this enables a wider variety of magnetic structures to be tested in the SFS configuration, with a similar result expected as the physics of the system is related and with the technology and knowledge developed within this thesis would be a relatively straight modification to make.

2.2.4 Micro-magnetic simulations

The importance of mesoscopic ferromagnets can be seen in uses from fundamental research to data storage devices, together with progressive fabrication technology has lead to the development of micro-magnetic simulations to compute the magnetisation of mesoscopic magnets enabling comparison of the theoretical and experimental images produced by the high resolution imaging technology. The Object Oriented Micro Magnetic Framework (OOMMF) project of the mathematical and computational sciences division of the Information Technology Laboratory at

the National Institute of Standards and Technology [41] was designed as a micromagnetic package showing the magnetic moments of a 3-dimensional object in a 2-dimensional vector field. After defining material parameters, geometry, initial magnetisation, anisotropy, and the time evolution of the external magnetic field, the OOMMF solver utilises a Landau-Lifshitz ordinary differential equation solver to relax 3D spins on a 2D square mesh, using fast Fourier transforms to compute the magnetostatic field. The magnetic structure of a nickel disc 300nm in diameter and 30nm thick, with a random initial magnetisation and without an applied external magnetic field can be seen in figure 2.8 (b). The important features to note are the curling configuration, and the increased exchange energy in the centre causing the perpendicular magnetisation of the core.

The software allows for simulations of the magnetic structure of the disc to be made after applying a magnetic field in the z direction, shown in figure 2.9. Using a disc initially in the vortex state, the increase in the magnetic field causes the spins to gradually align until the hedgehog state is realised. When removing the applied field, the hedgehog state collapses into the single domain. The important feature in this simulation is the magnetic structure of the disc at zero field, which can be both in the single domain and the vortex state depending on the magnetic history. This control of the magnetic structure will prove useful in the results section, due to the importance of the structure in the observation of the long range proximity effect.

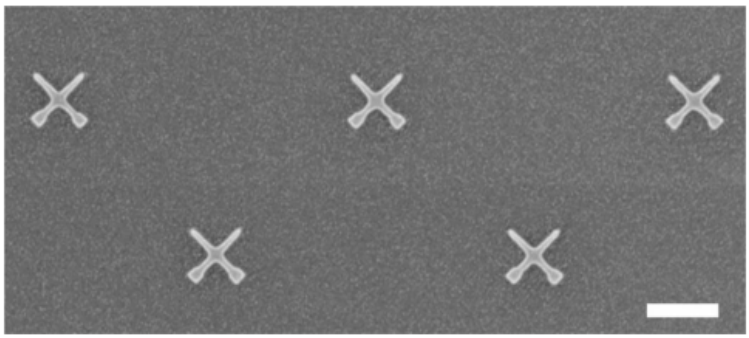

((a))

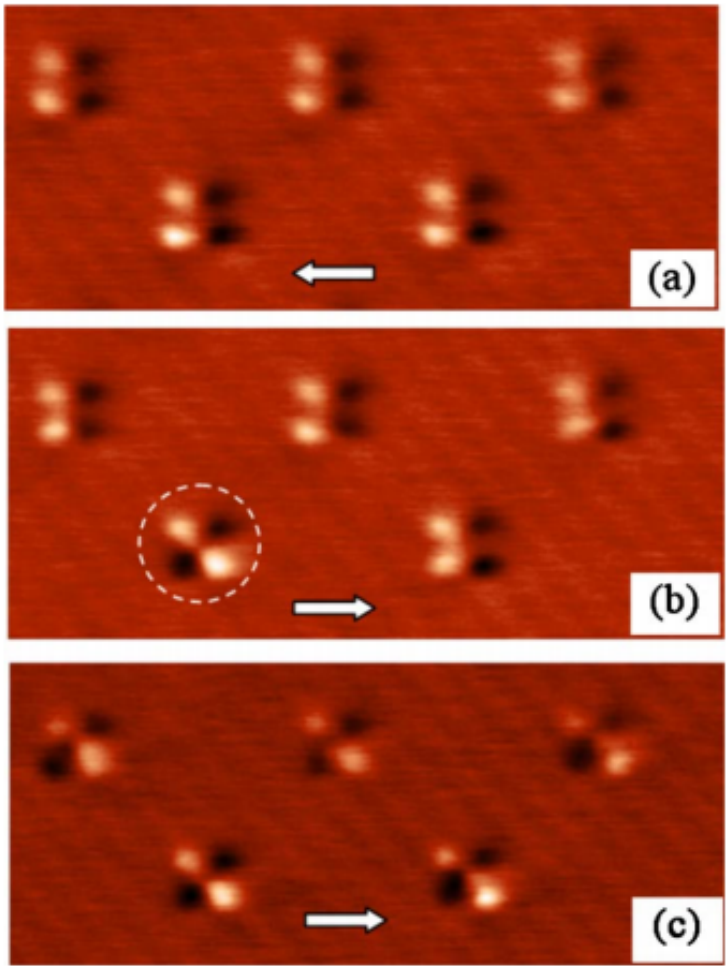

((b))

Figure 2.7: (a) SEM image taken from taken from [5] showing the asymmetric cobalt nanocrosses, the white scale bar is 1μm. (b) MFM images showing the transformations of magnetic states in the cobalt nanocrosses with the white arrows showing the applied magnetic fields. Initial image of the quasiuniform state (above). The reversed magnetic field causes a single antivortex shown in the circle (centre). Final antivortex states (below).

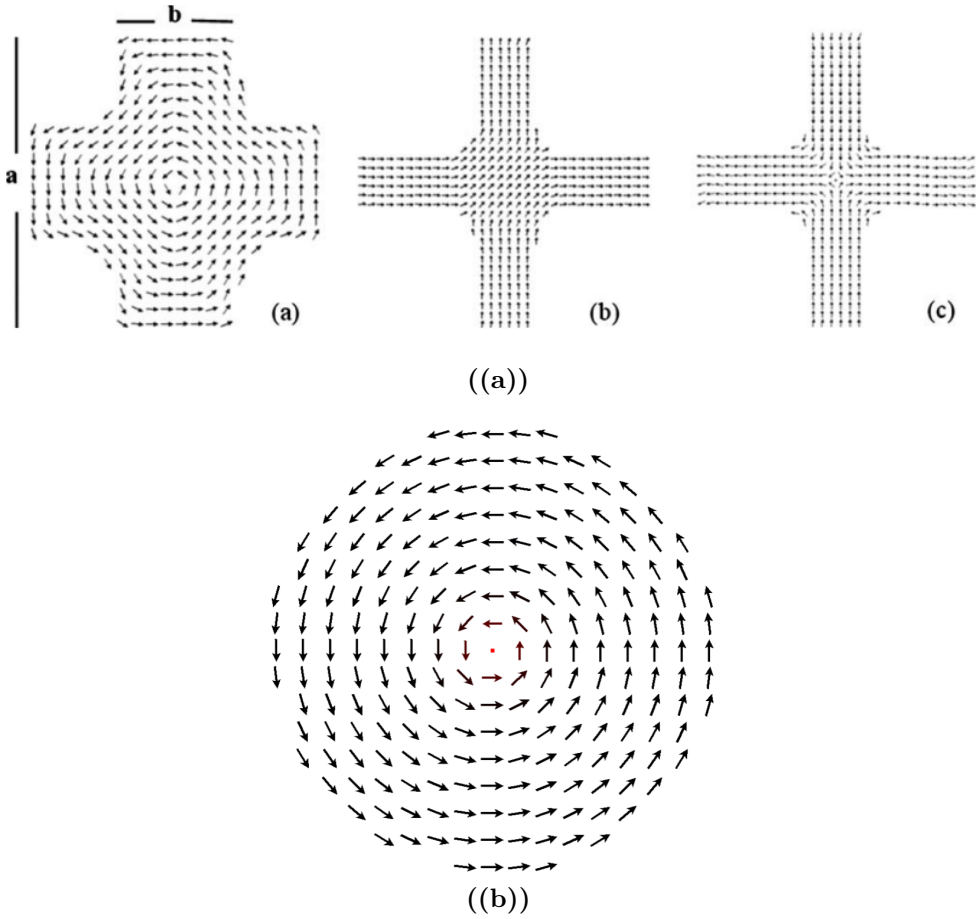

Figure 2.8: (a) Micro magnetic simulations taken from [5] showing the quasivortex state (left), quasiuniform state (centre), and antivortex state (right). (b) Micro magnetic simulation of a nickel disc 300nm in diameter and 30nm thick. It is important to notice the curling configuration, and the magnetisation at the core being forced perpendicular to the surface (red).

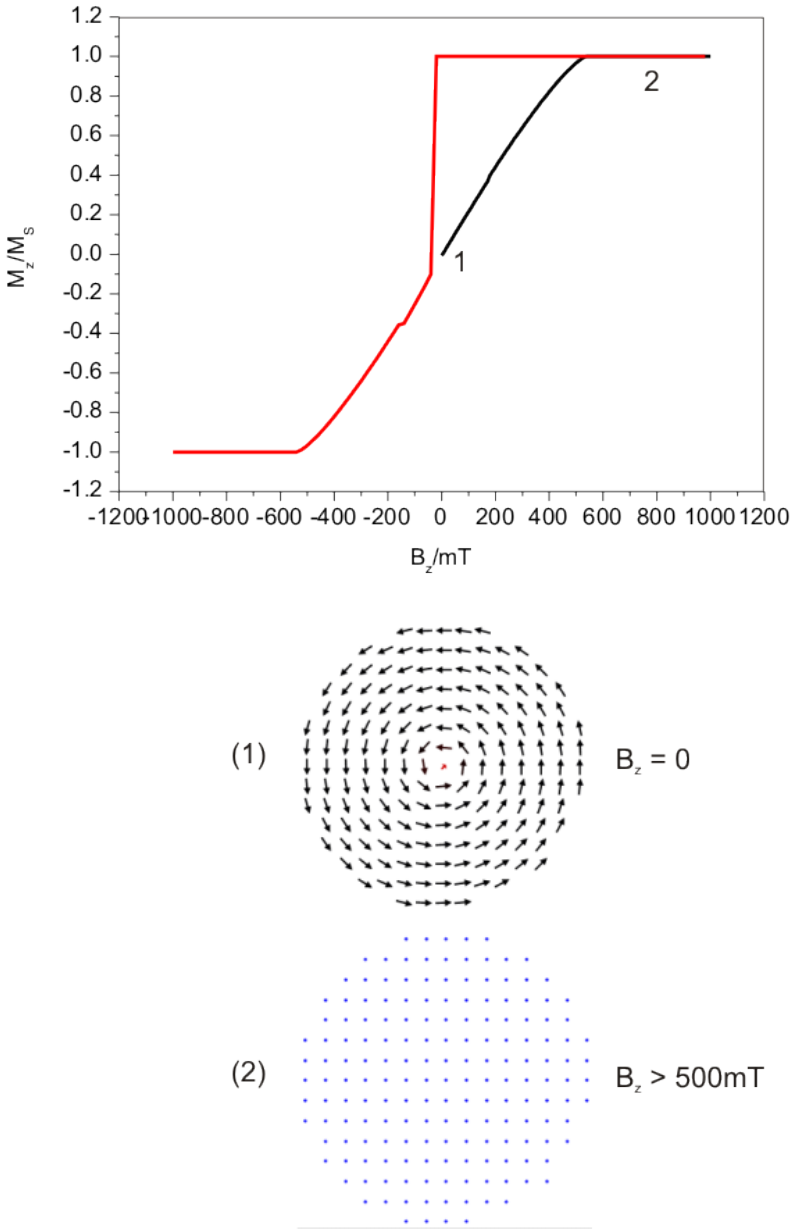

Figure 2.9: Simulated graph produced by applying a magnetic field in the z direction of a nickel disc 300nm in diameter and 30nm thick. The disc is initially in the vortex state (1) and the perpendicular magnetisation is increased, gradually turning the spins perpendicular to the plane of the disc (black line) until the hedgehog state (2) after exceeding the saturation magnetisation. Decreasing the applied field shows the single domain will form with a sudden jump to the vortex state when the field is applied in the negative z direction.

2.3 Superconductivity and the proximity effect

Since Heike Kamerlingh Onnes announced the revolutionary discovery of superconductivity in 1911 which opened up a new quantum mechanical view of physics, the volume of work on the subject has grown exponentially to become one of the most studied subjects in physics.

2.3.1 Perfect conductors and superconductors

The amount of magnetic flux enclosed within a conductor with zero resistance cannot change as $\dot{B} = 0$, meaning the flux distribution within the conductor must remain as it was when the conductor became resistanceless. There are then two situations that can occur, both of which are described using figure 2.10. Firstly, if the magnetic field is zero when the sample loses its resistance, then the flux density must remain zero after the application of the magnetic field. For this to occur, the application of a magnetic field induces resistanceless currents called screening currents which circulate on the surface to create a magnetic flux density inside the conductor that is equal and opposite to the flux density of the applied field. The flux lines outside the sample form a net distribution in superposition with the applied field, as though the sample had prevented entry of the applied flux. This sample can be described as perfectly diamagnetic.

If a magnetic field B_a is applied to the same sample before it is made resistanceless, the flux density inside is similar to that of the applied field, however becoming resistanceless will then have no effect on the magnetisation, with the same flux distribution. If the applied field is then reduced to zero, the persistent currents are induced to maintain the internal flux and leaving the sample permanently magnetised.

Superconductors were found to be more interesting than just perfect conductors, after a remarkable observation was made by Meissner and Ochsenfeld in 1933, when the flux distribution outside superconductors which had been cooled below the transition temperature within an applied magnetic field as in figure 2.11. It was found that the sample spontaneously became perfectly diamagnetic, cancelling all

internal flux instead of the expected situation shown in figure 2.10 (f). It was then concluded that superconductors possess a property that perfect conductors would not have, that a metal in the superconducting state does not allow a magnetic flux density within it, and therefore $\mathbf{B} = 0$ inside a superconductor. This effect is called the Meissner effect, and is one of the most fundamental properties of superconductors.

The phenomenon of superconductivity is characterised by the zero electrical resistance found in metals at low temperature. The microscopic theory of superconductivity was explained by Bardeen, Cooper and Schrieffer in 1957 [24] [25], which showed that when a metal is cooled below the superconducting transition temperature T_c, it becomes energetically favourable for electrons to form pairs with equal and opposite spin and momentum. These pairs, called Cooper pairs, are held together by an attractive force transmitted by the phonons in the lattice. Because this force is attractive, the energy of the Cooper pairs is lowered, and they form an energy state below that of the unpaired electrons at the Fermi energy. The Cooper pairs have a total spin of zero and so are no longer bound by the Pauli exclusion principle. They can all occupy the same energy state and can be described by a single coherent wave function. Therefore superconductors are systems containing many electron pairs that can be described by a single macroscopic wave function, meaning they display quantum interference behaviour similar to that observed with atoms at a microscopic scale, on a macroscopic scale. This leads to phenomenon of flux quantisation and the Josephson effect.

2.3.2 Flux quantisation

Considering a superconducting loop, the supercurrent circulating an enclosed path around a hole will lead to a flux density **B** inside it [6]. There will be a phase difference of the electron pair wave between any two points in the enclosed loop, due to both the presence of the magnetic field, and to the circulating current. The phase difference between two points (for example points X and Y) on the loop is given by

$$(\Delta\Phi)_{XY} = \frac{4\pi m}{hn_s e}\int_X^Y \mathbf{J}_s.d\mathbf{l} + \frac{4\pi e}{h}\int_X^Y \mathbf{A}.d\mathbf{l} \tag{2.3.1}$$

where m is the mass of an electron, n_s is the density of superelectrons, J_s is the supercurrent density, $d\mathbf{l}$ is an element of a line joining X to Y, and **A** is the magnetic vector potential. Considering the phase change occurring around a closed path, the total phase change will be

$$\Delta\Phi = \frac{4\pi m}{hn_s e}\oint \mathbf{J}_s.d\mathbf{l} + \frac{4\pi e}{h}\oint \mathbf{A}.d\mathbf{l} \tag{2.3.2}$$

Using Stokes' theorem (equation 2.3.3) where d**S** is an element of area, and using curl **A** = **B**,

$$\oint \mathbf{A}.d\mathbf{l} = \int_S\int Curl\mathbf{A}.d\mathbf{S} \tag{2.3.3}$$

The phase change around a closed path can then be written as

$$\Delta\Phi = \frac{4\pi m}{hn_s e}\oint \mathbf{J}_s.d\mathbf{l} + \frac{4\pi e}{h}\int_S\int \mathbf{B}.d\mathbf{S} \tag{2.3.4}$$

where S is the area enclosed by the closed path taken. As the superelectrons are represented by a wave, the wave at any point can only have one value of phase and amplitude. Consequently, the phase change $\Delta\Phi$ around a closed path must equal $2\pi n$ where n is an integer. This therefore leads to

$$\frac{4\pi m}{hn_s e}\oint \mathbf{J}_s.d\mathbf{l} + \frac{4\pi e}{h}\int_S\int \mathbf{B}.d\mathbf{S} = 2\pi n \tag{2.3.5}$$

which can be re-written as

$$\frac{m}{n_s e^2}\oint \mathbf{J}_s.d\mathbf{l} + \int_S \int \mathbf{B}.d\mathbf{S} = n\frac{h}{2e} \tag{2.3.6}$$

It was F. London that named the quantity on the left side of the equation the fluxoid enclosed by the closed path. It is given the symbol ϕ' to distinguish it from the flux ϕ. Due to the single valuedness of the wave function, the fluxoid can only exist in integral multiples of the unit $\frac{h}{2e}$

$$\phi' = n\frac{h}{2e} \tag{2.3.7}$$

Therefore any flux contained within the superconductor should only exist as multiples of a quantum, the fluxon, Φ_0 is given by

$$\phi_0 = \frac{h}{2e} = 2.07 \times 10^{-15} Weber \tag{2.3.8}$$

The value of n will be zero if no flux threads the hole. If the superconductor does not encircle a non superconducting region, then n will be zero.

2.3.3 Josephson tunneling

Consider for example two superconductors S_1 and S_2 separated by a large distance [6]. The phase of the electron pair wave in S_1 will be completely unrelated to the phase of the wave in S_2. By gradually decreasing the separation distance until they come into contact, we are able to see the amazing effect of quantum tunneling. When the separation distance is small, electron pairs can tunnel across the gap and the electron pair waves in S_1 and S_2 will become coupled. As the separation is decreased further, the interaction between the electrons is increased and the phases of the waves become increasingly related. When the two superconductors come into contact, they will form a single metal and there must be a definite relation between the phases throughout. The tunneling of an electron pair means that the two electrons maintain their momentum pairing after crossing the gap. If the gap is thin, the tunneling across it of electron pairs is probable resulting in a

resistanceless current flowing across it. The gap however, has a critical current I_c. When resistanceless current flows across the gap by electron pair tunneling, there is a phase difference between the electron pair waves on each side of the gap. If ϕ_{S_1} and ϕ_{S_2} are the phases on each side of the gap, and $\Delta\phi = \phi_{S_1} - \phi_{S_2}$ it can be shown that I_s is the supercurrent crossing the gap from S_1 to S_2 then

$$I_s = I_c \sin \Delta\phi \tag{2.3.9}$$

The maximum value of the supercurrent occurs when there is a phase difference of $\frac{\pi}{2}$ across the gap and I_s is then equal to the critical current of the gap, I_c. Equation 2.3.9 relates the electron pair current tunneling across a Josephson junction to the phase difference of the electron pair wave on the two sides. If the supercurrent varies with time, a voltage is developed across the Josephson tunneling junction with the phase difference $\Delta\phi$, and it can be shown that the voltage V developed across it is related to the rate of change of the phase difference by:

$$2eV = \hbar \frac{d\Delta\phi}{dt} \tag{2.3.10}$$

Equations 2.3.9 and 2.3.10 show how the current through a Josephson tunneling junction and any voltage developed across it are related to the phase difference of the electron pair on the two sides. These two equations follow from the coherent nature of the electron pair wave in a superconductor, and are the basic equations of a Josephson tunneling junction where nearly all properties can be derived.

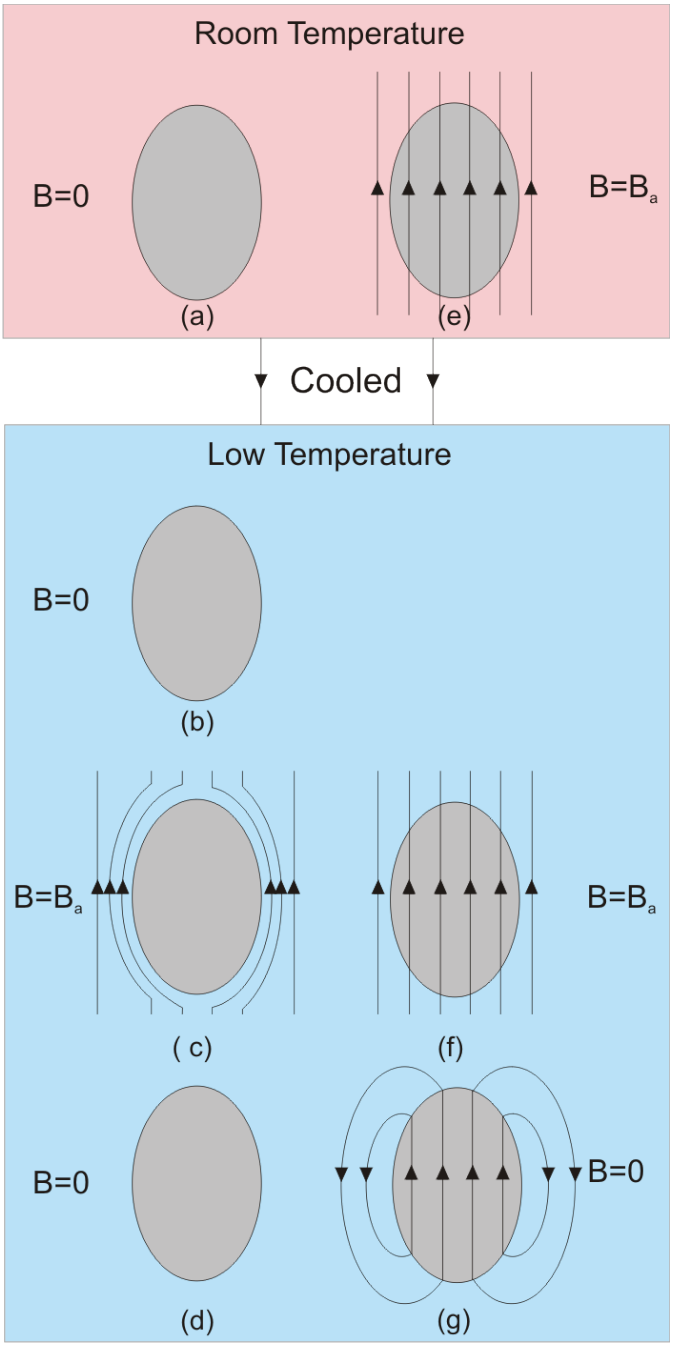

Figure 2.10: This figure is adapted from [6] and represents the magnetic behaviour of a 'perfect' conductor, as described in the text.

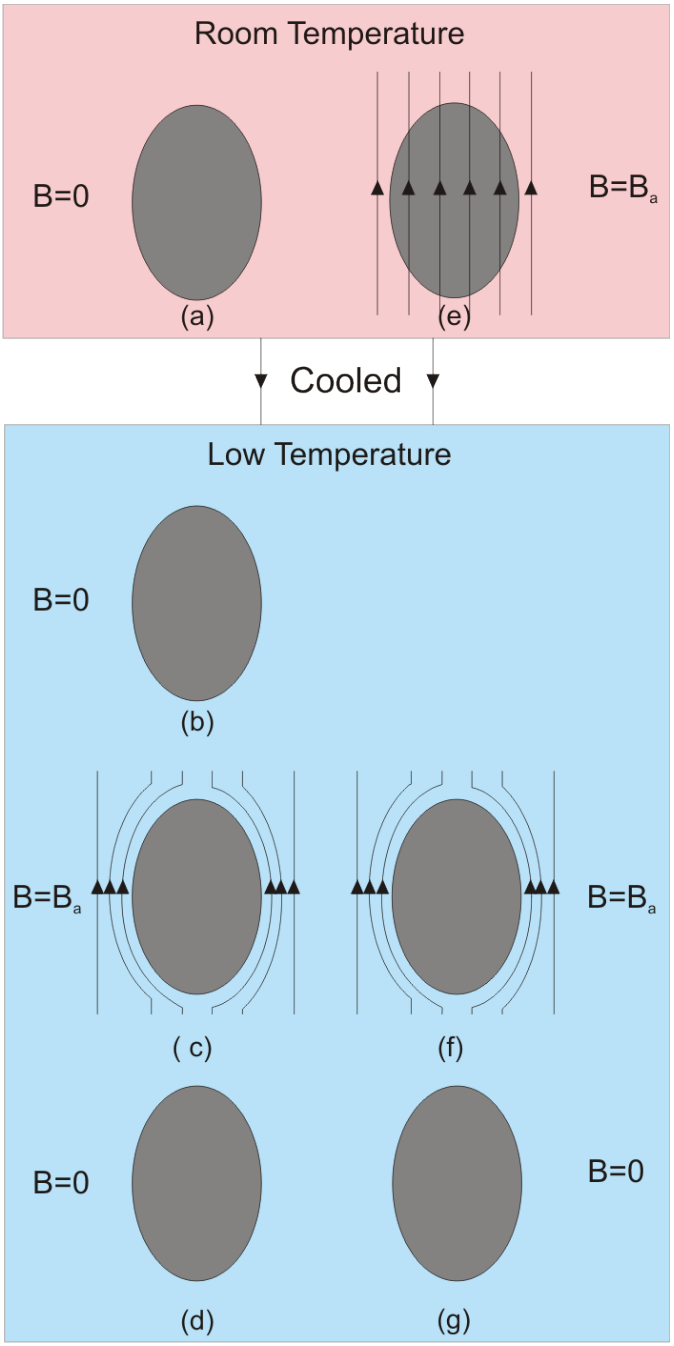

Figure 2.11: This figure is adapted from [6] and represents the magnetic behaviour of a superconductor. It is important to note the differences in (f) and (g) when compared with figure 2.10.

2.3.4 S/N/S junctions

The properties of a spin singlet superconductor and a normal (non-superconducting) metal will change near the interface when they are brought in contact [42]. The superconducting pair correlations will penetrate into the normal metal allowing it to carry a finite supercurrent, and the electrons can move from the normal metal into the superconductor and remain uncoupled for a short distance, decreasing the density of the Cooper pairs. These effects are collectively known as the proximity effect, described by Ginzburg-Landau theory in terms of the superconducting condensate wave function, the square modulus of which describes the density of Cooper pairs within the superconductor [43]. When the distance from the interface x is equal to the superconducting coherence length ξ_0, the wave function will start to decay as $e^{\frac{-x}{\xi_0}}$. Inside the normal metal, the wave function is still finite and decays as $e^{\frac{-x}{\xi_T}}$, where ξ_T is the thermal coherence length. When a normal metal has an elastic mean free path l, much shorter than the dimensions of the metal, then it is said to be in the diffusive limit and ξ_T is given by

$$\xi_T = \sqrt{\frac{\hbar D}{2\pi k_B T}} \tag{2.3.11}$$

where k_B is the Boltzmann constant, D is the diffusion coefficient of the metal, $D = \frac{v_f l}{3}$, and v_f is the Fermi velocity. When the mean free path is greater than the dimensions of the metal then it is said to be in the ballistic limit and the normal coherence length is given by

$$\xi_T = \frac{\hbar v_f}{2\pi k_B T} \tag{2.3.12}$$

Consider two superconductors separated by a normal metal as shown in figure 2.12 (b). There will be an overlap between the wave functions of the two superconductors if the length of the normal metal is shorter than $2\xi_T$, meaning a Cooper pair can remain coherent along the length of the normal metal, allowing a supercurrent to flow. The maximum critical current in the normal metal, I_c will obviously be lower than the two superconductors due to the reduction of the wavefunction in the centre.

2.3.5 Andreev reflection

In 1964, A. Andreev presented a solution to the problem arising from the proximity effect; explaining how an electron can move from the normal metal into the superconductor if there are no energy states in the superconductor when the superconducting energy gap Δ is much larger than k_BT at low temperatures [44]. The process involves an electron in the normal metal incident on the interface, which forms a Cooper pair in the superconductor with a retroreflected hole of opposite spin and momentum as shown in figure 2.13. Each electron reflection transfers a charge $2e$ across the interface, avoiding the forbidden single particle transmission within the energy gap. As the Cooper pair consists of an up and down spin electron, a second electron of opposite spin will form the pair of the superconductor with another reflected hole. As the process is highly spin dependent, if only one spin band is occupied by the conduction electrons in the normal metal, it will not be able to form a pair in the superconductor and the Andreev reflection process will not be possible. Therefore in a normal metal with an applied magnetic field, or with a ferromagnetic material, the strength of the Andreev reflection is a function of the spin polarisation of the normal/ferromagnetic material.

An important feature of Andreev reflection is that the reflected particle inherits phase information. If the phase of the superconductor is ϕ_s, then an electron will gain a change of $+\phi_s$, with the hole changing by $-\phi_s$. The reflected particle can be thought of as a time reversed version of the incoming particle, and they will remain correlated up to a maximum distance of L_ϕ, the phase breaking length. This means that for an SNS system, the Thouless energy, E_{Th} can be defined as:

$$E_{Th} = \frac{\hbar D}{L^2} \tag{2.3.13}$$

where D is the diffusion coefficient, L is the length of the normal section, and E_{Th} is the energy under which electron-hole pairs will remain correlated across the whole system. Variations of the normal metal resistance occur when the energy density is changed due to the constructive and destructive interference effects of the interaction between incoming and reflected particles, with the maximum cor-

relation occurring from the constructive interference when the two are in phase. This correlation leads to an energy gap in the metal similar to that observed in a superconductor, the magnitude being equal to E_{Th} and is phase dependent, reaching a maximum when the phase difference ϕ between the two superconductors is $\phi = n2\pi$ (where n is an integer) leading to a reduction of the resistance, and a minimum when $\phi = n\pi$, destroying the correlations and unaffecting the resistance. This effect can be exploited in the formation of an Andreev interferometer, which consists of an SNS junction with a normal length greater than ξ_T but shorter than L_ϕ. This condition means there will be no significant supercurrent through the junction, but an electron with energy less than E_{Th} reflected from one N/S interface will retain its phase information until it reaches the other interface. Interference between the electrons will occur based on the phase difference between the two superconducting electrodes, $\phi = \phi_2 - \phi_1$, and the resistance of the normal metal can then be defined as

$$R = R_0 - \gamma(1 + \cos\phi) \tag{2.3.14}$$

Where R_0 is the normal resistance of the metal and γ is an amplitude factor controlled by the properties of the system such as the diffusivity of the normal metal, the number of impurities and the quality of the SN interface.

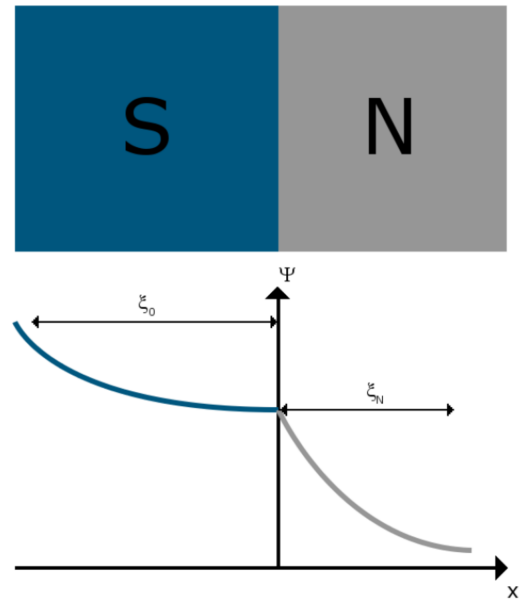

((a))

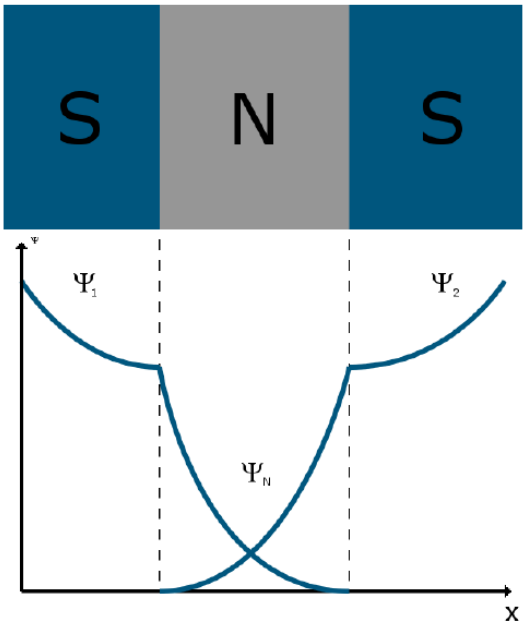

((b))

Figure 2.12: Figure taken from [7] showing (a) the penetration of Cooper pairs from the superconductor to the normal metal remaining coherent up to a certain distance from the interface, and also the movement of quasi-particles from the normal metal into the superconductor. (b) Shows an SNS junction, with the two superconductors' wavefunctions overlapping in the normal metal enabling Cooper pairs to remain coherent across the junction and allowing a supercurrent to flow.

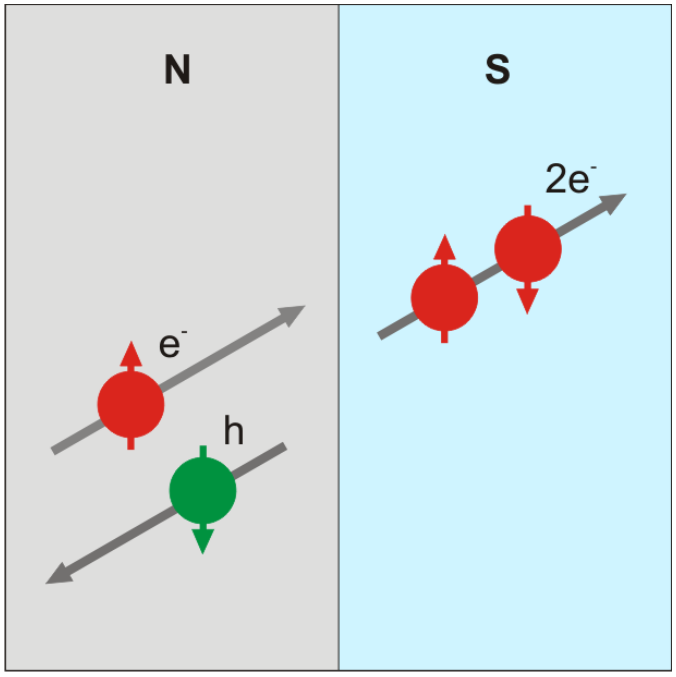

Figure 2.13: An electron above the Fermi energy in the normal metal cannot move into the superconductor as there are no allowed energy levels. This figure shows the process of Andreev reflection; the incoming electron is retroreflected at the SN interface, with charge and momentum reversed and travelling back along the incoming electrons path. The two quasi-particles move into the superconductor to become a Cooper pair.

2.3.6 The Andreev interferometer

The first experimental evidence of interference effects in a SNS structure was provided by Petrashov *et al* in 1993, by measuring the magnetoresistance of mesoscopic metal rings [8]. The measurement consisted of three different configurations as shown in figure 2.14, and the nanostructure with superconducting islands placed on the current leads showed Aharonov-Bohm oscillations that were 100 times greater than those without the superconductor. With a different configuration, the superconducting islands were placed perpendicular to the current flow, and revealed oscillations with period of $\frac{h}{2e}$. This experiment clearly shows the superconductor has a substantial effect on the magnetoresistance, however the results were limited by the inability to control the phase difference between the two superconductors.

This situation was improved in 1994 [9] by connecting a mesoscopic ring of normal metal to a loop of superconducting material, as shown in figure 2.15. The most important feature of this experiment, was the ability to control the flux through the superconducting loop, enabling them to show that the resistance of the ring oscillating as a function of the phase difference across it.

Results expanding on this work were published in 1995 [10], with a cross of silver or antimony connected to a superconducting loop of aluminium, represented in figure 2.16 (a). The horizontal section of the cross and the connected aluminium formed an SNS junction, while measurements were taken of the vertical section of the cross. Importantly, the phase across the junction could be controlled by generating flux through the loop with an applied magnetic field, or by passing a current through the loop using the two superconducting leads. The phase difference due to the magnetic flux $\Phi_{external}$ and the applied current $I_{control}$ can be expressed as

$$\phi = \frac{2\pi(\Phi_{external} + I_{control}L)}{\Phi_0} \tag{2.3.15}$$

Where L is the inductance of the loop. The results of the experiment can be seen in figure 2.16 (b), with oscillations in $\Delta\phi$ of period 2π.

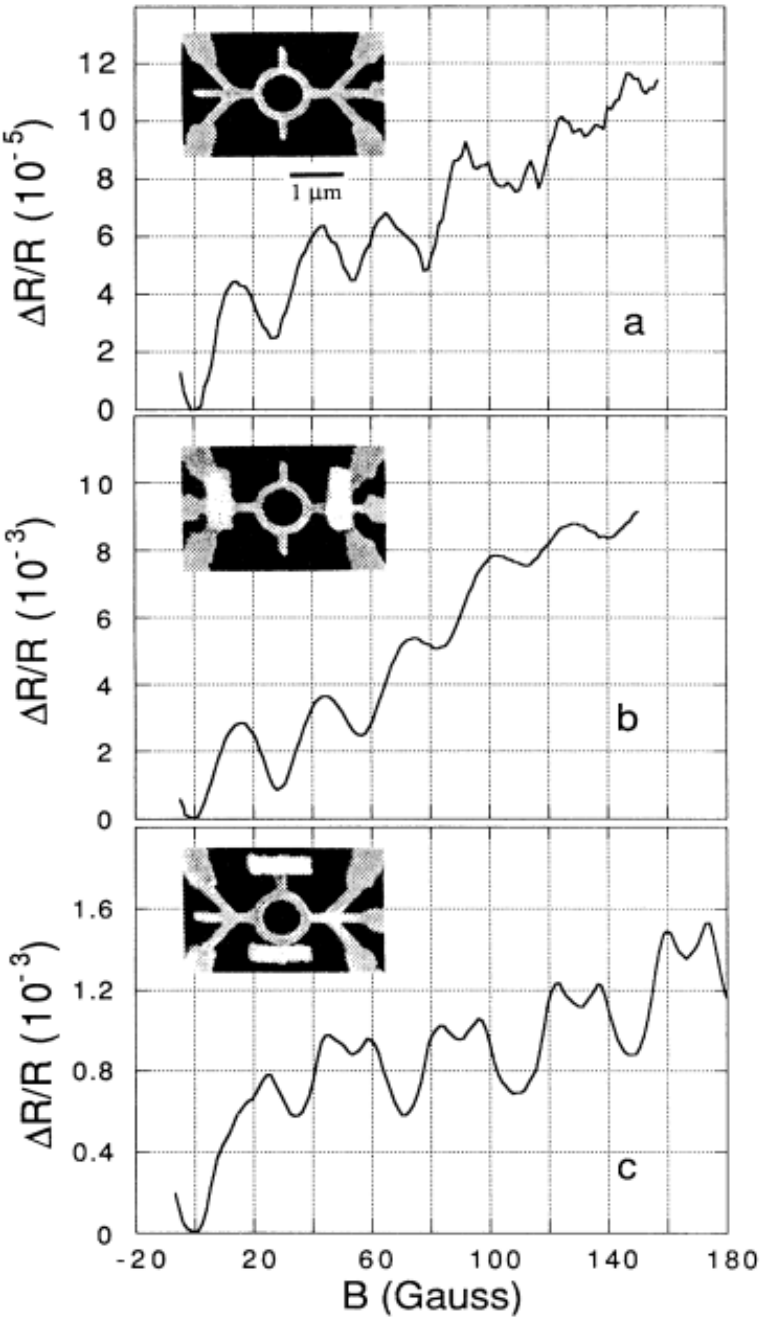

Figure 2.14: Results showing the magnetoresistance of mesoscopic silver rings taken from Petrashov *et al* [8] with the insets showing SEM images of the samples measured. The top image show rings without the superconducting mirrors with the expected $\frac{h}{2e}$ Aharonov-Bohm oscillations. The second figure shows the rings with superconducting mirrors on the current leads showing 100 times enhanced $\frac{h}{2e}$ oscillations. The lower image shows rings with superconducting mirrors perpendicular to the current direction showed $\frac{h}{4e}$ oscillations. It is important to note the large differences in the scales in each graph.

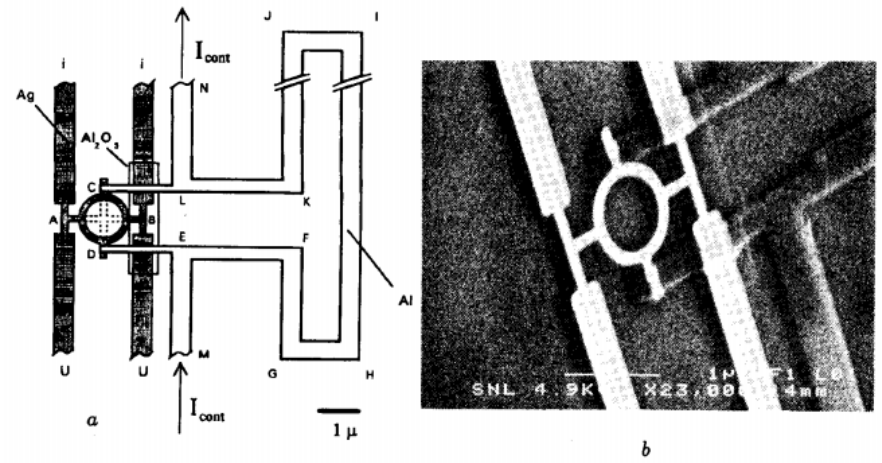

((a))

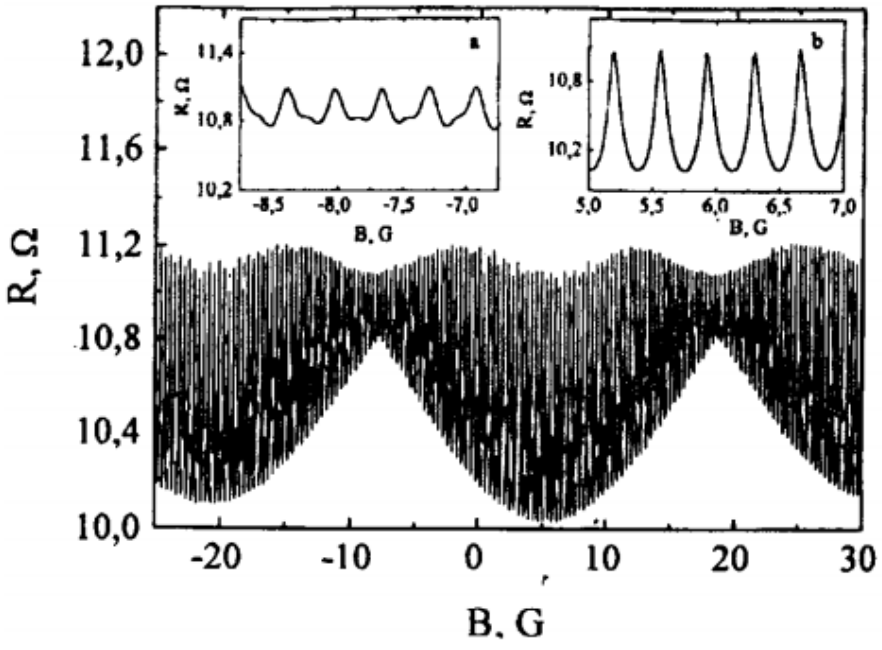

((b))

Figure 2.15: Figure (a) shows a schematic and SEM image of the sample measured in [9], where a mesoscopic silver ring was connected to a superconducting aluminium loop. The current and potential leads were used to measure the resistance between points A and B of the silver structure (R_{AB}). Figure (b) shows the resistance R_{AB} of the ring oscillated as a function of the phase drop across it, by controlling the flux through the superconducting loop.

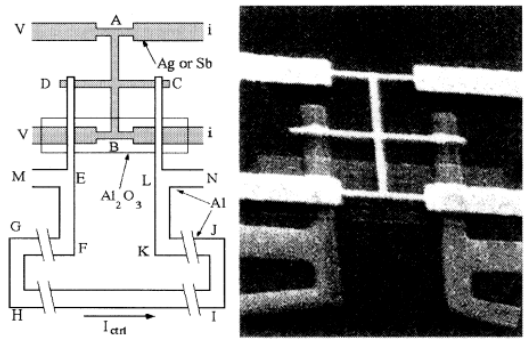

((a))

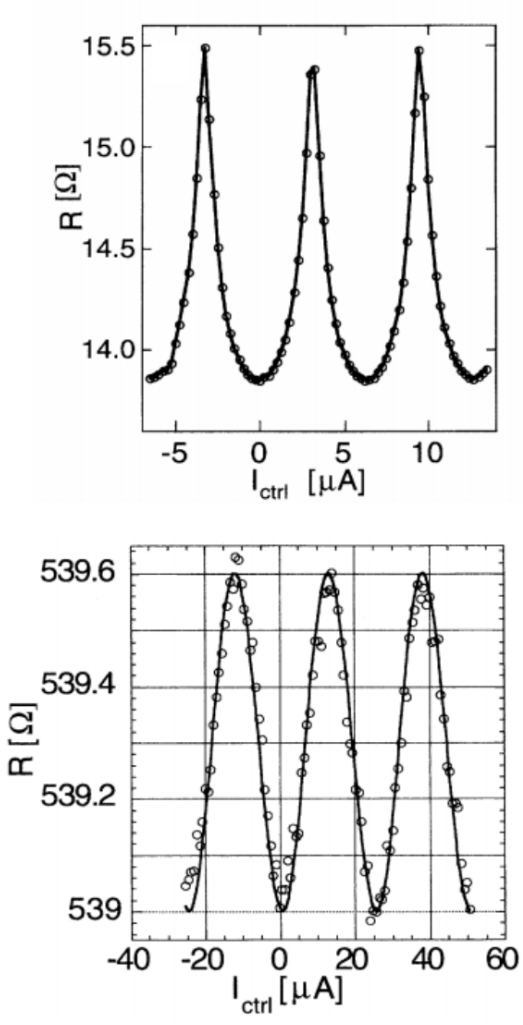

((b))

Figure 2.16: Figure (a) shows a mesoscopic cross of silver or antimony attached to a aluminium loop that was measured in [10]. The phase difference between C and D can be controlled by applying a magnetic flux through the loop or by passing a current through the loop using the attached leads. The resistance of the cross between A and B was probed using a four point measurement and was shown to oscillate with phase as shown in (b). It is important to note the shape of the oscillations between the silver cross (above) and the antimony cross (below), which was later explained by Nazarov and Stoof [11].

2.3.7 S/F/S junctions

When a conventional spin-singlet superconductor is placed in contact with a normal metal, superconducting pair correlations penetrate into the normal metal giving rise to the superconducting proximity effect, where the normal metal may become superconducting within the coherence length $\xi_T = \sqrt{\frac{\hbar D}{2\pi k_B T}}$ from the interface. The changes in the normal conductance however can survive up to the longer electron phase breaking length, $L_\phi = \sqrt{D\tau_\phi}$, ($\tau_\phi^{-1}$ is the electron phase breaking rate). If the normal metal is replaced with a ferromagnet, the quantum mechanical exchange interaction tries to align the electron spins, compared to the antiparallel spins of a Cooper pair. It is this antagonistic property that gives rise to the paramagnetic effect of pair breaking, leading to a rapid loss of phase coherence between electrons with opposing spins, only penetrating over a much shorter distance, specifically

$$\xi_F = \sqrt{\frac{\hbar D}{2\pi k_B T_{Curie}}} \tag{2.3.16}$$

As typically $T << T_{Curie}$, ξ_F is much shorter than ξ_T, meaning the proximity effect in ferromagnets is negligible and an SF system can be considered as an incoherent metal coupled to the superconductor. The exchange interaction in the ferromagnet causes the electronic bands for spin-up and spin-down to be shifted by $2E_{ex}$ as shown in figure 2.17, which is taken from an excellent review of the subject given recently by M. Eschrig outlining the major considerations for the spin polarised supercurrents. This exchange splitting will shift the momenta at the Fermi energy from $\mathbf{k}_F$ to $\mathbf{k}_{F\uparrow} = \mathbf{k}_F + \frac{\mathbf{Q}}{2}$ and $\mathbf{k}_{F\downarrow} = \mathbf{k}_F - \frac{\mathbf{Q}}{2}$. These two electrons will then form a Cooper pair with opposing spins and centre of mass momentum $\pm\mathbf{Q}$. As spin-singlet superconductivity couples quasiparticles of different spins by Andreev reflection, the long range coherence in normal metals require spin-degenerate bands close to the Fermi energy. Therefore the spin splitting caused by the exchange field energy leads to a strong decoherence of quasiparticles belonging to the different spin bands. As the superconducting energy scale is orders of magnitude smaller than the exchange field energy, the proximity effect in ferromagnetic metals is

significantly reduced.

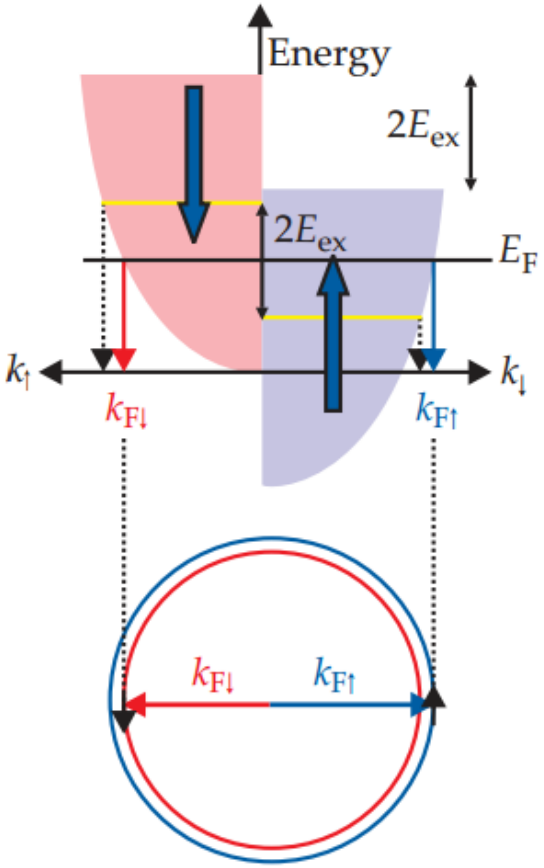

Figure 2.17: Image taken from [12] showing the electron spin bands for spin-up (blue) and spin-down (red) which are shifted by $2E_{ex}$ relative to each other.

Spin mixing

One of the most important mechanisms to mention when discussing SF structures is the idea of spin mixing. Superconducting Cooper pairs will prefer the singlet state ($\uparrow\downarrow - \downarrow\uparrow$), however the exchange splitting mentioned above will cause a modulation of the pair amplitude with position $\mathbf{R}$, and therefore the two spin contributions to the pair amplitude will be proportional to $e^{\pm i(\mathbf{k}_{F\uparrow}-\mathbf{k}_{F\downarrow})R}$. The resulting state is a mixture of singlet and triplet states with opposing spins, called the FFLO phase [45] [46]:

$$(\uparrow\downarrow - \downarrow\uparrow) \rightarrow (\uparrow\downarrow e^{i\mathbf{QR}} - \downarrow\uparrow e^{-i\mathbf{QR}}) = (\uparrow\downarrow - \downarrow\uparrow)\cos(\mathbf{QR}) + i(\uparrow\downarrow + \downarrow\uparrow)\sin(\mathbf{QR}) \tag{2.3.17}$$

The relation of this to the proximity effect can be clearly shown in figure 2.18. This figure shows the penetration of the pair amplitudes of the wavefunction as a function of distance from the interface. It is important to note the FFLO amplitudes induced at the SF interface that oscillate with wavenumber $\frac{Q}{\hbar}$ and that are heavily dependent on the size of the exchange field E_{ex}. The spin polarised barrier that causes the exchange splitting also modifies the Cooper pairs' internal structure due to the phase shifts acquired when quantum mechanically penetrating through the interface. These phase shifts are spin dependent, with the net phase difference θ acquired during reflection leading to the singlet-triplet mixing of Cooper pairs:

$$(\uparrow\downarrow - \downarrow\uparrow) \rightarrow (\uparrow\downarrow e^{i\theta} - \downarrow\uparrow e^{-i\theta}) = (\uparrow\downarrow - \downarrow\uparrow)\cos(\theta) + i(\uparrow\downarrow + \downarrow\uparrow)\sin(\theta) \tag{2.3.18}$$

In SNS junctions, the oscillatory dependence of the current on the magnetic field arises due to the interference of the phases of the electrons of the Cooper pair which are determined by the vector potential. In 1982, Buzdin *et al.* calculated the Josephson current in an SFS junction for a short weak link (where the thickness of the ferromagnet is small compared with the superconducting correlation length and the electron mean free path) consisting of a single domained ferromag-

net, and found that the interference also occurs in SFS junctions with the phases of the electrons in the Cooper pair determined by the exchange field of the ferromagnet [47]. They therefore explained that the amplitudes decay much faster with the greater spin splitting, and found the maximum current through the junction can be detected experimentally to oscillate with temperature as the exchange field in the ferromagnet changes with temperature, and will oscillate as a function of ferromagnet length with an exponential decay of the oscillations due to the impurity scattering. The physics behind the oscillatory behaviour in SF systems with a uniform magnetisation have been considered in [48], and have been since seen experimentally in [49] and [50]. Interestingly the measured oscillatory dependence of I_c on thickness fits to the theoretical predictions calculated by Buzdin, allowing calculations for the value of ξ_F and therefore the exchange energy.

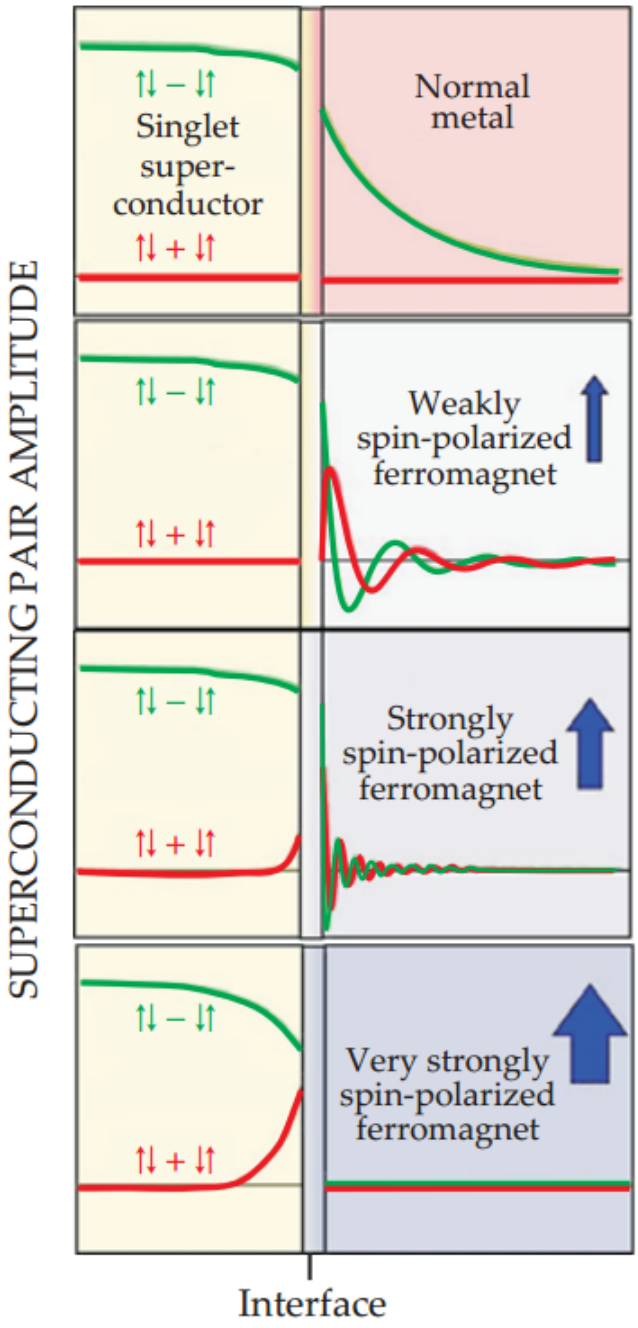

Figure 2.18: Image taken from [12] showing the proximity effect for SN and SF structures with varying strength ferromagnets. The singlet state (green) and the triplet state (red) penetrates over large distances in the normal metal, however is significantly reduced with increased exchange splitting. With a large exchange field, the Cooper pair will decay over atomically small distances.

2.4 The long range proximity effect

2.4.1 Variations in conductance

The effect on simple barrier junctions using ferromagnets such as cobalt is well understood. The singlet based I_c oscillates as a function of the cobalt thickness with a period of approximately 1nm superimposed on an exponentially decaying function with a characteristic length of $\xi_{Co} \approx 1nm$ [18]. There were some experiments on SFS systems however, that showed considerable changes in the conductance in S/F structures below T_c that required particular attention.

A pioneering paper came in 1994, with the experimental study of the conductance of superconducting islands deposited onto the surface of nickel structures [51]. They reported that the resistance of the nickel changed significantly with the onset of superconductivity, and the distance extended to more than 30 times larger than the coherence length of the electrons in a ferromagnet. At the time, explanations were not fully available however the behaviour of the conductivity of the nickel structures were related to the proximity effect in SNS structures as they were qualitatively similar to recent results involving silver samples.

In 1998 the group from Grenoble headed by B. Pannetier studied the superconducting proximity effect in a ferromagnetic metal [13]. They investigated the transport properties on a sample made from a cobalt wire on contact with aluminium as shown in figure 2.19 (a), and showed that the decay length for the proximity effect is much larger than expected from the exchange field of the ferromagnet. The particularly interesting part of the paper is the measurement of the differential resistance which is shown in figure 2.19 (b), revealing the interesting feature of a zero bias peak, a minimum at the 1.7 μA range, and returning to the normal state at high bias. The conclusions drawn from the paper state that this is strongly reminiscent of the reentrance effect, and will provide a useful reference in the results section of this thesis.

In 1999, the group headed by V. T. Petrashov presented observations of a strong mutual influence of hybrid FS nanostructures, revealing the proximity induced conductance on the F side to be two orders of magnitude larger than expected [52].

They found a crossover from positive to negative proximity induced conductance with increasing interface resistance, and note reentrance of the superconductor to the normal state has been found in low applied fields, with the new peaks seen in the differential resistance as an effect of the saturation magnetisation.

Another noteworthy paper was presented in 2001, explains measurements for electron transport in SF systems for a range of interface resistances. They found that the ferromagnet alone shows no appreciable superconducting proximity effect, but the SF interface exhibited strong temperature, field and bias current dependences [53]. It was suggested in [54] that the increased conductance was due to scattering at the S/F interface, and [53] suggested the change in conductance was related to the interface resistance. However, the interface resistance in [52] was measured to be small, and it was shown that the entire change in the conductance was due to an increase in the conductivity of the ferromagnet. The proximity effect is not considerably affected by the exchange energy if $h < T_c$, but these experiments use the strong ferromagnets of cobalt and iron with an exchange energy several orders of magnitude larger than T_c, so the singlet pairing is impossible. It was the above experimental results that inspired a new line of theoretical predictions into the long range proximity effect.

2.4.2 Spin flip scattering

One of the key developments to mention with reference to the SFS section above, is that pairs made from parallel spins at the Fermi energy can pair with equal and opposite momentum $\mathbf{k}_{F\uparrow}$ and $-\mathbf{k}_{F\uparrow}$ with zero centre of mass momentum. Therefore no oscillations will occur and the condensate can penetrate over a long range; comparable to lengths seen in a normal metal.

The next important concept to describe is the mechanism used to generate the equal spin pairs, which is elegantly explained in [12] with reference to figure 2.20. The process involves considering the amplitudes created by the spin mixing mechanism described above from a different angle in spin space.

The singlet states are independent of the quantisation direction so are rotationally invariant, but the triplet spin states transform into each other when the quantisa-

tion direction changes.

Figure 2.20 shows that when the interface in an SF system is magnetised in the same direction as the ferromagnet, the ferromagnet induces opposite spin-triplet mixing in the superconductor that penetrate only a short distance. If the interface is magnetised in a different direction however, the three triplet spin states mix in the different quantisation bases. If the interface is magnetised in the y-direction as shown in figure 2.20, opposite spin pairs with respect to the y-axis will be generated. It is this state that is equivalent to a combination of equal spin pairs when observed with respect to the z-axis, and it is this equal spin state that penetrates long distances into the ferromagnet.

2.4.3 Theoretical predictions of the long range proximity effect

It was the above information that lead to the first prediction of spin-triplet superconducting correlations induced due to a local inhomogeneity of the magnetisation at the SF interface shown in figure 2.21 (a) [14]. The inhomogeneity generates a triplet component of the superconducting order parameter with an amplitude comparable with that of the singlet pairing, and that the exchange field cannot destroy as the spins of the electrons forming Cooper pairs are already parallel. It was shown that not only the singlet component of the superconducting condensate is induced, undergoing the well known oscillations [47] and penetrating into the ferromagnet over a short length $\xi_F = \sqrt{\frac{D}{h}}$ (where h is the exchange field and D is the diffusion coefficient) but also the triplet component, which can penetrate into the ferromagnet over a longer length $\xi_\epsilon = \sqrt{\frac{D}{\epsilon}}$ (where the energy ϵ is of the order of temperature T or the Thouless energy $E_T = \frac{D}{L^2}$ where L is the sample size) which leads to a significant increase of the ferromagnetic conductance below the critical temperature of the superconductor. This lead to the revolutionary conclusion that the length ξ_ϵ is of the same order as that for the penetration of the superconducting pairs into a normal metal and therefore the increase in the conductance due to the proximity effect can be comparable with that in a S/N

structure. It is important to note all four symmetry components are induced in the superconducting regions next to the interface but only the (↑↑) triplet penetrate into the ferromagnet.

The above theory explained the generation of a triplet condensate by an inhomogeneous magnetisation and its penetration into the ferromagnet, with the main focus in the changes to the conductivity of the ferromagnet. In 2003, the same authors expanded on the above theory to introduce the idea of a new odd-triplet superconductivity and discuss how to detect this experimentally [55]. This suggestion included the introduction of an SF multilayer, with the main emphasis being on the control of the neighbouring magnetisations, achieving the non collinear alignment by using an exchange biased spin-valve or using ferromagnets with strong anisotropy and different axis of easy magnetisation.

If the directions of the magnetisations of the different F layers are neither parallel or anti parallel, they suggest the pair amplitude has to be isotropic in space, and remain unchanged with the interchange of the two electrons. As the triplet pair is even with the interchanging electron spins, the pair wavefunction must be odd with respect to interchanging the time coordinates of the two electrons.

This new type of condensate that is odd in frequency and even in momentum will be long ranged within the ferromagnet, and not sensitive to impurities. This is particularly interesting as no known material has this symmetry, and a similar multi-layered design provided some remarkable results [19] and is explained in detail in the later subsection.

Kadigrobov *et al.* were also interested by the experiments that revealed a large excess of conductance at the F/S boundary, and noticed that the spin-triplet fluctuations in the electron-hole correlations caused by the spin-orbit interaction and electron impurity scattering cannot explain the large effect observed in [56], and in 2001 published some equally revolutionary work on the subject [16]. This paper showed that quantum spin fluctuations in inhomogeneous ferromagnets drastically affect the Andreev reflection of electrons and holes at the F/S interface, resulting in a strong long-range proximity effect.

They briefly analyse the process similar to that considered above, when a Cooper

pair propagates from the superconductor to the ferromagnet being in the singlet state at the moment of the injection, which is then scattered into the triplet configuration by the inhomogeneously oriented magnetisation, however more interestingly they consider a different model for the magnetic inhomogeneity that acts as magnetic spin splitter for the incident electron as shown in figure 2.22. The incident spin-up electron crosses the inhomogeneous ferromagnetic layer and splits up into a coherent mixture of spin-up and spin-down electronic states which are subject to Andreev reflection at the F/S interface, transforming to spin-down and spin-up holes states. These two states encounter the magnetic scattering layer again and experience further spin splitting. The final result of the composite scattering process is that the incoming electron is reflected in two hole-channels, one with spin-up and the other with spin-down, meaning one of the reflected hole channels has the same spin orientation as the incident electron.

It was difficult to plan this for an experiment without knowing the detailed character of the magnetic inhomogeneity, however they considered the effect of two samples; a multi domain structure with non parallel magnetisation in neighbouring domains, and two domains with parallel magnetisation with spin splitting in the domain wall. They show the superconducting correlations due to the spin splitting process in the magnetic region will decay exponentially in the ferromagnet and vanish at distances corresponding to the superconducting correlation length in normal metals. They showed the calculations of the excess resistance is in agreement with the experiment, by using experimental values of the parameters taken from [52].

An excellent review was provided in 2005 by Bergeret *et al.*, specifically looking at the unusual effects caused by the triplet component of the condensate function in superconductor-ferromagnet structures [57]. They recap the previous work on the subject, emphasising the generation of the triplet component that is odd in frequency and even in momentum which is not destroyed by even a strong exchange field, and unlike anomalous order parameters in ^3He and unconventional superconductors, is insensitive to non magnetic impurities. They also consider other effects caused by the proximity effect, including an enhancement of the Josephson

current due to the presence of the ferromagnet, induction of a magnetic moment in superconductors resulting in a screening of the magnetic moment, and formation of periodic magnetic structures due to the influence of the superconductor.

An important contribution came from M. Houzet and A. Buzdin in 2007 [15], that presented work on the Josephson current through a ferromagnetic tri-layer as shown in figure 2.21 (b). They look at the conditions required to achieve the Josephson effect, and specifically indicate that both interfaces need to be magnetically non collinear and share specific symmetries. They note that this is a vital requirement, as with collinear (parallel or antiparallel) magnetisation of the F layers, the Josephson current is small due to the short range proximity effect. Even though this experiment was designed for a multi layered structure, it is crucial to take the discussed physics into account as this could provide a substantial contribution to the experiment of this thesis.

Some interesting results were presented by M. Eschrig and T. Lofwander [58] after some surprising experimental results on half metallic ferromagnets in 2006 [2], which have the remarkable feature of showing conducting or insulating behaviour depending on the direction of the electron spin. They describe a similar process as described above, and explain the mechanism for the conversion between unpolarised and completely spin polarised supercurrents based on electron spin precession together with triplet-pair rotation at interfaces with broken spin-rotation symmetry. They calculate the Josephson current through the junction, and show the magnitude of this can be on the order of normal metal junctions, and is reduced for longer junctions. Their model contains contributions to the phases that depend on the microscopic structure of the disordered magnetic moments at the two interfaces, and conclude that there is a strong sensitivity of the critical Josephson current on the properties of the interface, which will lead to a large sample to sample variation. This opens up to some possible variations in experiment, especially if the properties of the interface can be changed for example by applying a magnetic field. This paper specifically looks into the effect using two singlet superconductors and a half metallic ferromagnet, however this information provides an insight into the mechanism for the generation of equal spin pairs which is an

essential part of this project.

It is the above theoretical calculations, together with the experimental breakthroughs mentioned below that will lead to structures combining the zero resistance of supercurrents with the spin alignment of ferromagnets to enable fully spin polarised supercurrents, and superconducting spintronics devices. These will introduce the elements of nonlocality, entanglement, and quantum coherence, all of which will be crucial for quantum computing [12].

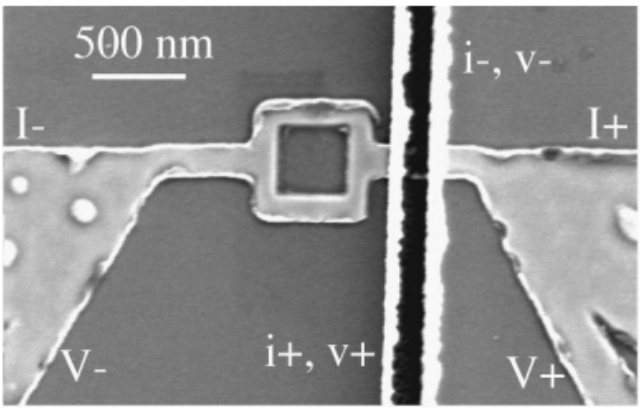

((a))

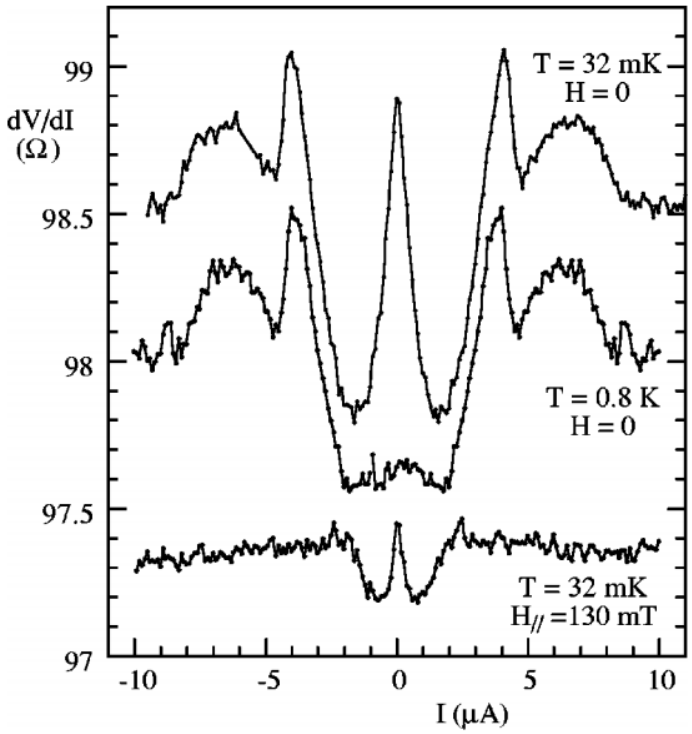

((b))

Figure 2.19: (a) shows the SEM micrograph of the sample measured in [13], showing a cobalt wire and loop in contact with an aluminium island. (b) shows the differential resistance of the sample measured the different conditions labeled. The increase in magnetic field parallel to the sample strongly depresses the aluminium gap, but does now affect the characteristic energies of the electrons in the FS sample. This means the aluminium peaks are depressed, but the zero bias peak which was related to reentrance was still present.

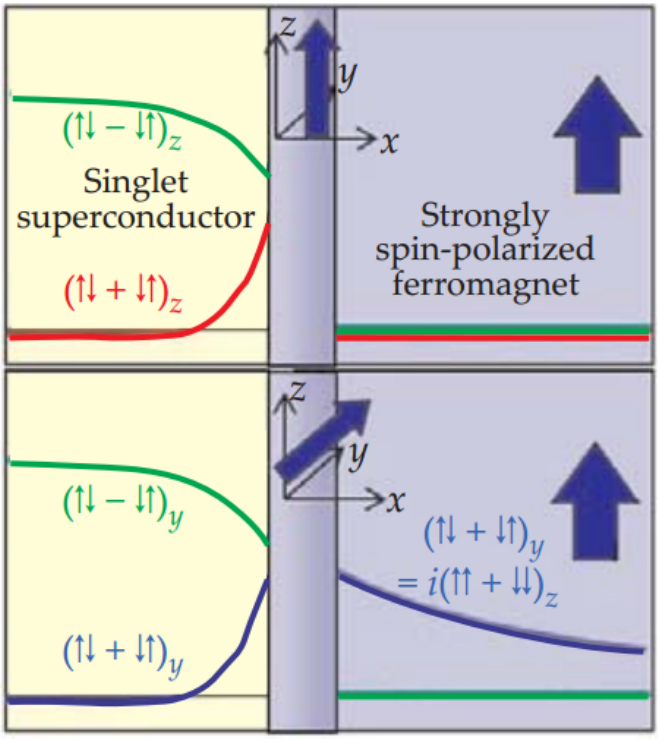

Figure 2.20: Figure taken from [12] highlighting the generation of equal spin pairs, where the $(\uparrow\downarrow + \downarrow\uparrow)$ triplet state in the y-basis is the equal spin $i(\uparrow\uparrow + \downarrow\downarrow)$ triplet state in the z-basis.

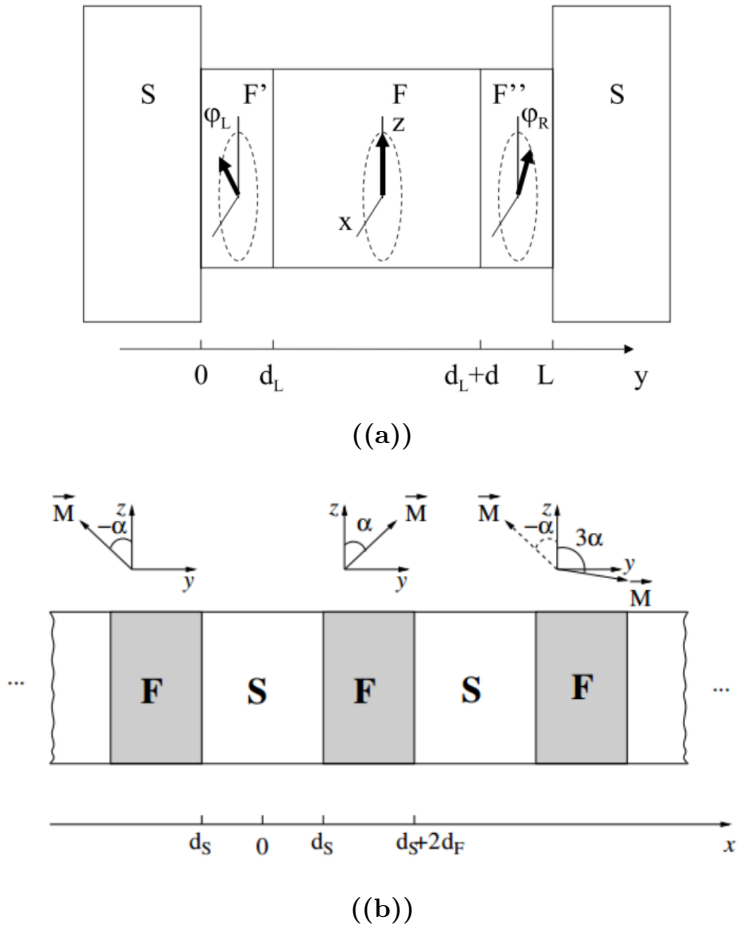

Figure 2.21: (a) shows a schematic diagram of a SF multilayer considered in [14], with the magnetisation of the different F layers shown above. (b) shows the geometry of the S/F'/F/F"/S system taken from [15], with indications of the noncollinear orientations of each layer magnetisations.

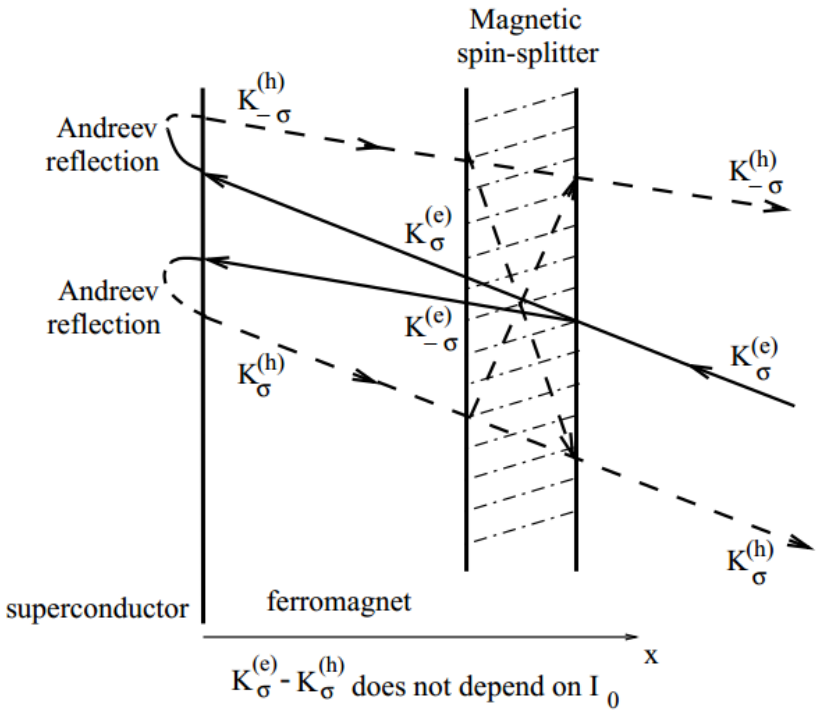

Figure 2.22: Sketch taken from [16] of the scattering of an electron at the interface between a superconductor and a ferromagnet with an inhomogeneous magnetisation. It shows the Andreev reflection and spin-splitting scattering in the region of the inhomogeneity. The reflected hole is a mixed state with both spin-up and spin-down components as a result.

2.4.4 Previous experimental work on the long range proximity effect

Some particularly interesting experiments have taken place in the last few years, all of which are building on previous knowledge and the theoretical models detailed above, to gain a clearer picture of the long range proximity effect in SFS junctions. Reports on measurements of temperature dependence of the critical current in Josephson junctions consisting of a conventional superconductor and a weakly ferromagnetic interlayer were presented by Ryazanov *et al.* in 2001 [59]. They found that I_c increased with decreasing temperature, however found a maximum at specific thicknesses, followed by a strong decrease to zero, and then rises again. They describe that this can only be explained by assuming that the junction changes from a 0-phase state to a π-phase state at low temperatures, which agrees with theoretical predictions that the triplet Josephson effect provides the possibility of 0 and π junction realisation due to the different orientations of the magnetic moments of the layers [15].

The group at Royal Holloway in 2006 reported on superconducting phase-periodic conductance oscillations in ferromagnetic wires with interfaces to conventional superconductors [1]. This experiment involved an Andreev interferometer using aluminium as the conventional s-wave superconductor and a ferromagnetic part made of holmium; a rare earth metal with an intrinsic helical magnetic structure (explained in more detail in the previous subsection). The geometry of the measured structure can be seen in figure 2.23 (a). By observing conductance oscillations as a function of the superconducting phase difference, and excluding the singlet proximity effect by making the length of the ferromagnet at least one order of magnitude larger than the singlet magnetic coherence length, the experiment showed unambiguous proof of coherent electron transport through a ferromagnet. The oscillations shown in figure 2.23 were seen in samples with holmium wires up to 150nm in length, and were explained as the result of the long range triplet proximity effect predicted in [14].

The results by Robinson *et al.* in 2010 detected a long-ranged supercurrent in

the ferromagnetic layer of an SFS junction, using the intrinsic conical structure of holmium for the inhomogeneous ferromagnet, coupled to a homogeneous ferromagnetic barrier [17]. The experiment was based on the work published in 2006 suggesting a spin-triplet Josephson junction consisting of two spin-singlet superconductors coupled to a ferromagnetic tri-layer $F_L/F_C/F_R$ [15]. Cobalt was used for the F_C layer, and holmium was used for the F_L and F_R layers so the magnetisation was non-collinear, providing the necessary inhomogeneity for the spin-triplet configuration, the schematic design of the junctions used can be seen in figure 2.24 (a). This experiment was designed to compare the decay length of the supercurrent from spin-triplet pairs in the homogeneous F_C layer, with a simple homogeneous S/F/S junction made with the same material and thickness. Figure 2.24 (b) shows one of the results obtained from the Nb/Ho/Co/Ho/Nb junctions. The graph compares the results with the Co barrier junctions and outlines the substantially longer decay length, suggesting the supercurrent is passing through the composite Ho/Co/Ho barrier as if it were non-magnetic. It was found that the long range effect required a specific thickness of holmium consistent with spin-triplet proximity theory, enabling the control of the electron pairing symmetry by tuning the degree of magnetic inhomogeneity through the thickness of the holmium injectors.

An interesting set of results presented recently from the group headed by Professor Birge at Michigan State University [19]. They reported on a long range supercurrent in Josephson junctions consisting of two niobium electrodes separated by a strong ferromagnetic cobalt layer and two thin layers of the weakly ferromagnetic alloy PdNi (they also replaced the PdNi layers with CuNi, with a similar outcome). Figure 2.25 (a) shows a schematic diagram of the Josephson junction tested in this experiment, with a detailed sequence of the internal layers labeled 'F'. The junction consists of two cobalt layers used to suppress the conventional spin-singlet Josephson supercurrent, separated by a thin ruthenium layer to induce antiparallel exchange coupling resulting in a nearly zero net magnetisation of the junction. The magnetic inhomogeneity used in their design (discussed in more detail in the earlier subsection) was supplied by two thin layers of the weakly ferromagnetic PdNi alloy inserted between the niobium and cobalt layers. These layers were

used for inducing the spin-triplet pair correlations, and by varying the thickness of these layers, they were able to control the strength of the triplet correlations. The copper layers are present firstly to isolate the PdNi and Co layers magnetically so the magnetization of the PdNi layers is not exchange coupled to the Co layer, and secondly for practical reasons as the quality of the sputtered Co is higher when sputtered onto Cu. Figure 2.25 (b) shows the product of the critical current and normal state resistance, I_cR_N plotted against total cobalt thickness D_{Co} for a series of samples with a fixed PdNi layer of 4nm. It shows there is no discernible decay of I_cR_N for D_{Co} >12nm, in sharp contrast to the very fast decay observed in similar junctions without the alloy layers carried out in [60]. It is important to note from the graph when D_{Co} = 20nm, that I_cR_N is over 100 times larger in the samples with the PdNi layer. The long range character of the Josephson current suggests strong evidence for its spin-triplet nature, as predicted by the theory mentioned in the above subsection. At large thicknesses of the PdNi layer, I_cR_N will decrease suggesting the destruction of the spin triplet correlations due to the spin memory loss in this layer, the spin memory length in PdNi being approximately 2.8nm.

The paper by Keizer *et al.* reported on a Josephson supercurrent through a strong, fully spin polarised ferromagnetic half metal CrO_2, inferring the generation of a spin-triplet supercurrent [2]. This experiment consisted of two s-wave superconducting $NbTiN$ contact leads deposited onto a CrO_2 layer, which was epitaxially grown onto an insulating TiO_2 substrate as shown in figure 2.26 (a). On cooling the samples to below 10K, they found a Josephson current between the two superconducting electrodes which can only pass through the ferromagnetic film over a distance greater than half a micron as shown by the result in figure 2.26 (b), and which depends on the orientation of the magnetisation in the ferromagnet. It was also found that with increasing temperature, the maximum supercurrent I_c decreases and disappears at a temperature comparable to the superconducting transition temperature T_c of the $NiTiN$ film. Using a half metal with an absent spin-down band leads to the conclusion that the conversion from the singlet to the triplet state must happen at the interface. However the large spread in the critical current between samples indicates that the process responsible for the

conversion is not very well defined, and the different properties of the interfaces provide variations in the efficiency of the singlet-triplet conversion.

An interesting result was presented recently that investigated long range coherent transport in high temperature superconductor/half metallic ferromagnet junctions [20]. They found quasiparticle and electron interference effects in the conductance across the SF interface that shows the long range propagation across the half metallic ferromagnet. Figure 2.27 (a) shows a schematic of the setup used in the experiment, and the differential conductance revealing a series of oscillations that appear symmetrically in a wide range of voltages that exceed the superconducting gap. They argue that these are due to electron and quasiparticle interference effects, and are composed of two distinct sets of geometrical resonance; a long period set which they identify as Tomasch resonances [61] [62] and a short period set which due to McMillan-Rowell resonances [63] [64].

These can be described with the use of figure 2.27 (b), showing the Tomasch resonances occur due to the quasi particle interference on the S side of the interface, and the interference is between an incident electron like quasiparticle and its hole like counterpart which is Andreev reflected from the interface.

The McMillan-Rowell resonances occur on the non superconducting side of the interface. The incident electron is Andreev reflected as a hole at the interface, this hole then travels a distance d_N to the opposite interface and after being normally reflected, will be Andreev reflected from the superconducting interface for a second time. This returns the hole to its original electron state and will interfere with the first incident electron. For this to occur, the McMillan-Rowell resonance requires that the phase coherence induced by the energy gap between the incident electron and Andreev reflected hole is preserved.

The physics of this experiment is made more interesting with the use of a half metallic ferromagnet. The quasi particle normally transmitted as a hole due to Andreev reflection is forbidden as the spin will oppose the original majority spin of the incident electron. The McMillan-Rowell resonance is therefore not expected to occur within the half metallic ferromagnet, and they conclude that the only explanation of this result is by considering a spin flip process at the interface that

induces in the Andreev reflected hole the same spin as the incident electron, and that the phase coherence between the incident and reflected particles occurs over 30nm, which is considerably larger than ξ_F.

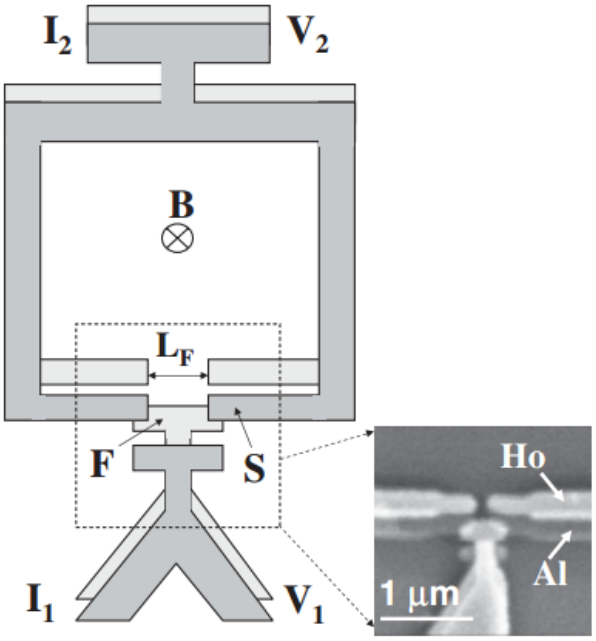

((a))

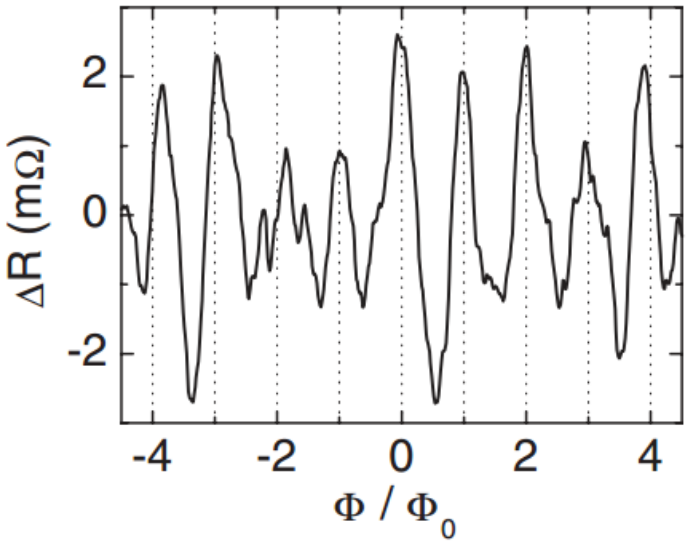

((b))

Figure 2.23: (a) shows a schematic diagram and SEM micrograph of sample measured in [1] producing the magnetoresistance oscillations as a function of normalised external flux through the loop shown in (b).

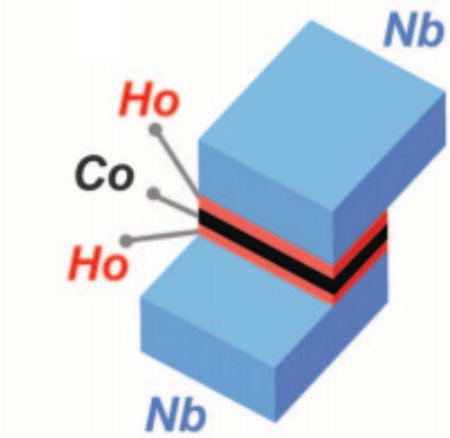

((a))

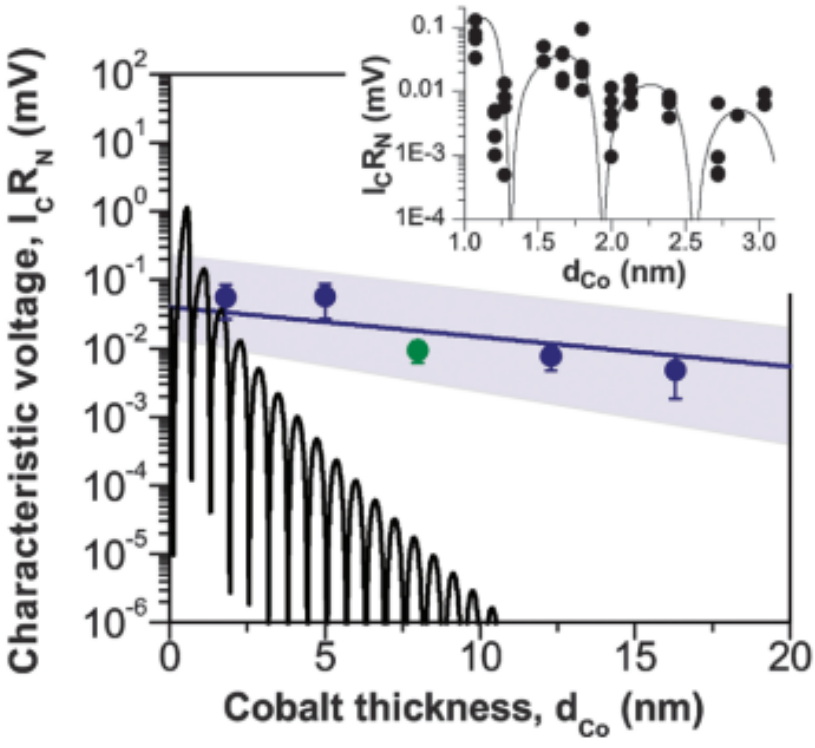

((b))

Figure 2.24: Image taken from [17], with (a) representing the device fabricated in this experiment consisting of two superconducting niobium electrodes separated by the Ho-Co-Ho trilayer. (b) shows the slow decay of the characteristic voltage of the structure shown in (a) versus cobalt barrier thickness d_{Co}. The inset shows comparative data showing the behaviour of a similar experiment of Nb/Rh/Co/Rh/Nb junctions taken from [18].

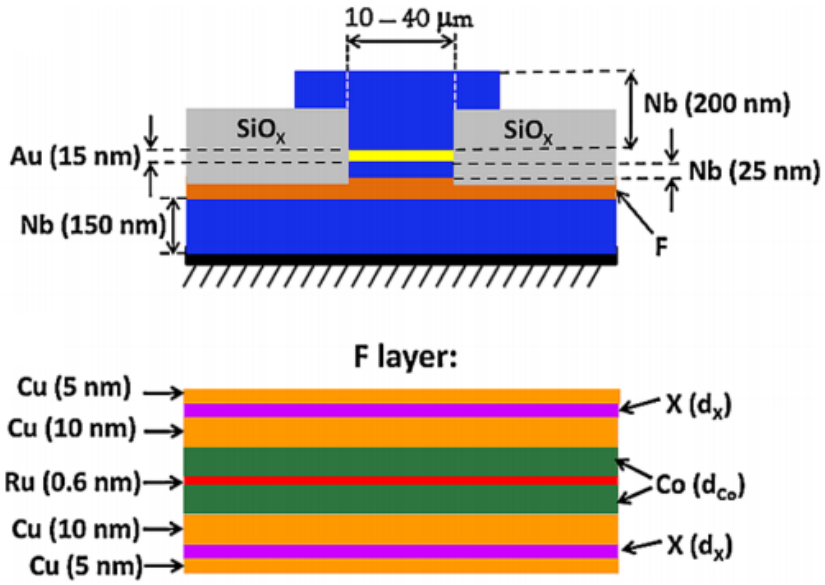

((a))

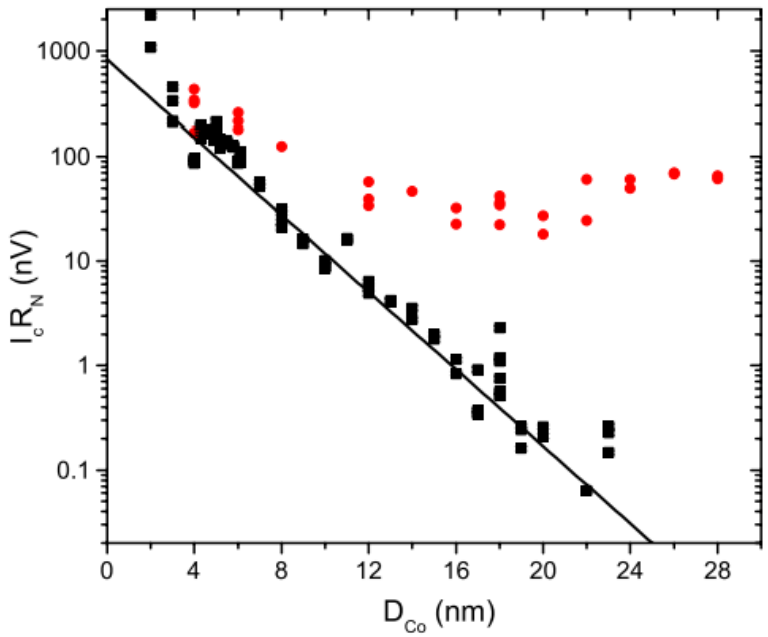

((b))

Figure 2.25: Schematic cross section of the Josephson junctions taken from [19] (above). Lower image shows the detailed cross section of the layers inside the Josephson junctions labeled F. The layers labeled X are represented by the ferromagnetic alloy $Pd_{0.88}Ni_{0.12}$ (or $Cu_{0.48}Ni_{0.52}$ but that is not discussed here). Figure (b) shows the results taken with the junctions shown in (a), and shows the product of the critical current and the normal state resistance I_cR_N as a function of the total cobalt thickness, $D_{Co} = 2d_{Co}$. The red circles represent a $PdNi$ thickness of 4nm, and the black squares represent a sample with no $PdNi$ layer. It is important to note the critical current hardly decays when the cobalt layer is in the range of 12-28nm.

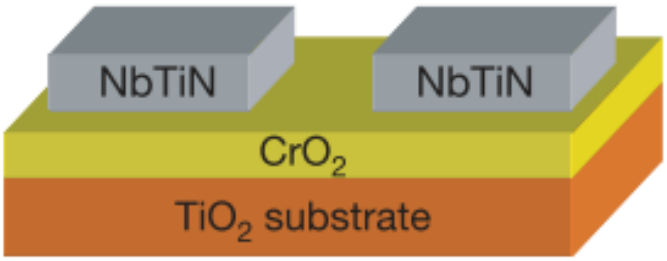

((a))

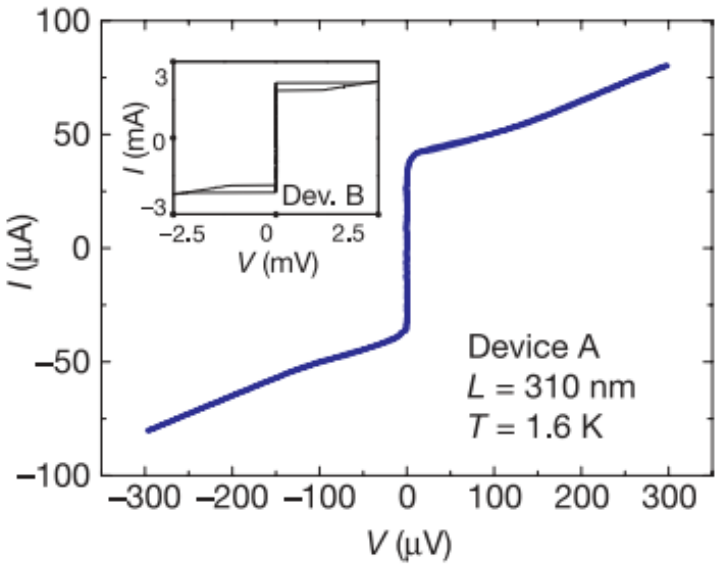

((b))

Figure 2.26: (a) shows a schematic illustration of the device studied in [2], producing a zero resistance supercurrent in the I-V curve shown in (b).

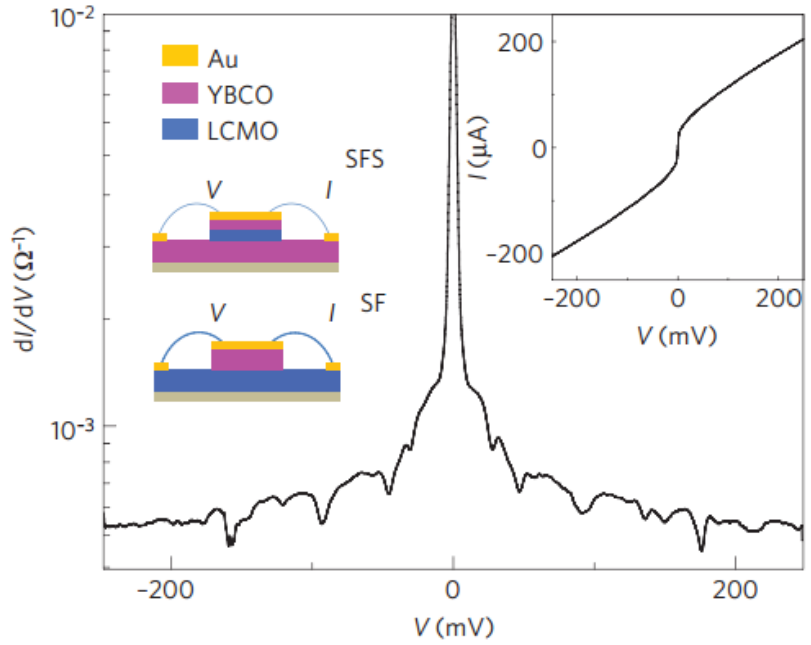

((a))

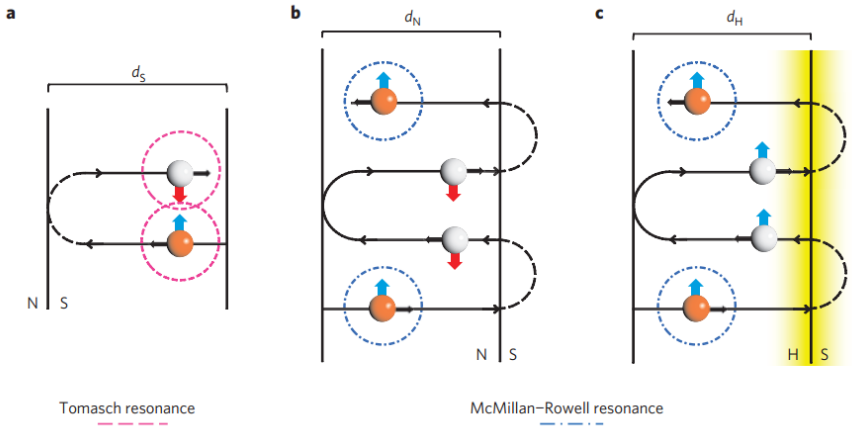

((b))

Figure 2.27: (a) shows the differential conductance $\frac{dI}{dV}$ as a function of the voltage V for the SFS tri-layer shown inset. (b) taken from [20] shows a schematic representation of the Tomasch resonance at the SN interface (left). McMillan-Rowell resonance at the SN interface (centre) and the McMillan-Rowell resonance at the superconducting/Half metallic ferromagnet interface (right). The interfering particles are enclosed in the dashed circles, with the McMillan-Rowell resonance only occurring with the presence of the spin active interface that flips the reflected particles' spin (right, shaded).

2.4.5 Theory of the long range proximity effect in a ferromagnetic vortex

An excellent contribution to the field of the long range proximity effect was presented recently, that argued the realisation of triplet superconductivity in hybrid SF structures with a ferromagnetic vortex configuration and demonstrates that this junction can sustain a supercurrent that can be directly measured experimentally [21]. The authors describe the model of a ferromagnetic vortex partially covered by two superconducting electrodes as shown in figure 2.28 and employ the quasi-classical Usadel equations for energy integrated matrix Matsubara-Green functions to analyse the superconducting correlations that penetrate into the vortex from those electrodes. The most important observation to note is the decay length of each component, most of which decay in the vicinity of the interface. However it is the component that is independent of the exchange field h which is of interest in this project, as this can penetrate into the ferromagnet over a much longer length scale providing the temperature remains low. It should also be noted that they consider tunnel barriers at both SF interfaces implying a weak electron tunneling regime. An important result taken from the paper includes evaluations of the Josephson critical current of the SFS system, as they note that it is in the measureable range and has potential to be tested by experiment. Considering a symmetric situation with $\Delta_{1,2} = |\Delta|$ and by assuming the relevant thouless energy $\epsilon_{Th} \approx \frac{D}{4R^2}$ remains smaller that the superconducting gap $|\Delta|$. Then in the limit $T << \epsilon_{Th}$ it is found that

$$I_c \approx \frac{D^2 \epsilon_{Th}}{edh^2 r_1 r_2 \sigma} \tag{2.4.1}$$

while for $\epsilon_{Th} << T << |\Delta|$ the Josephson current follows the standard exponential dependence on temperature

$$I_c \approx \frac{TD^2}{edh^2 r_1 r_2 \sigma} e^{-L\sqrt{\frac{2\pi T}{D}}} \tag{2.4.2}$$

where L is the distance between the two SF contacts. The result for I_c in the SFS

system turns out to be $\approx \frac{\epsilon_{Th}^2}{h^2}$ smaller than that for a conventional diffusive SNS junction with identical geometry. It was also suggested that the critical current can be further increased by a proper choice of the system parameters, for $T << \epsilon_{Th}$ and $d \geqslant \xi_h$ they obtain

$$I_c \approx \frac{(\frac{\xi_h}{d})^2 \epsilon_{Th}}{eR_N} \tag{2.4.3}$$

where R_N is the normal state resistance of the ferromagnetic film between the two superconducting electrodes. This equation shows that values of I_c can be reached only by the factor $\approx (\frac{\xi_h}{d})^2$ smaller than the absolute maximum $I_c \approx \frac{\epsilon_{Th}}{eR_N}$ achieved for SNS junctions. It should be noted that this maximum can be achieved with extremely thin films when $d \leqslant \xi_h$ with large values of R_N, however this would then cause other factors to arise as the formation of the vortex is thickness dependent. Interestingly, the spin triplet pair correlations predicted to survive over long distances through a ferromagnet are different from the correlations in materials such as $SrRuO_4$, as these satisfy the spin statistics theorem of quantum mechanics by having odd relative orbital angular momentum. The triplet pair correlations induced in the SF design used in this thesis have even relative angular momentum meaning they will be s-wave and able to survive in the presence of disorder, and therefore will have to be odd in frequency to ensure further quantum mechanical systems are not violated.

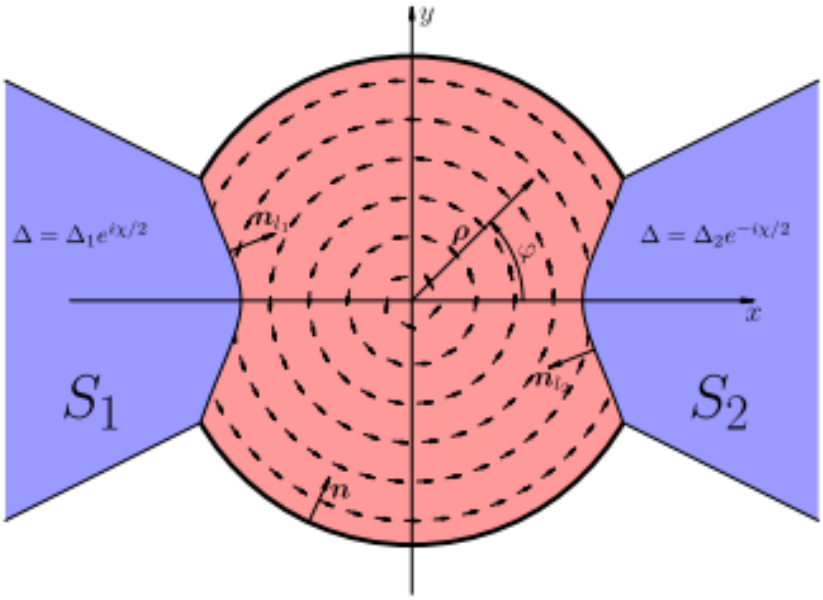

Figure 2.28: Structure of the SFS junction considered in [21], consisting of two superconducting electrodes separated by a ferromagnetic vortex. The figure highlights the superconducting order parameter Δ equals zero in the ferromagnet, while in the two superconducting terminals it is respectively $\Delta = \Delta_1 e^{\frac{i\chi}{2}}$ and $\Delta = \Delta_2 e^{\frac{-i\chi}{2}}$ with χ being the superconducting phase difference across the SFS junction.

Chapter 3

Design and fabrication of hybrid S/F nanostructures

The evolution of this section played a critical role in obtaining the results for this thesis. Fabricating a ferromagnetic disc between two aluminium leads created the initial four point sample, revealing the first of many challenges; alignment and conductance. These problems were solved by incorporating the shadow evaporation technique, however magnetic force microscopy images revealed the detrimental effect of the resultant stray magnetic material. A unique solution of a simple but powerful way to improve the shadow evaporation technique was used, by including a thin germanium layer to allow a selective undercut that would prove invaluable throughout all future designs. After developments in the calculation for the critical current, the next design involved creating arrays of SFS junctions. The issue of a delicate critical current encountered at this stage would lead to a fundamental change in the measurement setup by using a flux biased interference based system, and developing a device that could be isolated from the measurement setup eliminating the problem incurred by the current biased design of previous samples.

3.1 Fabrication techniques

3.1.1 Chip preparation

All samples were made on silicon wafers with a native oxide. Surface contamination of the 100mm wafer was removed with a four minute oxygen plasma etch as this could prevent successful deposition of the resist. The wafer was patterned with gold contact leads to allow the connection between the macroscopic measurement system and the mesoscopic structure, the design of which can be seen in figure 3.1, and shows the exposure area measuring 80μm x 80μm at the centre of each chip. The contact leads were fabricated by photolithography using a chrome and quartz photo mask and a bi-layer photo resist setup, the under layer with its faster development rate producing a large undercut. Exposing with UV light is useful as it can expose a large pattern in a short time due to all areas being exposed simultaneously, however the maximum resolution is limited by diffraction so this is only used for larger structures a few microns in size, unlike the e-beam resolution of approximately 100nm. After reaching a pressure of at least 5×10^{-6} Torr, 80nm of 99.9999% pure gold is then thermally evaporated onto the wafer, after 10nm layer of NiCr to aid adhesion. Once lifted off, the design is visually inspected for quality and cut to individual chips measuring 7mm x 7mm in size.

3.1.2 Resist deposition and electron lithography

The foundation for fabricating structures for this project is based on different electron beam lithography techniques. The first stage involves layering the substrate with two layers of resist. The base layer consists of copolymer dissolved a concentration of 14% ethylactate, and is spun onto the prepared chip to a thickness of 600nm. This layer is more sensitive to the electron beam and can therefore provide a large undercut when developed. The upper layer is made from PMMA dissolved in a concentration of 4% anisole and spun to a thickness of 200nm, providing an accurate mask by only developing the exposed areas. Both resists were baked on a hotplate at 160°C producing the structure seen in figure 3.3.

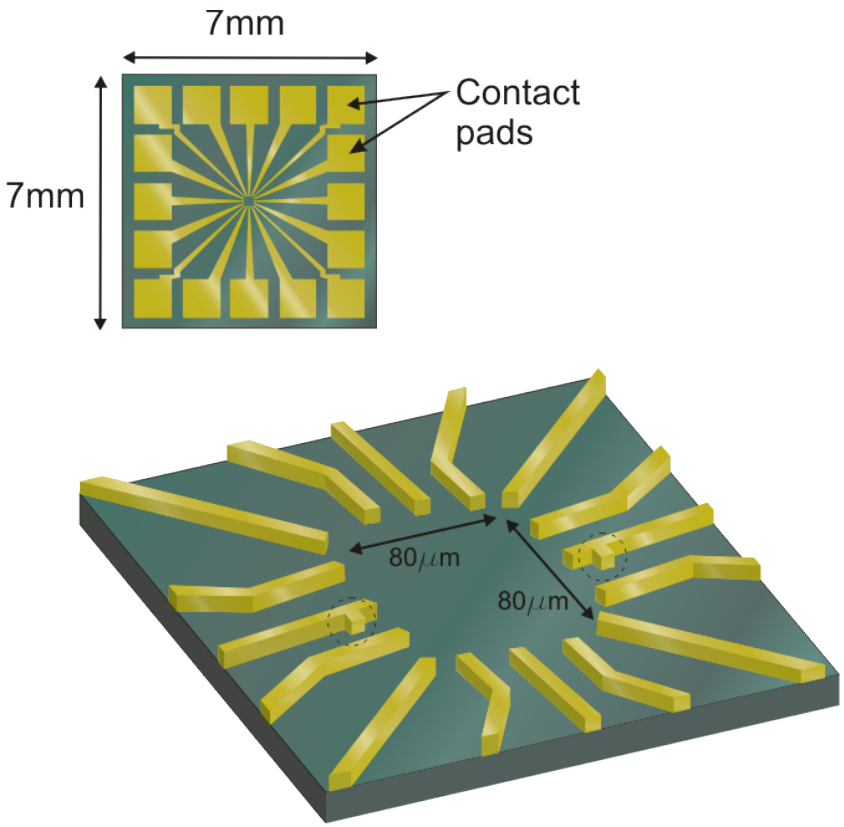

Figure 3.1: Individual silicon chip with gold contacts formed by photo lithography, revealing the 80μm x 80μm exposure area and the alignment marks used during electron lithography.

Exposing the design involves a high energy electron beam to destroy the polymer chains in the resist, increasing the solubility of the exposed areas in water and revealing a positive mask of the designed mask (alternatively, with a different type of resist the electron beam can be used for cross linking between polymer chains causing the resist to develop more slowly in the exposed areas, leaving a negative mask). During the e-beam exposure, it is important to account for the scattering of the electrons, broadening the design and leading to over exposing the resist and a distortion of the pattern. This effect known as the proximity effect is minimised by using a thin top layer of resist and by adjusting the dose on the design to account for the back scattered electrons. The designs used can be seen in the following subsections, and after exposure the chips are developed in a de-ionised solution of 7% H_2O and 93% IPA, rinsed in 100% IPA, then loaded into the evaporator after visual inspection.

3.1.3 Thin film deposition

All samples made with thin metallic films have been thermally evaporated using the evaporator shown in figure 3.2. This shows the chamber of the evaporator, which is always pumped to a pressure below 5×10^{-6} Torr using a rotary and diffusion pump. After etching with an argon plasma to remove excess resist, a large current is passed through the metal source placed on a tungsten boat at the bottom of the chamber. A thin film can be deposited on the sample placed at the top of the chamber which can rotate to allow in-situ plasma etching, and separate evaporations to take place at various angles which will prove invaluable for later designs. After the evaporation, acetone is used to remove the resist and unwanted metal with the aid of the ultrasonic bath and heating the acetone to 50°C if required.

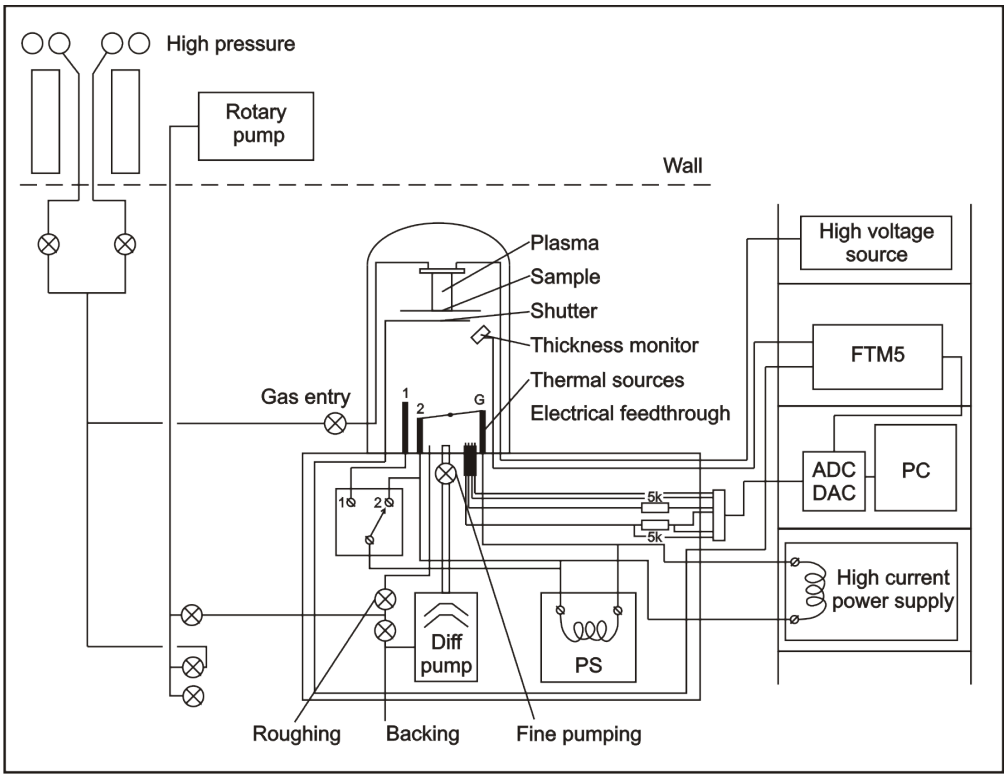

Figure 3.2: Schematic of the evaporator used for thin film deposition, achieving a vacuum of less than 5×10^{-6} Torr.

3.2 The shadow evaporation technique

To create the initial four point measurement, a ferromagnetic disc was evaporated using the positive lithography technique described above. After lift off, the resist would be re-spun and the aluminium leads would be exposed (with the use of alignment marks) to cover the disc and create the SFS junction required. This method showed two distinct problems: aligning the aluminium leads over the disc to form the junction, and conductance at the interface if alignment was achieved. These challenges were overcome by the introduction of the shadow evaporation technique [65] which naturally helped with alignment, and by evaporating the two materials in-situ without breaking the vacuum or having to re-spin the resist; solved the contact issue. The shadow evaporation is a powerful tool used throughout nanofabrication, and can be explained with the use of the diagram shown in figure 3.3. Firstly, two layers with varying sensitivity are spun onto the substrate, and the design is exposed using an electron beam. After developing the exposed areas, the two materials can be evaporated and two different angles without breaking vacuum, and the resist and excess material can be removed easily with acetone. This process was used to create the initial four point measurements, the design of which can be seen in the following subsection.

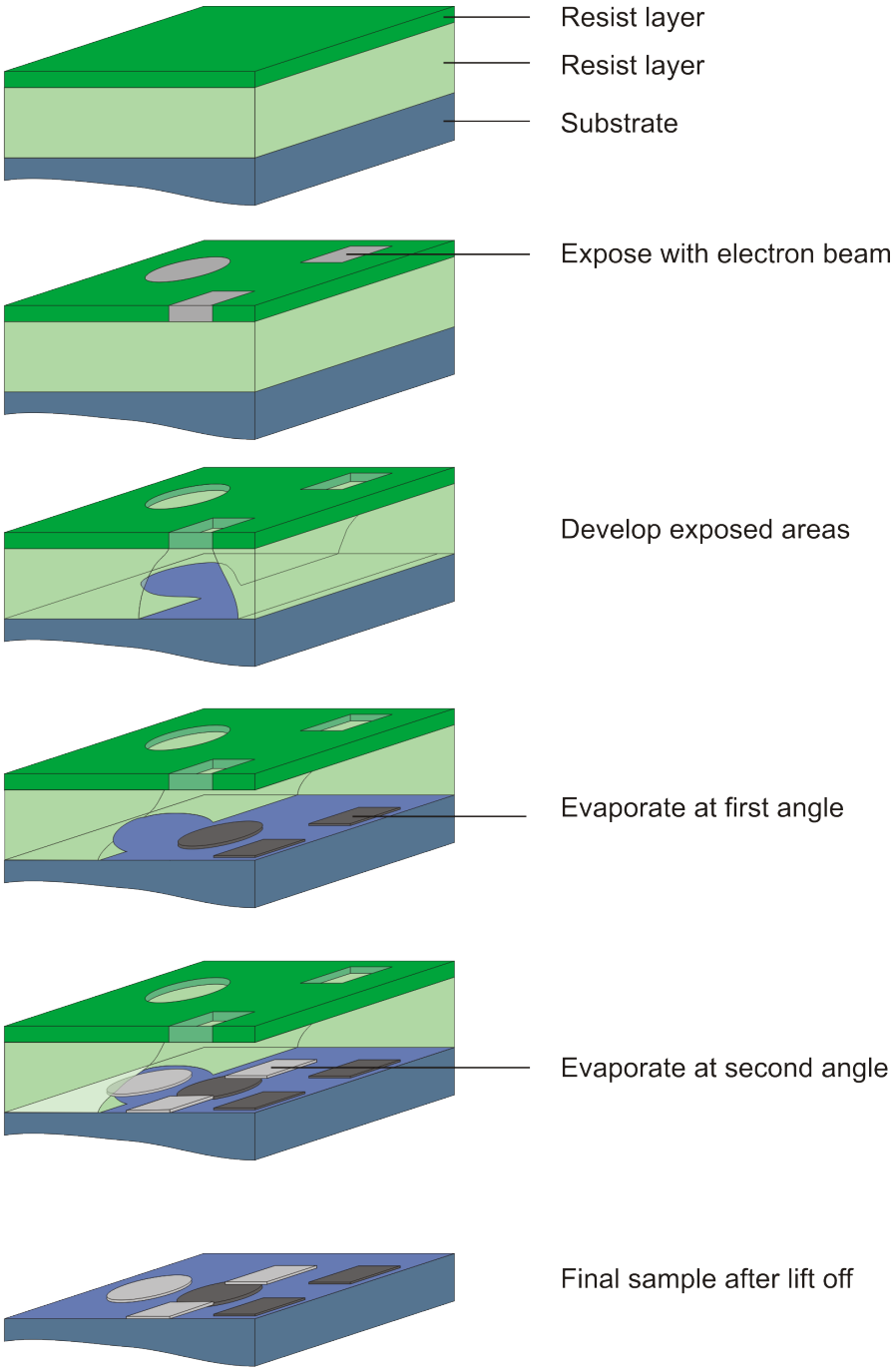

Figure 3.3: List of steps for the fabrication of two materials using the shadow evaporation technique.

3.2.1 Four point measurement design

The design for the initial four point measurement can be seen in figure 3.4. This shows clearly the use of the shadow evaporation technique and highlights the benefits of alignment. The junctions created with this design with the associated results can be seen in figure 5.5 in the results section.

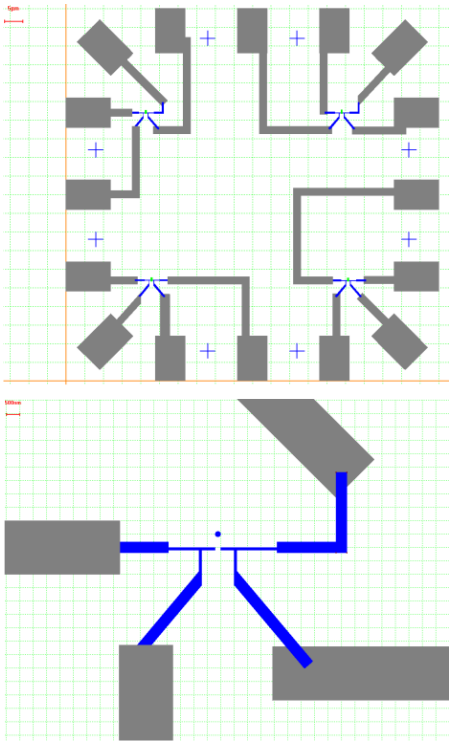

Figure 3.4: Nanomaker image of the initial four point design, using discs 300nm in diameter.

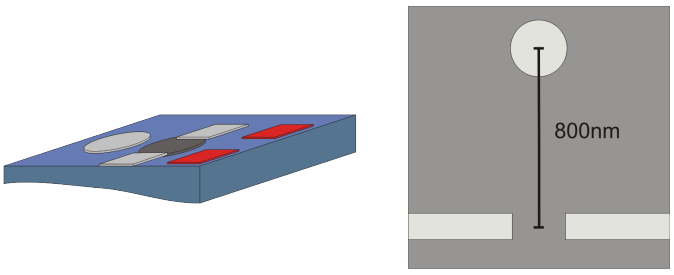

Figure 3.5: Left image shows the excess material evaporated onto the chip highlighted in red. The MFM images in the results section show the signal from this is strong, and may affect the magnetisation of the disc. The right image shows the first part of solving this issue; by increasing the separation distance and evaporating the disc at an extreme angle.

3.3 The modified shadow evaporation technique

The shadow evaporation technique solves the issues mentioned above, however causes new problems to arise. Figure 3.6 shows the second structure or 'shadow' that is naturally left on the substrate after evaporation. Although this has no contact with the junction, MFM images of the samples seen in figure 5.4 in the results section reveals the stray ferromagnetic material affects the magnetic structure of the disc. The figure shows the effect from the stray material on the tip of the microscope is enough to make the signal from the disc invisible, and as the structure of the disc plays a critical role in this project, this issue proved to be critical. This was overcome by evaporating the ferromagnetic material at an extreme angle, causing all of the material to hit the side wall of the resist. This leads to the inevitable problem of making sure the disc did not hit the resist wall, which is only possible with an asymmetric undercut created using the electron beam to remove the base resist layer. This was a non-trivial consideration as both layers of resist are sensitive to the electron beam. The new technique therefore involved introducing a thin germanium film between the two resist layers, allowing the design to be exposed into the top resist layer, and then etched into the germanium using a sulfur hexafluoride plasma. The power of this process is revealed when the sample was re-exposed, specifically selecting the areas for the undercut in the base layer while leaving the germanium mask intact. This therefore permits the user to specifically and accurately control what part of the structure in the mask is evaporated onto the substrate, allowing a single nickel disc by evaporating through whole germanium mask with the unwanted nickel deposited on the resist walls and removed at lift off. The results produced by this new process can be seen by the SEM images in the results section.

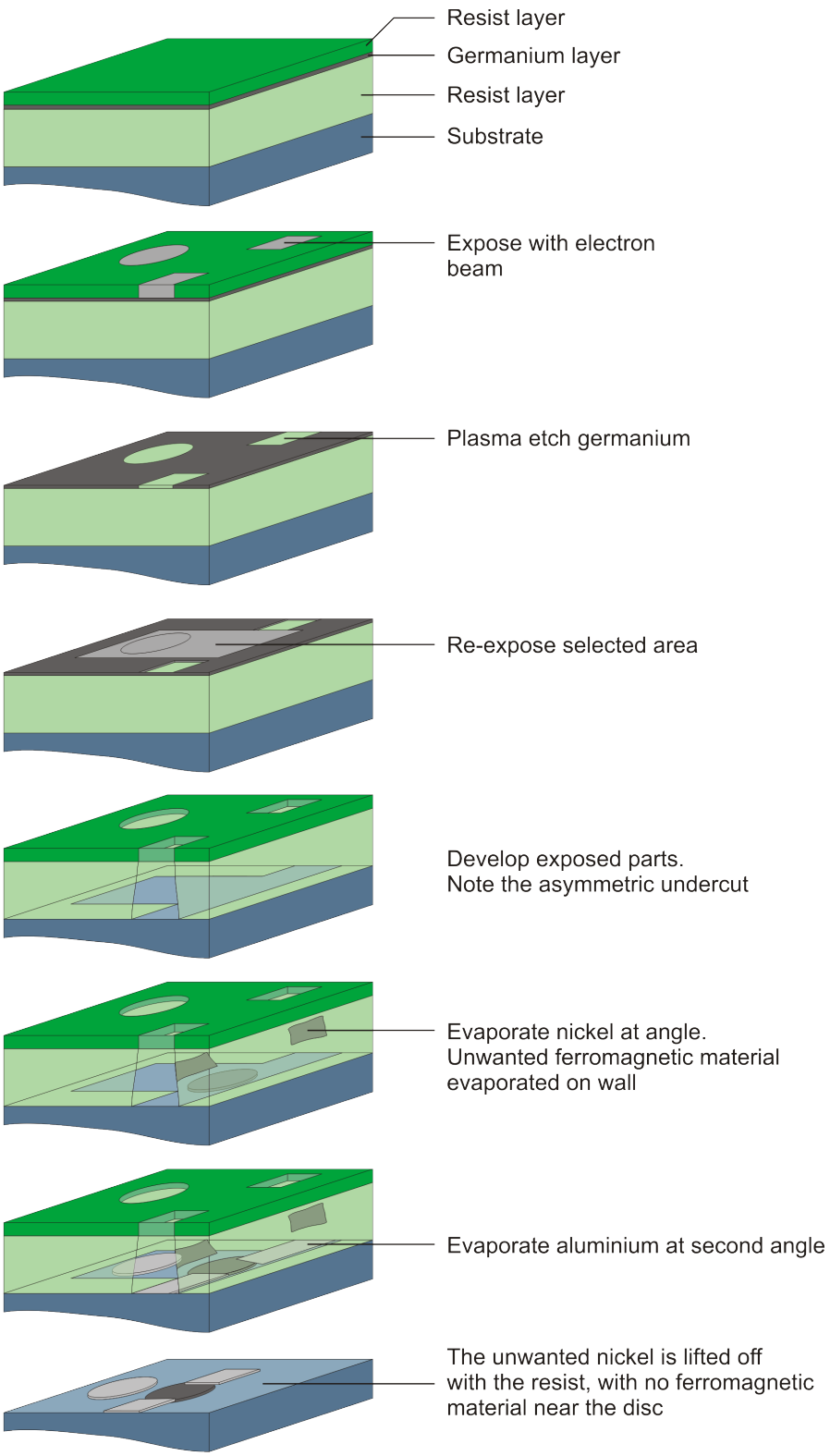

Figure 3.6: List of steps for the fabrication process using the modified shadow evaporation technique. The vital step to note is the inclusion of the germanium layer which allows for the structure to be re-exposed creating an asymmetrical undercut, and preventing the unwanted nickel from hitting the substrate.

3.3.1 Improving the four point design

The four point design was then repeated using the modified shadow evaporation technique. The design for this can be seen in figure 3.7, and reveals the designed secondary exposure for the asymmetric undercut. It is important to note the comparison of the two techniques which is highlighted in the images of the samples in the results section, and the power resulting in the selective undercut which removes all unwanted stray material.

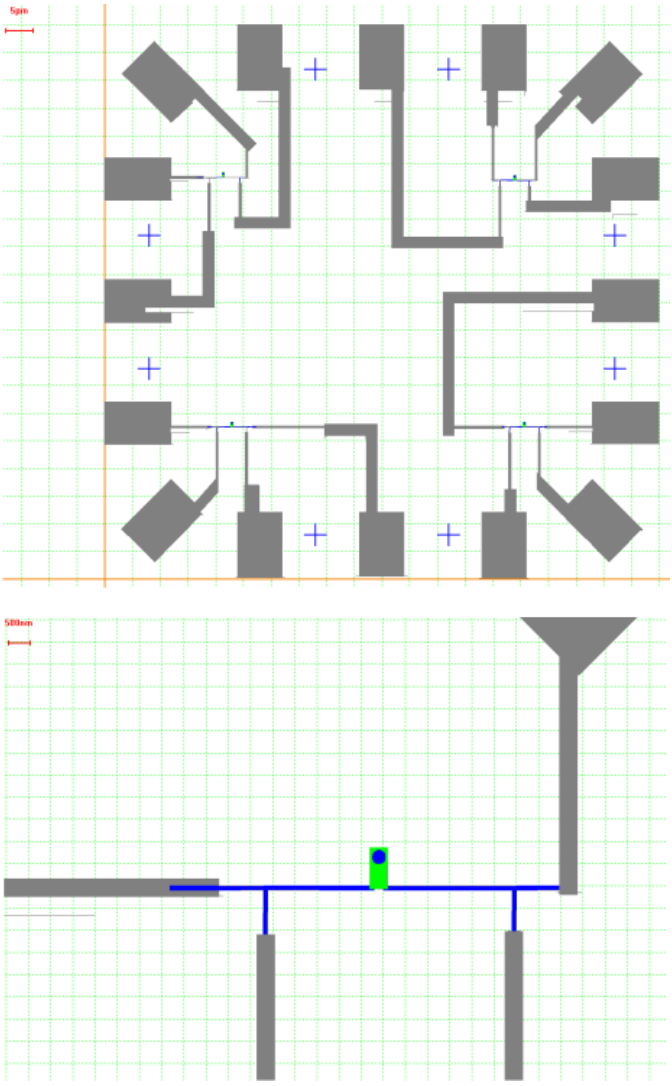

Figure 3.7: Nanomaker image of the new four point design using the modified shadow evaporation technique. The superconducting leads are moved further away from the disc, and the green rectangle shows the area re-exposed by the electron beam to create the asymmetric undercut.

3.4 SFS array design

After calculations of the critical current seen in the background section and the results from the four point measurements, an array of discs was designed to reduce the measuring current through the discs. The design for this seen in figure 3.8 also benefited from the use of the modified shadow evaporation technique to ensure the only ferromagnetic material on the substrate is the discs.

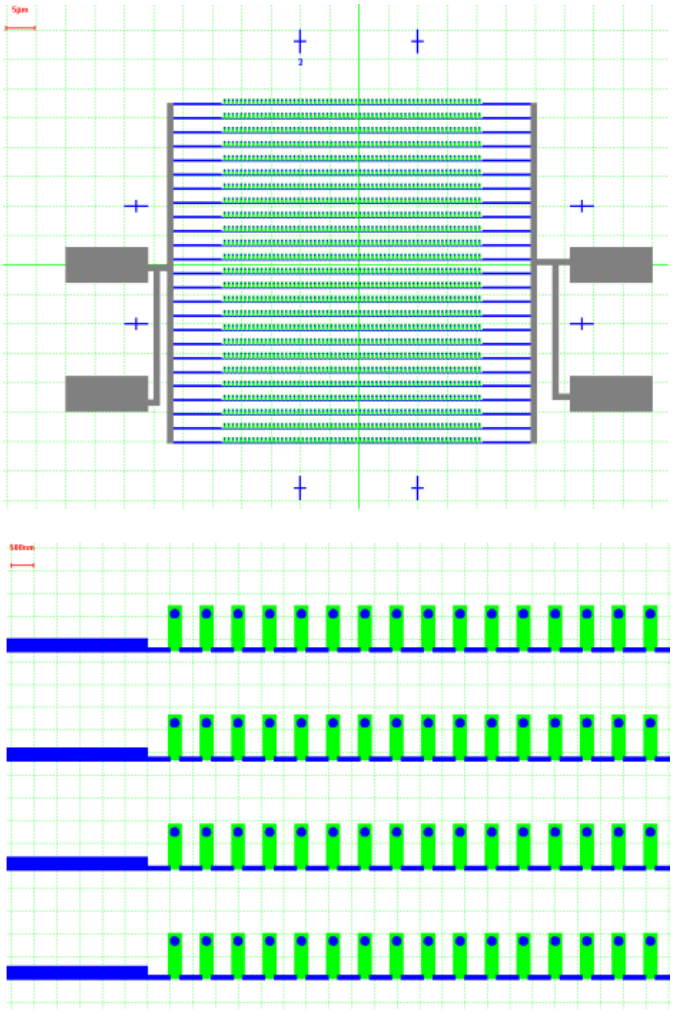

Figure 3.8: Nanomaker image of the array design, with 1064 discs 300nm in diameter.

3.5 The Hybrid Quantum Interference Device

The design progression lead to the incorporation of an Andreev interferometer with a ferromagnetic disc to create a Hybrid Quantum Interference Device (HyQUID) which benefits by using a flux biased system. The HyQUID consists of a superconducting loop interrupted with a ferromagnetic disc. The conductance of the disc will oscillate periodically as a function of the superconducting phase difference between the S/F interfaces, created by the current induced by applying a magnetic flux through the loop. The oscillations can be described by $\delta R_F = -\delta R_{0F}(1 + cos\phi)$, where the superconducting phase difference $\phi = 2\pi\frac{\Phi}{\Phi_0}$, where Φ is the magnetic flux applied through the loop and $\Phi_0 = \frac{h}{2e}$ is the flux quantum. These oscillations will provide unambiguous proof of phase coherent electron transport through the ferromagnetic vortex. The possibility of the singlet proximity effect is excluded by fabricating the distance between superconducting contacts to be two orders of magnitude larger than the ferromagnetic coherence length ξ_F. The device design can be seen if figure 3.9, with the final design presented in figure 5.12 of the results section.

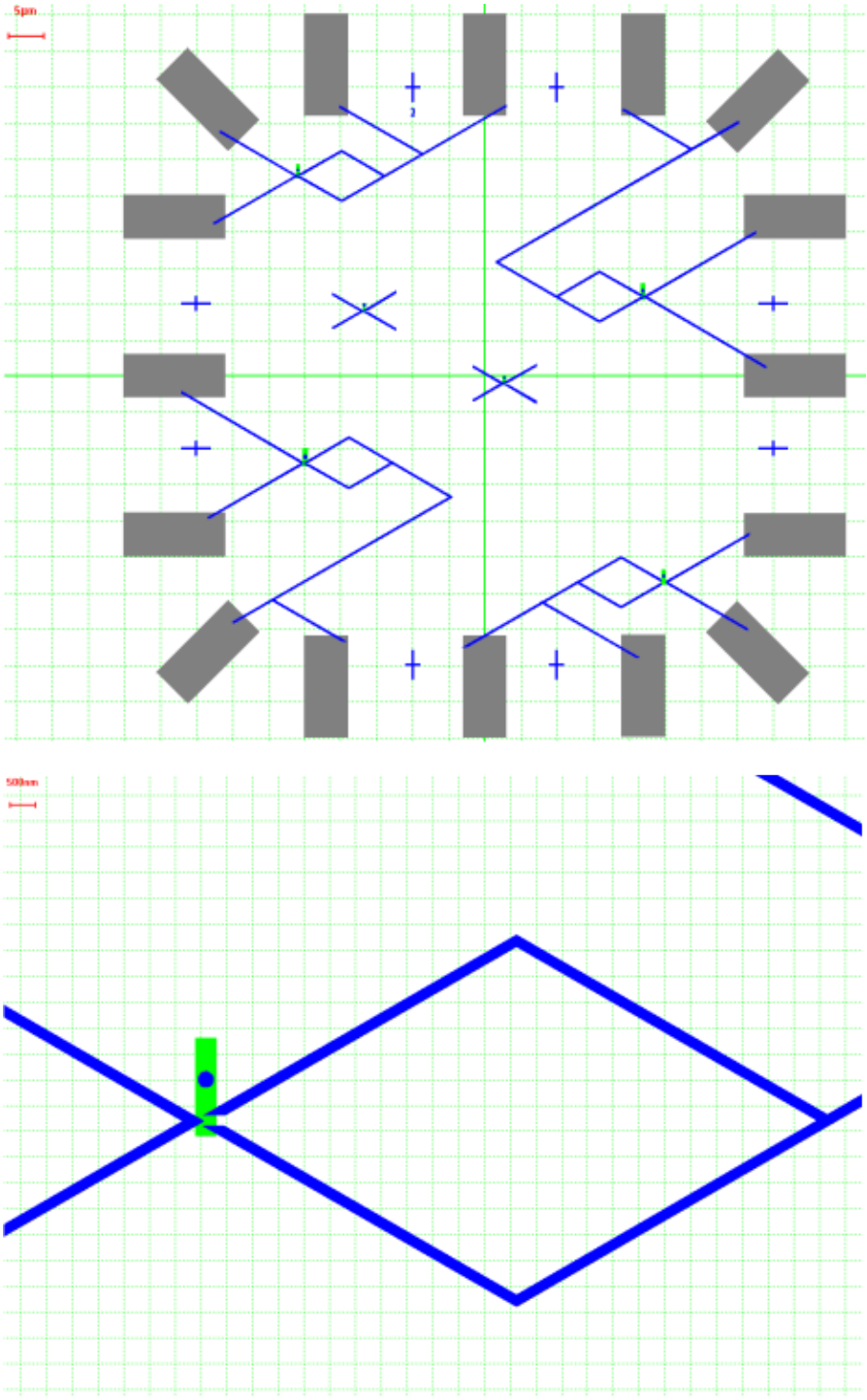

Figure 3.9: Figure showing the final HyQUID design consisting of a superconducting loop with an area of 40 μm^2 and ferromagnetic discs 300nm in diameter. The angular shape and second exposure was used to aim the new shadow evaporation technique.

Chapter 4

Experimental setup

This chapter will discuss details including the cryostat design, and the equipment setup used for collecting the data expressed in the results section. The experiments must be carried out below the aluminium critical temperature of 1.2K, but lower temperatures would be necessary to avoid thermal noise. The theoretical discussions considered in the background section must also be taken into account, as this shows the critical current in the disc is temperature dependent.

4.1 The cryostat

The fabricated samples were mounted onto a probe and inserted into a commercial Oxford Instruments Heliox He^3 cryostat with a base temperature of 240mK as illustrated in figure 4.1. The cryostat benefits from a top loading design, and can accommodate four chips per measurement which proved valuable when measuring the many samples required. The superconducting magnet situated within the cryostat was biased with a current generated by a high accuracy current source, providing a magnetic field perpendicular to the sample.

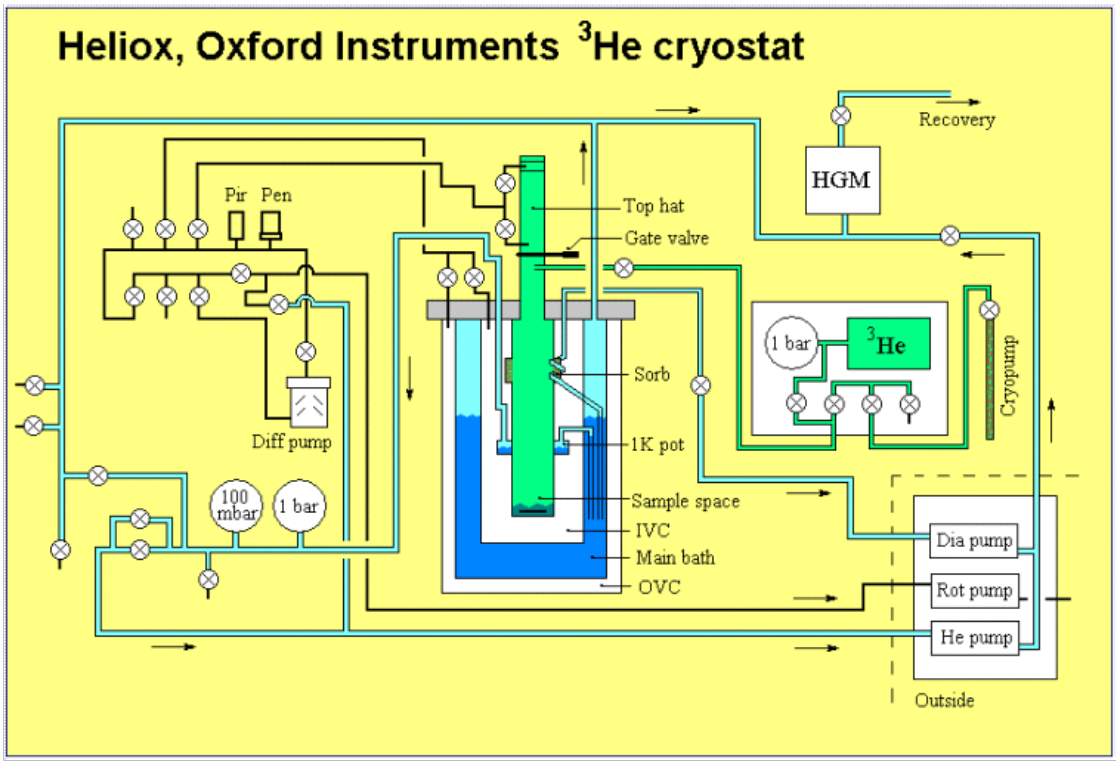

Figure 4.1: Schematic of the He^3 cryostat and associated equipment.

4.2 Measurement setup

The four point measurement setup used to probe the resistance of the interferometer is shown in figure 4.2. The measurements carried out were current biased, with a low frequency AC lock-in technique using a lock-in amplifier and a high accuracy DC source. The excitation current was generated using the internal signal generator of the lock-in amplifier with a current limiting bias resistor producing an excitation current in the range of 1-100nA. The voltage drop was measured by two voltage probes, connected to a low noise voltage pre-amplifier at room temperature. The output from this was then passed to a lock-in amplifier and recorded. The illustration of the setup shows all lines were fitted with a commercial π filters at room temperature.

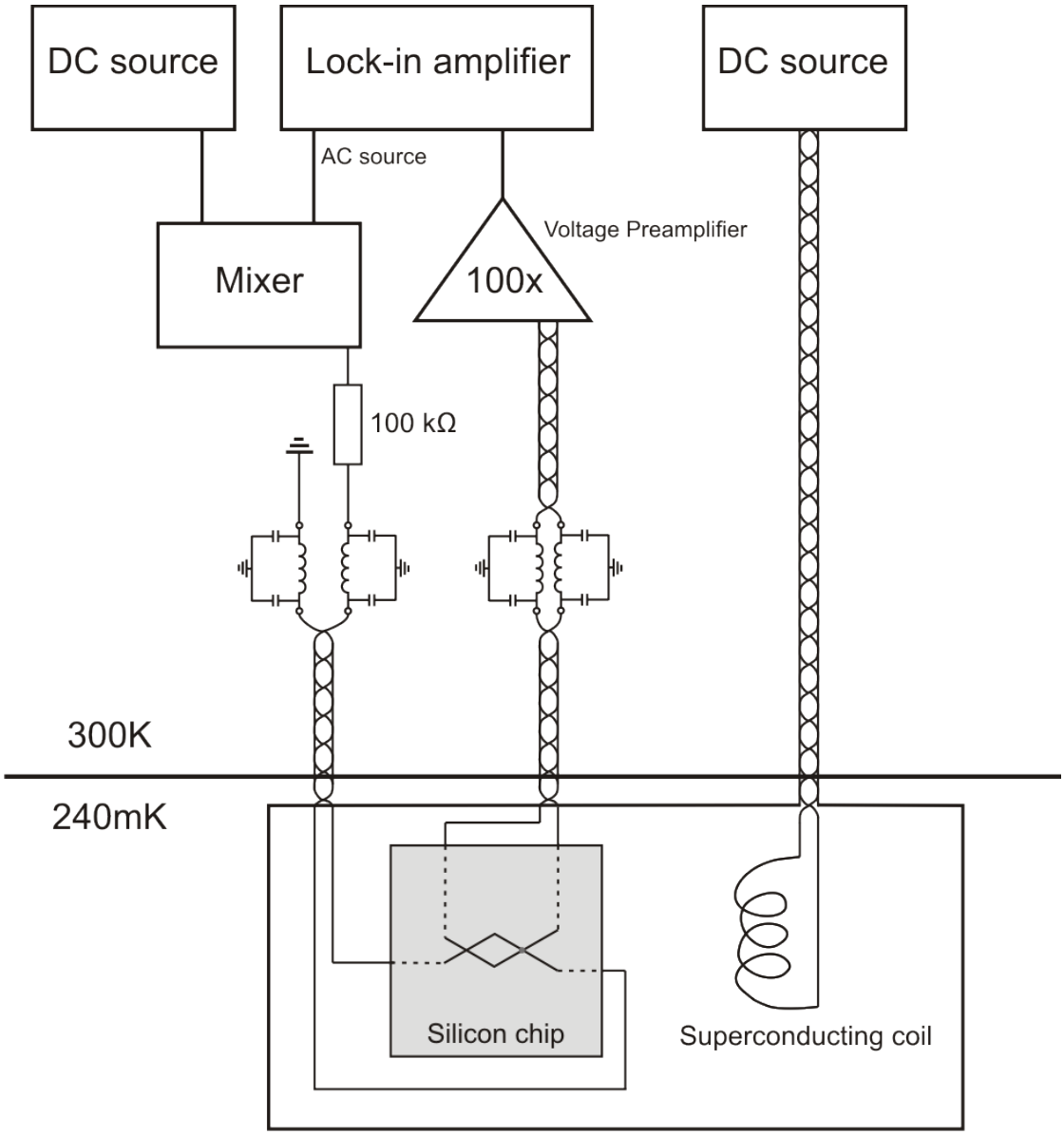

Figure 4.2: Schematic of the experimental apparatus used on the He^3 cryostat. Low frequency twisted pair wiring was used to carry out the four point measurement, and a superconducting coil was used to generate the external flux.

Chapter 5

Results and analysis

5.1 Introduction

This section will reflect the development of the experimental methods, beginning with the initial four point measurement of nanostructures fabricated using standard technology with associated issues encountered, and the solution in the form of structures produced using a new fabrication technique. The results from other developments are discussed, including the final design of a flux biased interference device used to show coherent long range effects in SFS junctions up to two orders of magnitude larger than the conventional singlet coherence length. These interference devices are the first to measure the long range proximity effect through a geometrically confined ferromagnet exhibiting a vortex structure. All samples were made using the process described in chapter three, and were measured using the experimental setup described in chapter four.

5.2 Magnetic structure of mesoscopic nickel discs

The magnetic structure of the ferromagnetic disc plays a critical role in the observation of long range quantum coherent effects. The magnetic structure is relatively well investigated in ferromagnetic discs made of soft magnetic materials such as permalloy, observed using a variety of techniques including the use of a magneto-optical Kerr magnetometer [66], time resolved scanning transmission

X-ray microscopy [67], photoemission electron microscopy [68], magnetic force microscopy [4] [69], together with analytical models and three dimensional numerical finite element simulations [70]. The diameter-thickness phase diagram was established indentifying vortex and single domain magnetic phases in permalloy [35] [36], and finite element simulations [70]; however the coherence length in permalloy was estimated to be shorter than the spatial definition of electron beam lithography. This leads to the use of high purity nickel for use within this experiment. To find the disc diameters and thicknesses where ferromagnetic vortices are stable, micromagnetic simulations and a magnetic force microscope (MFM) were used to image fabricated discs with the same dimensions as the discs used in the HyQUID. With help from the group headed by Dr Olga Kazakova at National Physical Laboratory, the topography and the local distribution of magnetic moments of the individual particles were studied by an AFM/MFM scanning probe technique using a MultiMode microscope. Images were obtained with the instrument operated in the tapping and lift modes (lift height = 40nm) using the standard Co/Cr tips (MESP, Hc 400Oe, m 10-13emu). The tips were magnetized in the direction normal to the sample. All of the discs imaged were 21nm in thickness, with a diameter of 500nm and 900nm (figure 5.1) and 300nm (figure 5.2). The disc with a 500nm diameter has a domain arrangement similar to a closed vortex state and consists of individual domains with a mostly in plane magnetisation, and a perpendicularly magnetised vortex core with a width of approximately 100nm located in the centre. This multi domained vortex state is significantly more disturbed than a classical example of the vortex state [4]. The disc shows sharp domain walls with a width from approximately 6-12nm. The disc with a diameter of 900nm has an irregular domain state. The arrangement of the domain walls in the outer part is qualitatively similar to the 500nm disc with sharp, radially aligned domain walls. The inner part is much more complex. Instead of a vortex core, it contains a number of irregular domains with an arbitrary orientation. Traces of the interaction with the magnetic tip are observed in the lower part of the scan as a set of horizontal lines. The complex domain state in both types of the particles can be explained by the dominating role of the magnetocrystalline anisotropy of nickel. The discs

with a diameter of 300nm are the most similar to the ferromagnetic section of the HyQUID, and produce far more intriguing images. These images are much closer to showing the in plane magnetisation of traditional vortices previously observed with no signs of domain walls or any form of multi domain nature. In the lower image of figure 5.2, a clear dark sport is visible just off centre. However as discussed in the *background* section, the general drawback of the magnetic force microscope is the resolution, proving difficult to find a definitive core in the centre of the disc. From all of the images taken, it is clear that the magnetic structure of the discs needed to be considered in one of three states; the vortex state, the multi domain vortex state, or the single domain. The effects of each of these on the observation of the long range proximity effect are discussed in a later subsection.

It is important to consider the effect of the magnetic flux generated by the core of the magnetic disc, especially for the induced oscillations of the interference device. The magnetic flux generated from the core can be represented by $\phi_{core} \approx 4\pi \mathbf{M} A$ where $\mathbf{M} \approx 600$ Gauss is the magnetisation and A is the surface area of the core on the disc, with a diameter of approximately 10nm. This produces a value for $\phi_{core} \approx 6 \times 10^{-17}$Wb, which is two orders of magnitude less than the value of one flux quantum $\phi_0 = 2 \times 10^{-15}$Wb and therefore have a negligible contribution to the observed oscillations.

Another important consideration involves the relative orientation of the aluminium leads with respect the varying magnetisations of the disc. Figure 5.3 (a) shows the MFM image of a nickel disc, with the arrows highlighting the domain walls that form the closure domain configuration. Figure 5.3 (b) shows the MFM image with two different disc orientations, and the arrows representing superconducting lead placement. As explained in the *background* section, the ferromagnetic inhomogeneity at the interface is critical in generating the triplet component required for the long range effect. These images clearly shows the relative orientation of the leads with respect to the domain walls could have a large contribution to the observed effects.

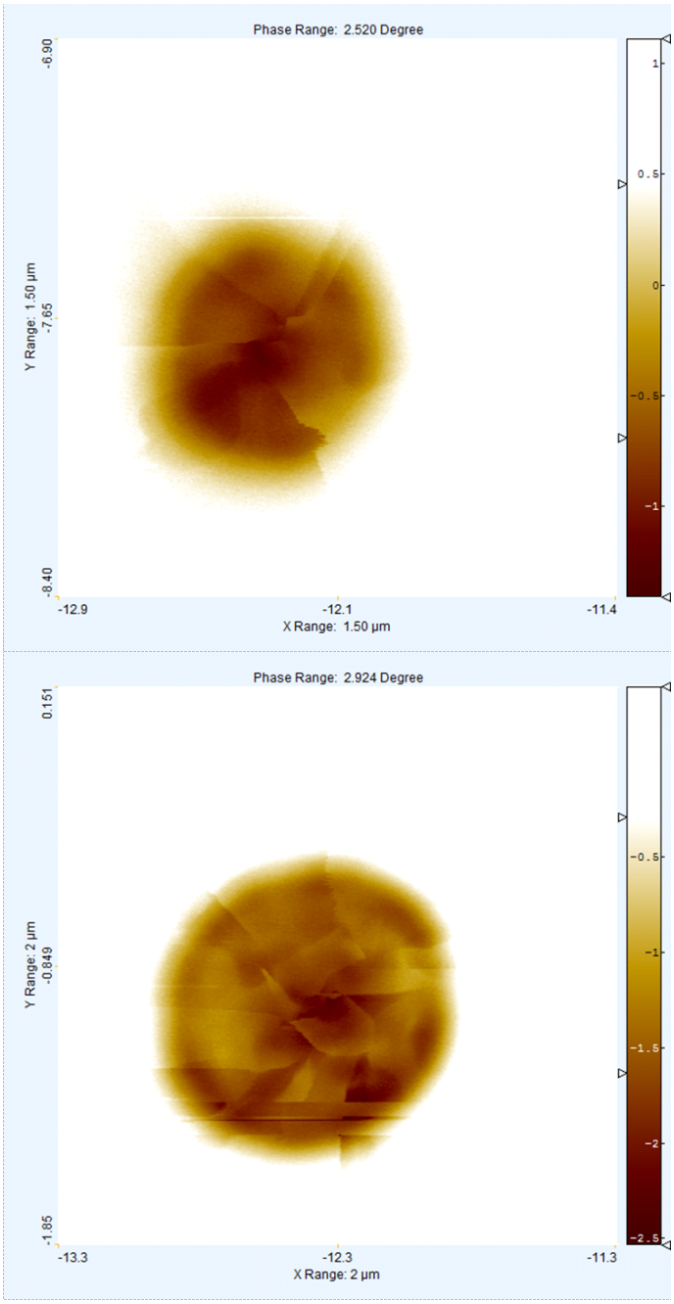

Figure 5.1: MFM measurements revealing the local magnetisation of two discs; 500 and 900nm in diameter and 30nm in thickness measured at room temperature with zero applied magnetic field. The image shows the 500nm disc (above) has a multi domain vortex state with mostly in plane magnetisation and a perpendicular core. The domain walls can be seen along the radius of the disc, and are highlighted on figure 5.3. The disc 900nm in diameter has a more complex inner section with an arbitrary domain orientation, with outer domain structure similar to that in the 500nm disc. With the MFM in tapping mode, the presence of a force gradient causes a change in the resonant frequency of the tip, and therefore changes in the phase response. It is the changes of the resonant properties that are used to obtain information on the samples' magnetisation. The scale bar on the right represents the change of the cantilever phase.

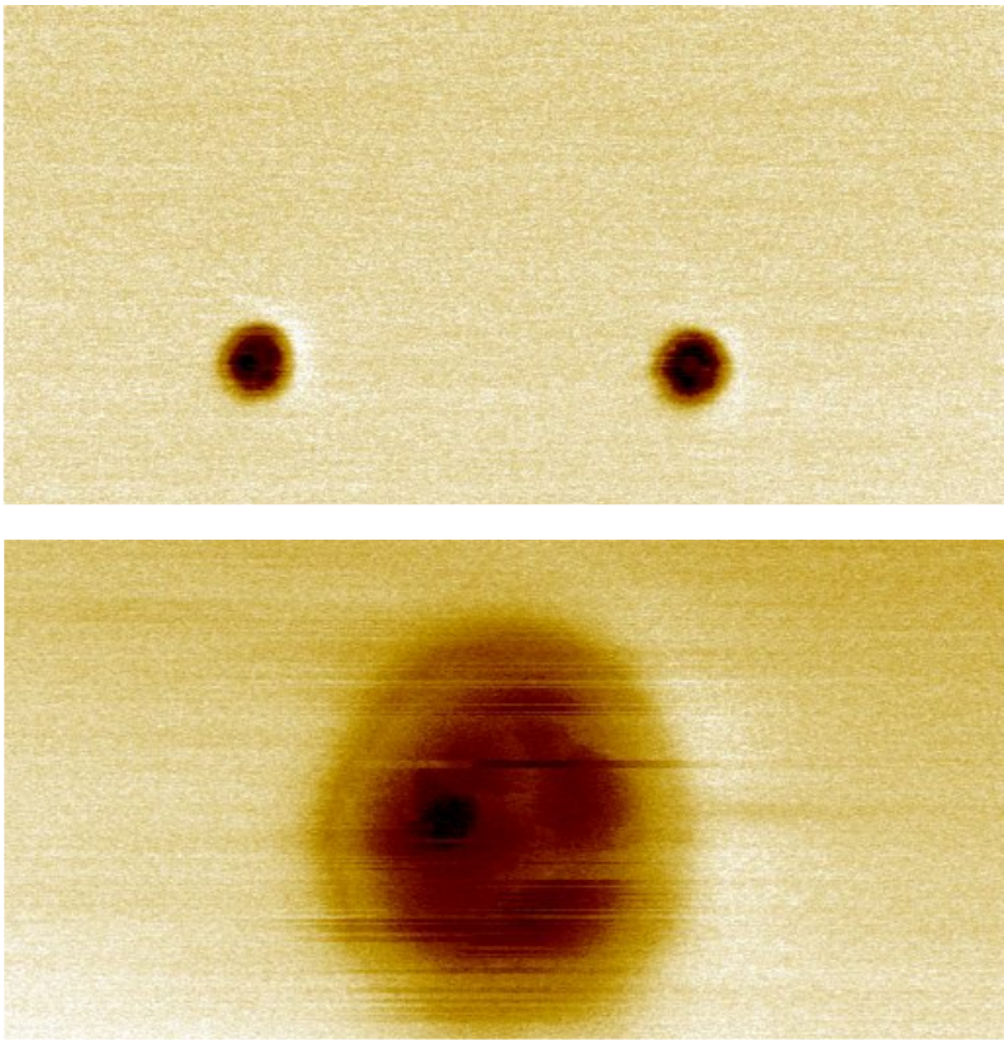

Figure 5.2: MFM images of nickel discs 300nm in diameter and 30nm thick, measured at room temperature with zero applied magnetic field. When comparing the images to figure 5.1, these discs show evidence of magnetic vortices as they do not show any form of domain walls, and no stray field characteristic of discs with a single domain such as in figure 5.32. This shows that the local magnetisation of the disc is vortex like, and lies in plane, parallel to the surface of the substrate.

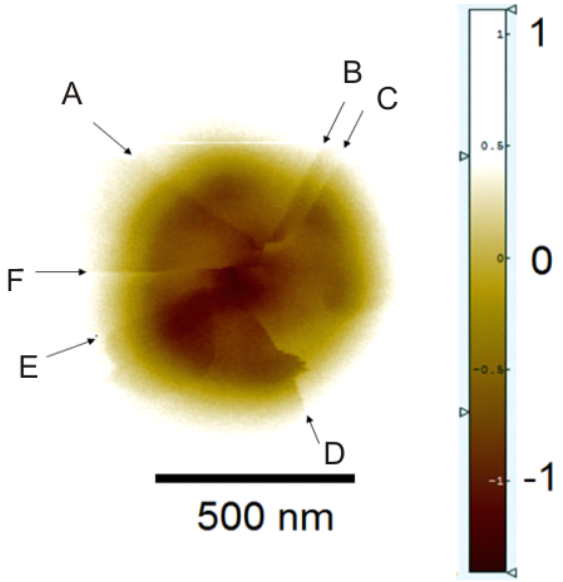

((a))

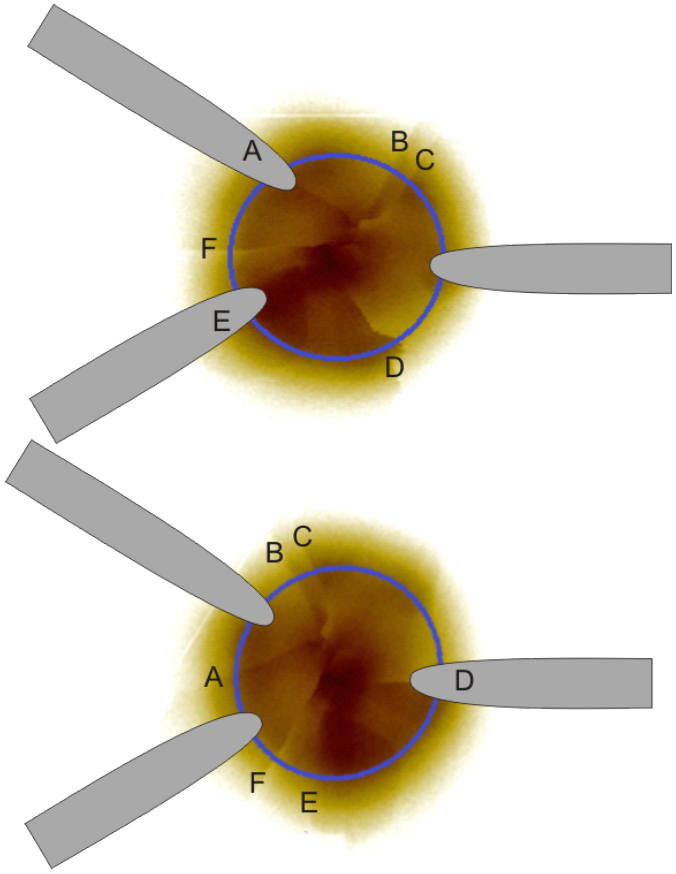

((b))

Figure 5.3: (a) shows the MFM image of the 500nm nickel disc taken from figure 5.1, where the domain walls that help form the closure domains have been lettered. The scale bar on the right is the change of the cantilever phase. (b) shows a possible outline of the disc (blue) with two possible configurations of the lettered domains walls relative to the added superconducting leads (grey). The magnetisation at the SF interface is critical for the observation of the long range proximity effect, so this would have a large contribution to the variety of observed results.

5.3 The four-point measurement with current biased SFS nanostructures

5.3.1 SFS nanostructures fabricated using the standard technique: problem with stray magnetic fields

The first experiments in search for the long range proximity effect consisted of designing and fabricating a single ferromagnetic disc with a vortex structure connected to superconducting leads to form a four point measurement. The four point measurement is the first technique to be considered as this involves a current biased SFS junction with the exclusion of the contact leads' resistance enabling the search for the critical current. The major obstacle of contact and alignment was overcome by using the traditional shadow evaporation technique as described in the *fabrication* section. The initial structure was created by the angular evaporation of nickel, then evaporating aluminium perpendicular to the substrate to create the sample shown in figure 5.5 (a). This two-angled evaporation inevitably creates a 'shadow' of material consisting of nickel resulting from the first evaporation.
The effect of this unwanted nickel on the disc revealed an important issue that required careful consideration. Figure 5.4 (a) shows an atomic force microscope (AFM) image of a five disc sample made with the traditional shadow evaporation technique that was not measured however is used to highlight the effect of the unwanted nickel on the magnetic tip. The MFM image shown in figure 5.4 (b) clearly shows the signal from the leads is large enough to make the discs invisible, and is therefore likely to have a significant effect on the nickel disc. This lead to the implementation of the improved shadow evaporation technique before the single disc could be measured, as the magnetisation of the disc is critical for the outcome of this project. The images of the samples and results taken after this method was introduced can be seen in the later subsections.

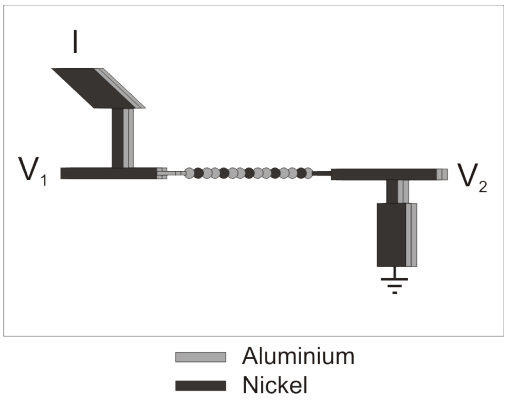

((a))

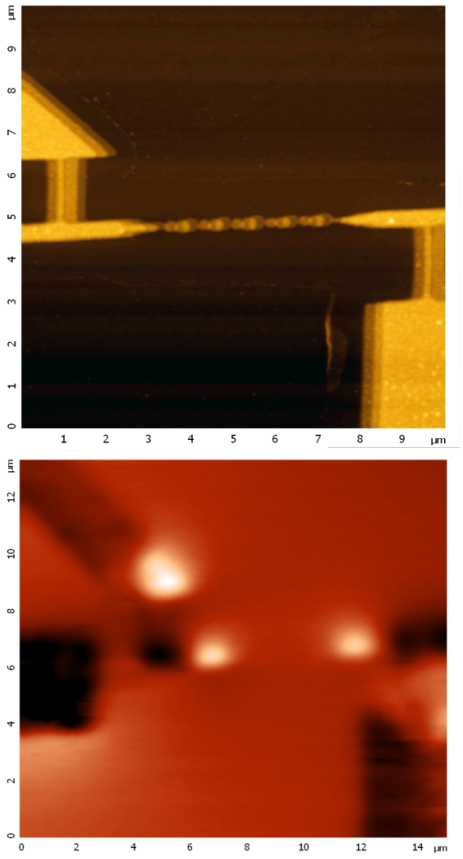

((b))

Figure 5.4: (a) shows a schematic of a sample consisting of five nickel discs 21nm thick and two evaporations of aluminium producing 80nm contact leads. It is important to note that this was produced using the traditional evaporation technique, so the excess nickel can be seen on top of the aluminium leads. (b) shows the atomic force microscopy image (above) and magnetic force microscopy image (below) of the sample. The point of this figure is to highlight the stray field magnetisation produced by the excess nickel (shown as black and white in the lower image) is significant and problematic, as the signal from these leads is strong enough to make the discs' magnetisation invisible. It is not possible to see if this stray field can have a significant effect on the discs. As the magnetisation of the disc is imperative to this project, the improvements made to the evaporation technique were critical.

5.4 Four-point measurement with nanostructures fabricated using the modified shadow evaporation technique

After developing the improved shadow evaporation technique, the sample fabricated to measure the four point measurement can be seen in figure 5.5 (b) and (c). The power of the new technique is revealed when comparing to the previous sample shown in figure 5.5 (a), with the unwanted nickel being completely removed from the area around the disc. This was an imperative process and removed all possibilities of magnetisation deformation from the stray field, and proved vital in the fabrication of all future samples.

The sample was then loaded into the cryostat and measured as explained in the experimental techniques section. An oscillator set to a low frequency and a current limiting resistor at room temperature were used to drive a current through the disc. The voltage drop across the disc was then measured by the voltage probes which were connected to a low noise voltage pre-amplifier at room temperature. The output from this amplifier was then passed to a lock-in amplifier and recorded. The $\frac{dV}{dI}$ produced can be seen in figure 5.6, with the integrated IV shown in figure 5.7. This shows a zero bias resistance of 6Ω, and no superconducting transition of the ferromagnetic disc was detected. An important feature of this experiment, is the ability to repeat measurements after changing the disc magnetisation. Using the sample seen in figure 5.5, the external magnetic field was increased to 3T and reduced back to 0T; changing the magnetisation of the disc from the vortex state to the single domain state as explained in the *background* section. Figure 5.8 shows the differential resistance of the sample exposed to high magnetic field, in comparison with figure 5.6. It is important to note the zero bias resistance remains the same as before the exposure to high field, however there is a clear change in curve shape. Moreover, the critical current in the SFS wire with the ferromagnet in the single domain state was found to be much smaller than in the vortex state. This variation is possibly due to the difference in the polarization of electrical currents

injected into the aluminium wire from discs in different magnetic states; with a lower expected polarization in the vortex state, however this effect deserves further investigation. The peaks relating to the critical current of the aluminium are clear, however a transition of the ferromagnetic disc to the superconducting state, or superconductor induced changes in the conductance cannot be seen. Assuming the critical current of the disc to be too small so that the corresponding voltage drop is less than the noise level we have measured a multi disc sample explained in the next section.

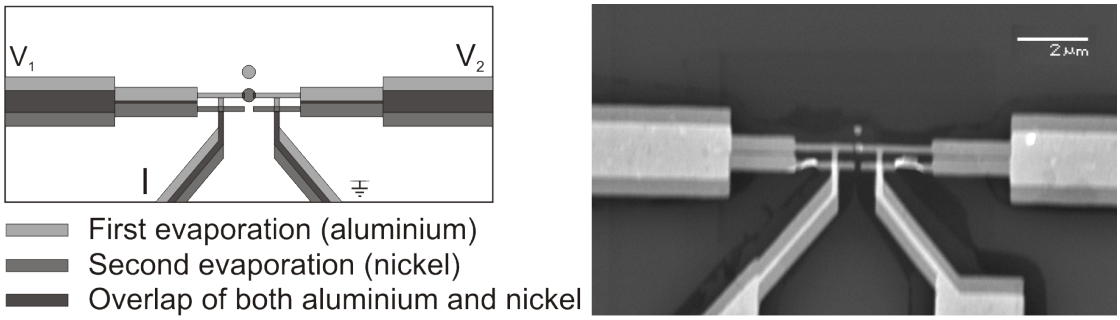

((a))

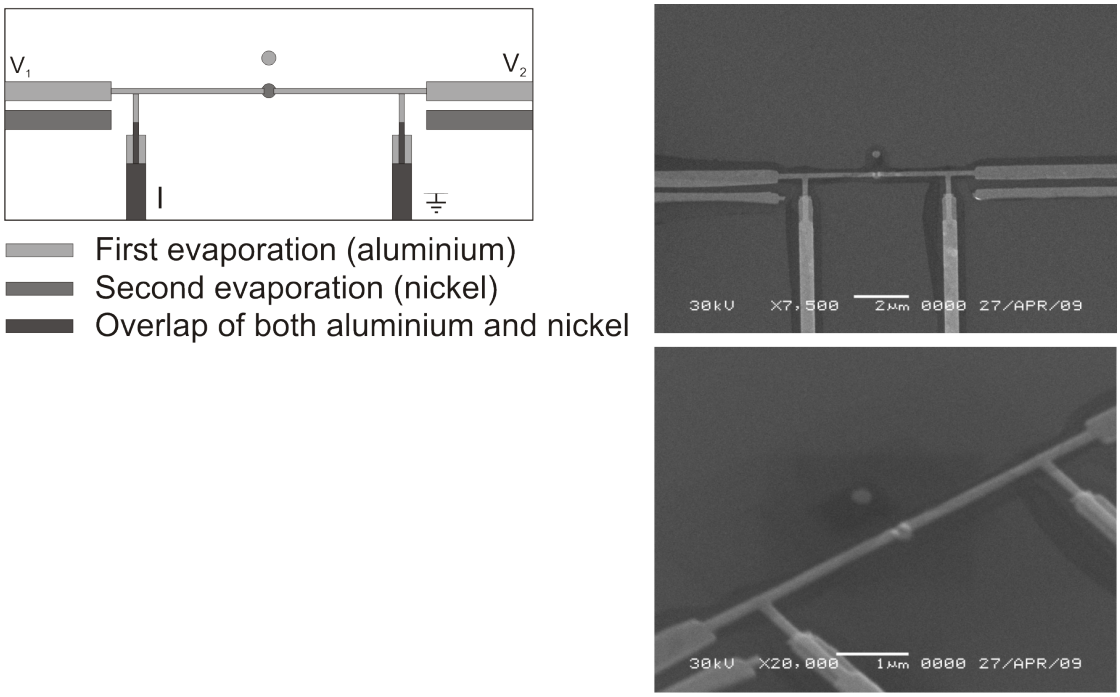

((b))

Figure 5.5: Schematics (left) and scanning electron microscopy images (right) of two samples consisting of a 21nm thick nickel disc and 100nm aluminium wires made with two different evaporation techniques. Figure (b) shows the sample fabricated with resist/germanium/resist tri-layer, benefitting from the use of the selective undercut allowing the formation of the ferromagnetic disc, but the power of the process can be seen from the lack of the excess nickel when compared with the traditional evaporation technique shown in figure (a).

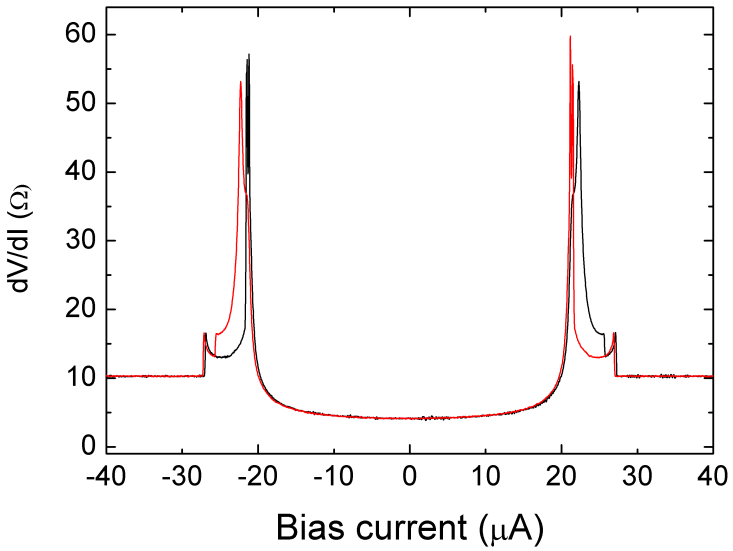

Figure 5.6: Differential resistance of the four point measurement sample measured in 5.5 (b), showing a zero bias resistance of 6 Ω. These measurements were taken at 240mK and at zero applied field, and the red and black curves represent measurements taken in each current direction.

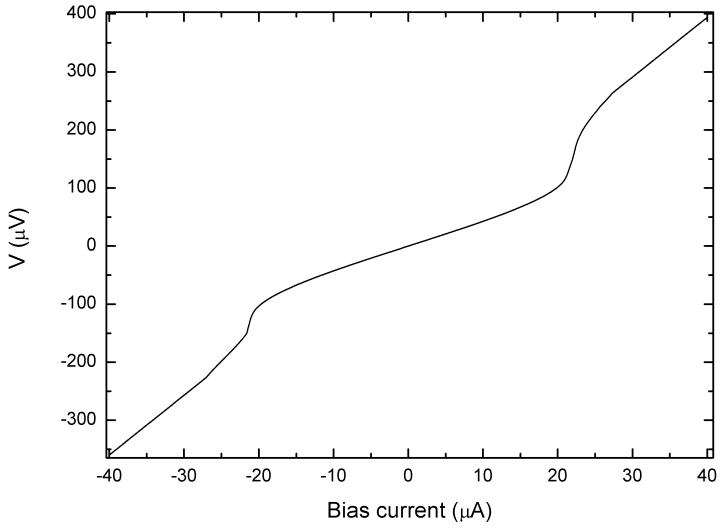

Figure 5.7: IV curve integrated from the above differential resistance curve for the four point measurement sample measured in 5.5 (b).

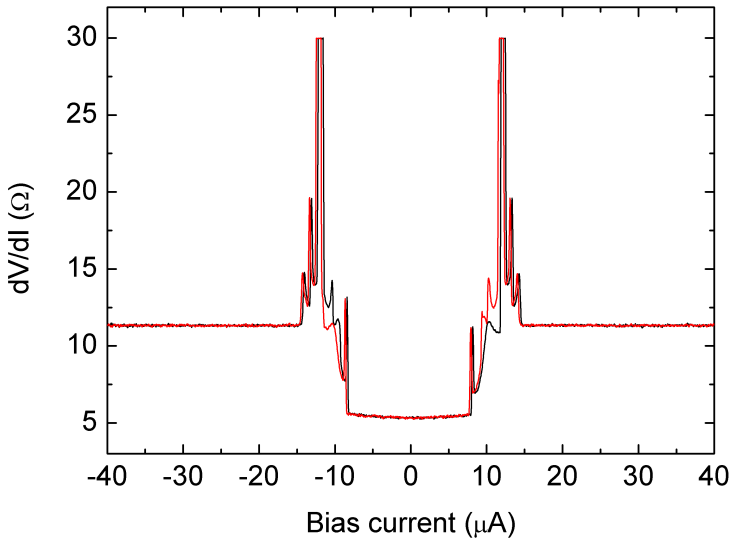

Figure 5.8: Differential resistance repeated from 5.6, after exposing the sample to an external magnetic field of 3T.

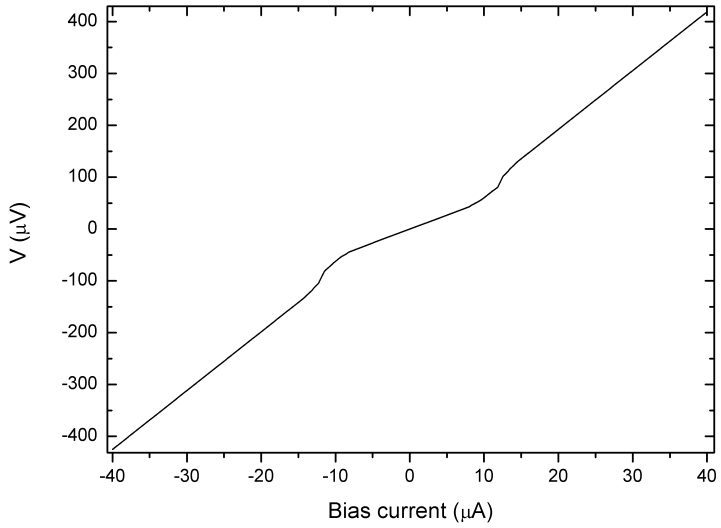

Figure 5.9: IV curve integrated from the above differential resistance curve after exposing the sample to an external magnetic field of 3T.

5.5 The multi-disc sample

The four point measurements showed no evidence of a critical current for the nickel, so the search for the critical current in the SFS junction lead to the development of a multi disc sample. As the I_c was expected to be small, leading to a small characteristic voltage, an array was designed consisting of 1064 individual discs in both series and parallel to sum to a measureable signal. An SEM micrograph of the series design can be seen in figure 5.10, and the benefits from the improved shadow evaporation technique can be clearly seen.

The differential resistance curve is presented in figure 5.11 representing the sample shown, with the red and black curves representing the results taken from each direction. The first interesting effect to note is the reproducible peaks seen between $\sim 6\mu$A and $\sim 9\ \mu$A. The second feature is the zero bias peak, which was also seen in the interference devices described below, however interestingly not seen in four point measurements. The possible contributions to this effect are discussed in the later subsection.

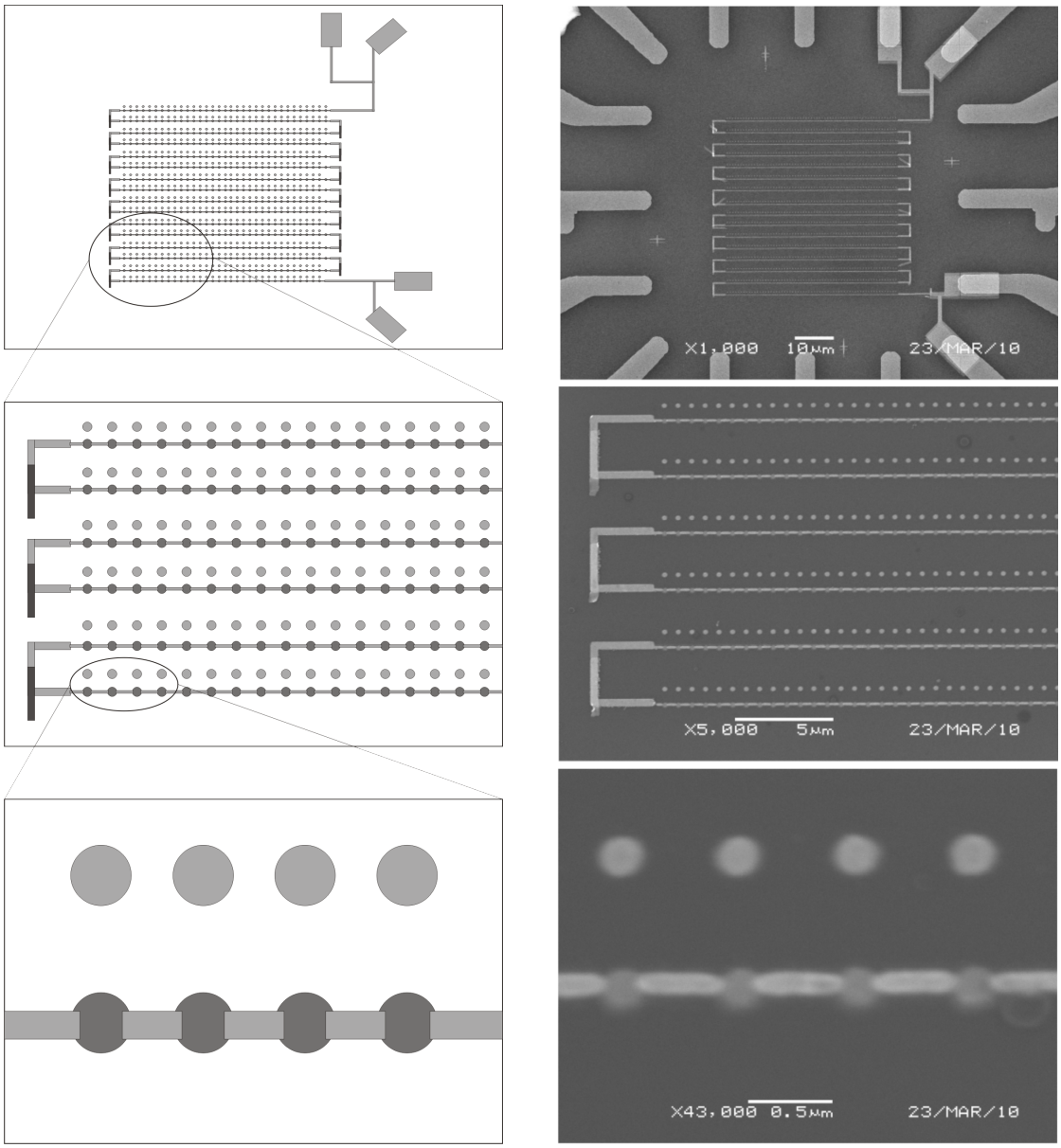

Figure 5.10: Schematic (left) and SEM image (right) of the multi-disc sample consisting of 1064 nickel discs 300nm in diameter and 21nm thick, and aluminium leads 60nm thick. It is also important to note the lack of unwanted nickel from the sample area arising from the selective undercut.

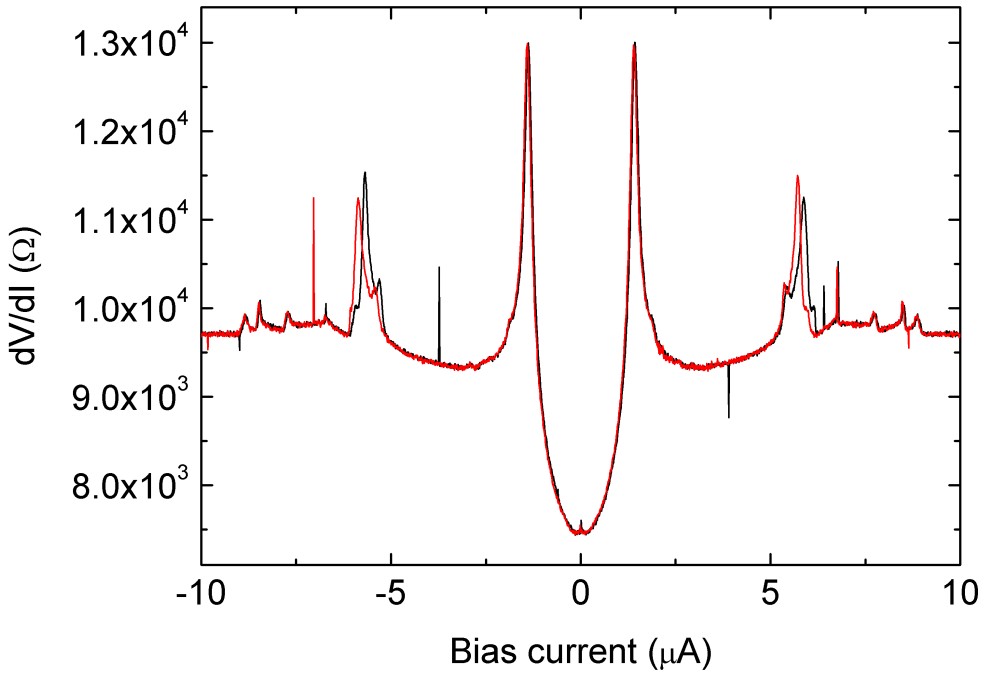

Figure 5.11: Differential resistance of the multi disc sample shown in 5.10 measured at 240mK. The red and black curves represent measurements taken in each direction. It is important to note the peak at zero bias at variant with the curve for the single disc, with the contributions to this feature discussed in the later subsection

5.6 The Hybrid Quantum Interference Device

The issues presented so far lead to the design of a flux biased interference device, developed by adapting ideas used to test the proximity effect in holmium SFS junctions using Andreev interferometry discussed in the *background* section. The device consists of a superconducting loop interrupted with a ferromagnetic disc, allowing the detection of superconducting phase-periodic conductance oscillations as a function of the magnetic flux applied perpendicular to the substrate. By designing the separation of superconducting contacts to be more than two orders of magnitude larger than ξ_F, the contribution can be attributed to the penetration of time-asymmetric triplet pairs.

5.6.1 SEM images

This subsection will discuss four particularly interesting samples labelled A-D, all with the same design and each distinguished by their particular $\frac{dV}{dI}$ curves. The samples show essentially different transport properties that we believe is due to the difference in the magnetic structure in proximity to the F/S interfaces and the varying resistance of the each interface. All of the devices were fabricated using the improved shadow evaporation technique with an asymmetric undercut resulting in the unwanted nickel being evaporated onto the wall of the resist and removed at lift off, minimising the effect of the stray field on the disc. These SEM images show clearly the power of the improved evaporation technique, with the area directly under the superconducting wires being completely absent of nickel. The important dimensions are all summarised in the table at the end of this subsection. All of the SEM images consist of a ferromagnetic section made of a 4N nickel disc, all of which are 21nm thick, and either 300nm or 400nm in diameter.

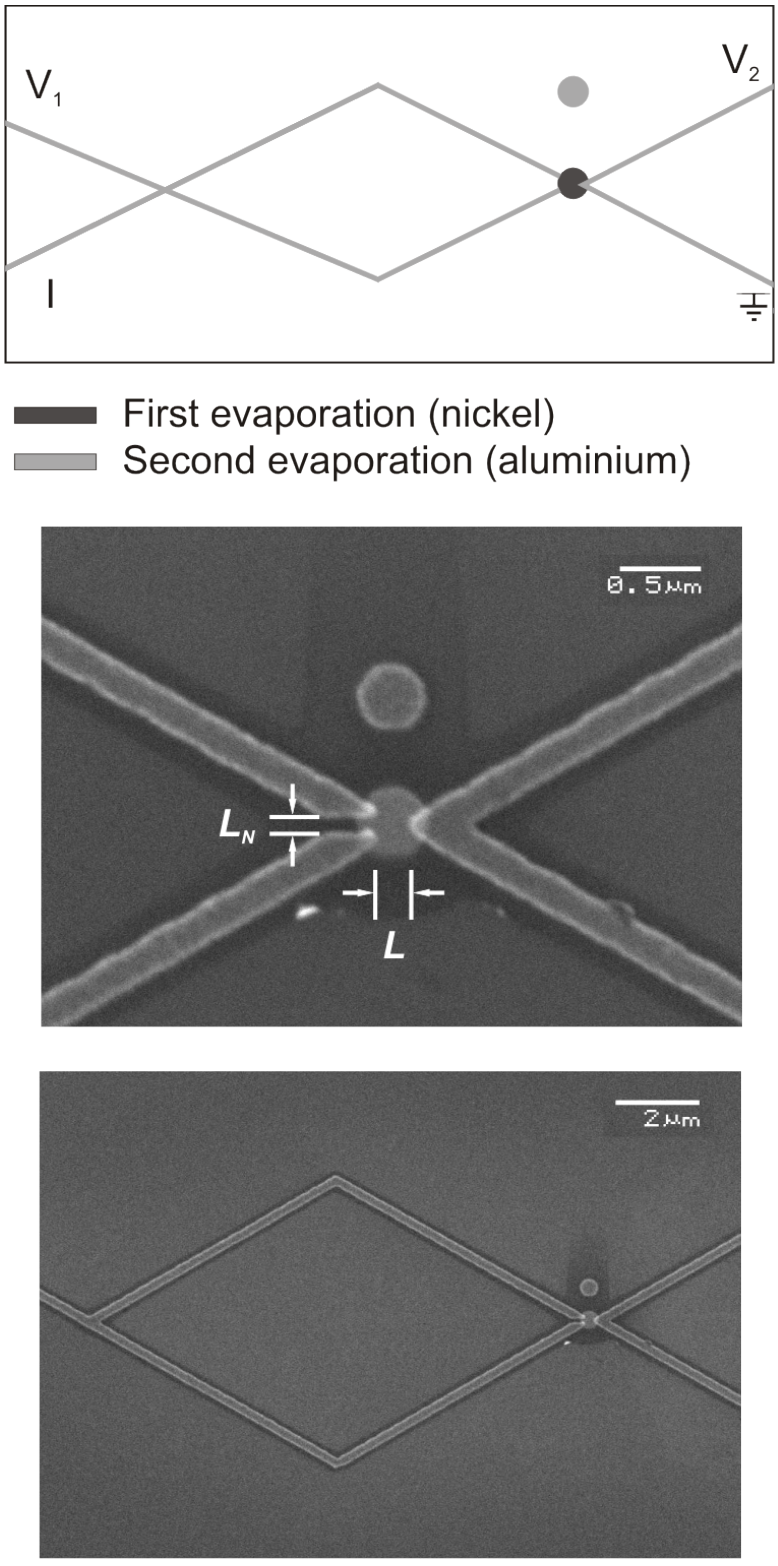

Figure 5.12: SEM images of the type A hybrid quantum interference device consisting of a nickel disc 440nm in diameter and 21nm thick, with aluminium leads 100nm thick. The power of the improved evaporation technique shows the complete absence of nickel with the exception of the single disc. It is important to note the dimensions labeled with $L_N = 98$nm and $L = 214$nm, both of which are orders of magnitude larger than the ferromagnetic coherence length.

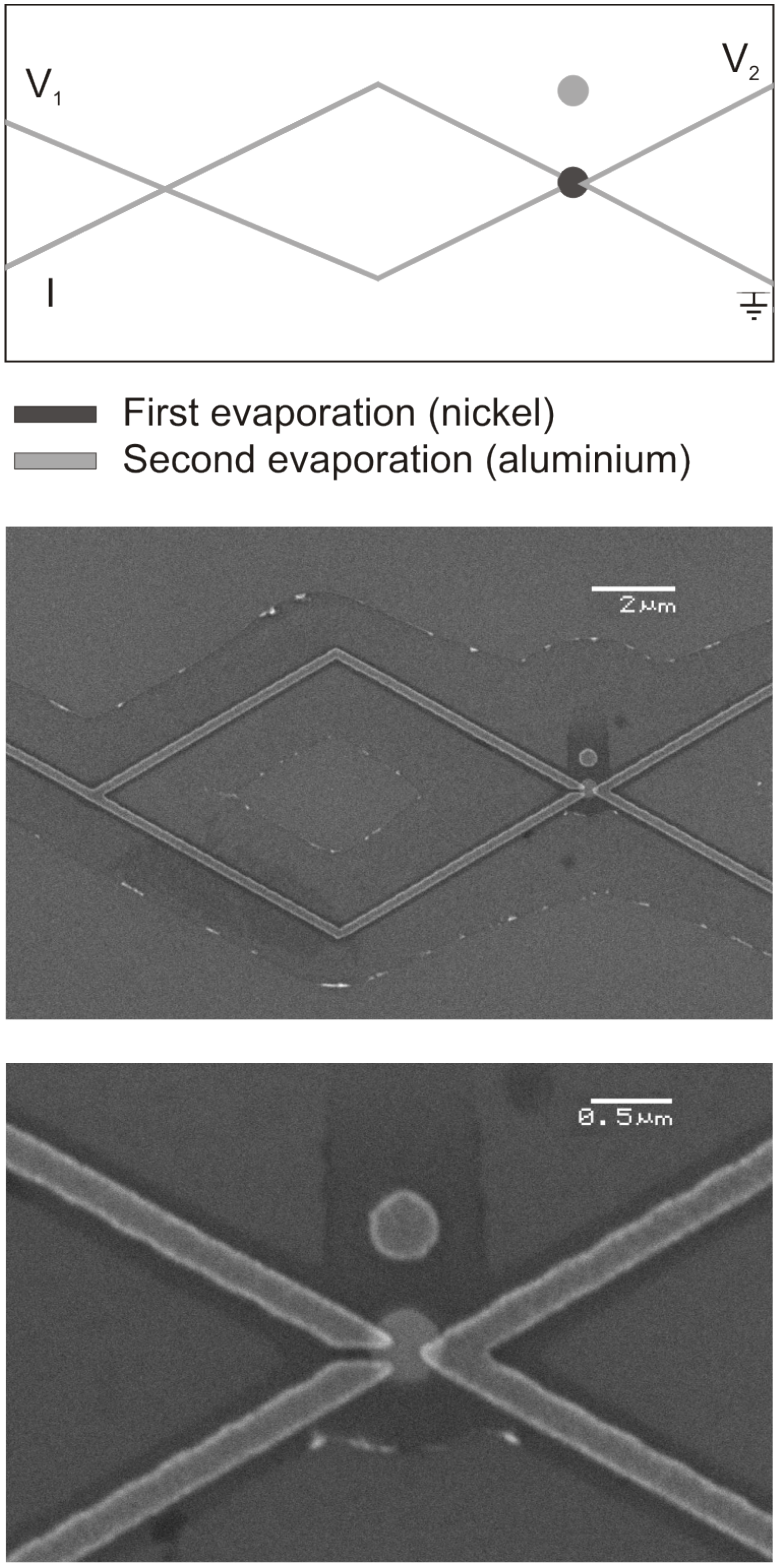

Figure 5.13: Schematic (above) and SEM images (below) of the type B interference device consisting of a nickel disc 440nm in diameter and 21nm thick. The aluminium leads are 100nm thick, and the dimensions labeled in (b) are $L_N =$ 88nm and $L = 176$nm.

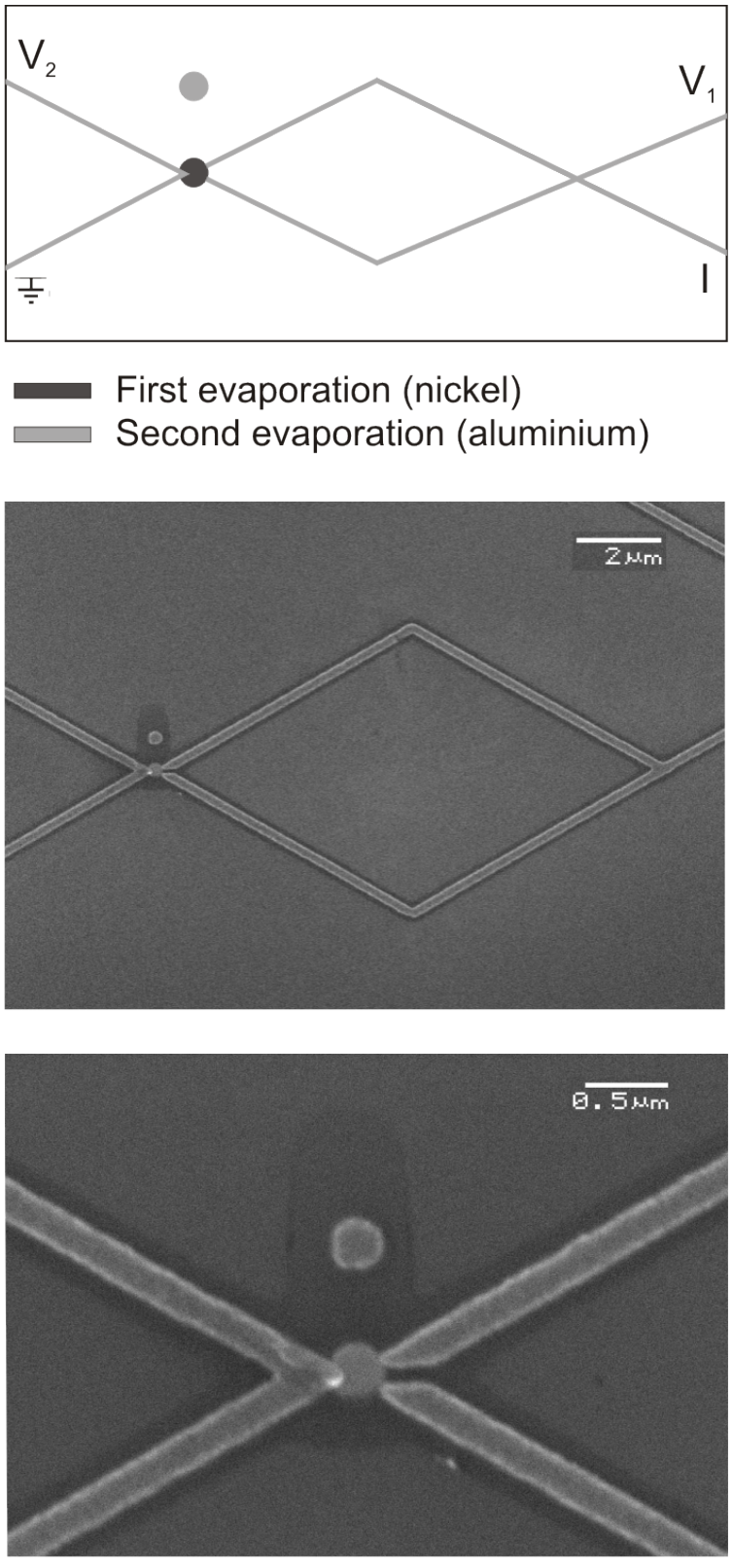

Figure 5.14: Schematic (above) and SEM images (below) of the type C interference device consisting of a nickel disc 330nm in diameter and 21nm thick. The aluminium leads are 100nm thick, and the dimensions labeled in (b) are L_N = 110nm and L = 225nm.

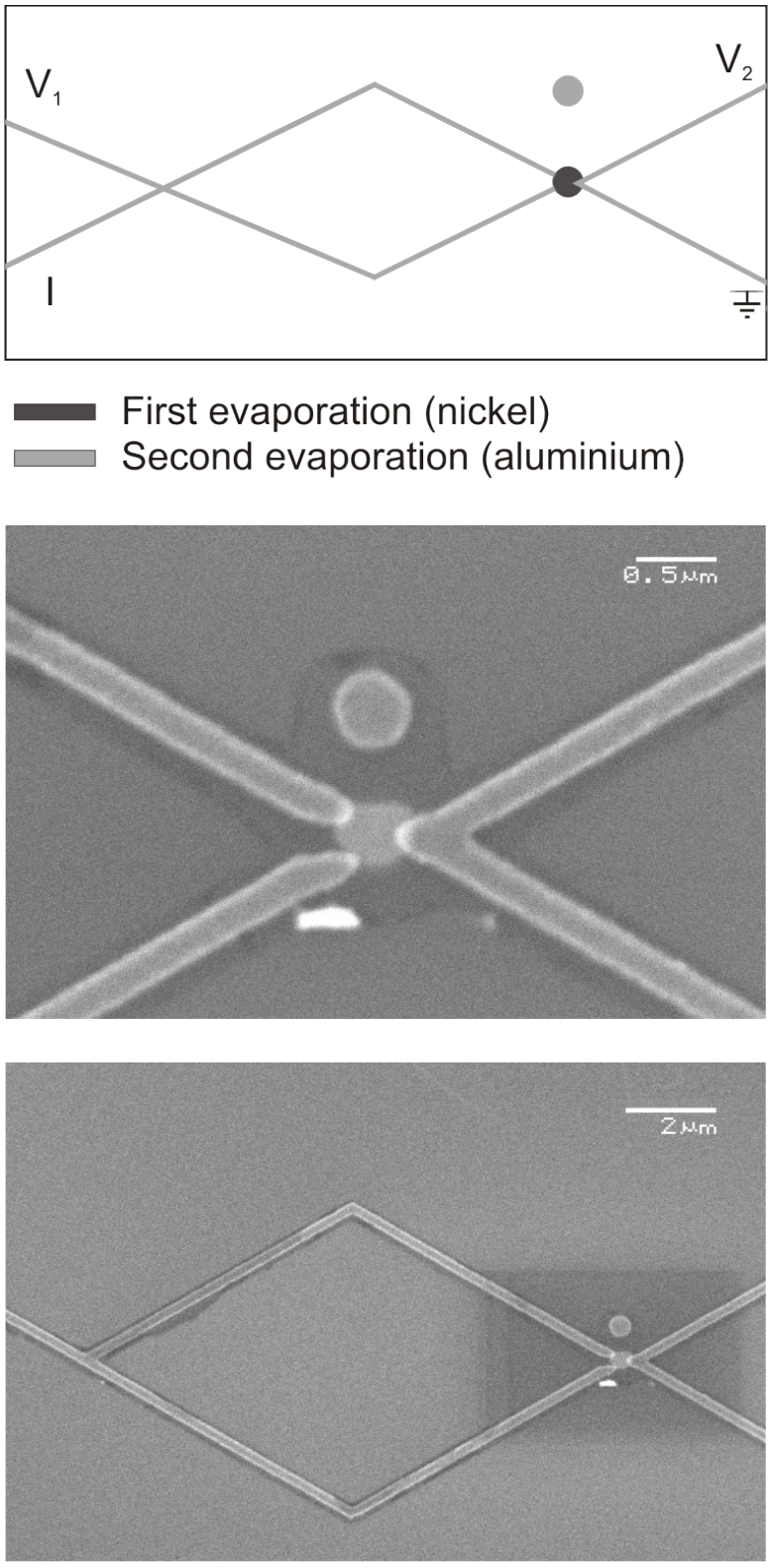

Figure 5.15: Schematic (above) and SEM images (below) of the type D hybrid quantum interference device consisting of a nickel disc 470nm in diameter and 21nm thick. The aluminium leads are 100nm thick, and the dimensions labeled in (b) are $L_N = 165$nm and $L = 250$nm.

5.6.2 Evidence of long range proximity effect: Phase periodic conductance oscillations

Unambiguous evidence for the long range proximity effect can be provided by observing superconducting phase-periodic conductance oscillations as a function of the applied magnetic field. The superconducting leads of the HyQUID are made of aluminium 100nm thick, forming a superconducting loop with an area of $40\mu m^2$. By using $\Phi_0 = \frac{h}{2e} = 2 \times 10^{-15}$Wb and $\Phi = \mathbf{B}A$, where $\mathbf{B}$ is the applied magnetic field and A is the area of the loop, the interferometer can be shown to have a period of $50\mu T$. It is important to note the magnetic field required for one oscillation is orders of magnitude smaller than the magnetic field required to change the magnetisation of the disc.

The oscillatory dependence was measured for the type D device at zero bias and by fixing the bias to 4.2μA and sweeping the magnetic field from -156.5 to 156.5 μT shown in figure 5.16 and 5.17, and the oscillations for the type C device can also be seen in figure 5.22. These curves represent a periodic line shape with a period of 50μT; matching the period expected from calculations using the area of the loop as 40 μm^2. This periodicity is also confirmed with analysis of the Fourier spectrum shown if figure 5.19 for the type D device, and in figure 5.23 for the type C device. The differential resistance for the type D sample was also repeated at varying magnetic fields from -235 to 235μT as shown in figure 5.20 and the magnetoresistance oscillations can be clearly seen by changing the range from 3.5 to 5μA as shown in figure 5.21. These oscillations provide a signature of superconducting phase coherent electron transport through the discs resulting from an overlap of condensate wave functions induced in the ferromagnetic disc by the superconductors within the range that is more than two orders of magnitude larger than the ferromagnetic singlet coherence length, ξ_F.

The amplitude of oscillations is approximately 1% and the line shape is close to sinusoidal. The oscillations are seen in the bias current range up to 0.13μA. The oscillations show unusual behaviour as a function of the bias: they disappear upon an increase in the bias and then reappear at the bias 3.9 μA corresponding to the

small feature seen in figure 5.37 at approximately 0.25 of the critical current of aluminium and exists in the bias range 3.90-4.45 μA shown in figures 5.20 and 5.21. Figure 5.18 shows the phase difference for both magnetoresistance oscillations, with the lower resistance oscillations shifted by 29.5Ω for clarity.

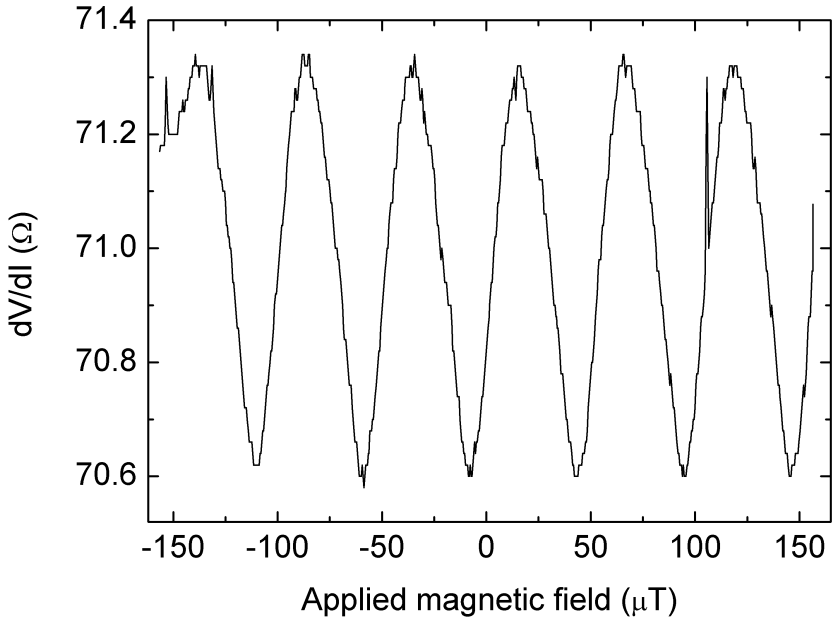

Figure 5.16: Magnetoresistance oscillations of the type D device, measured at 240mK with a fixed bias current of 4.2 μA. This device clearly shows the expected period of 50 μT.

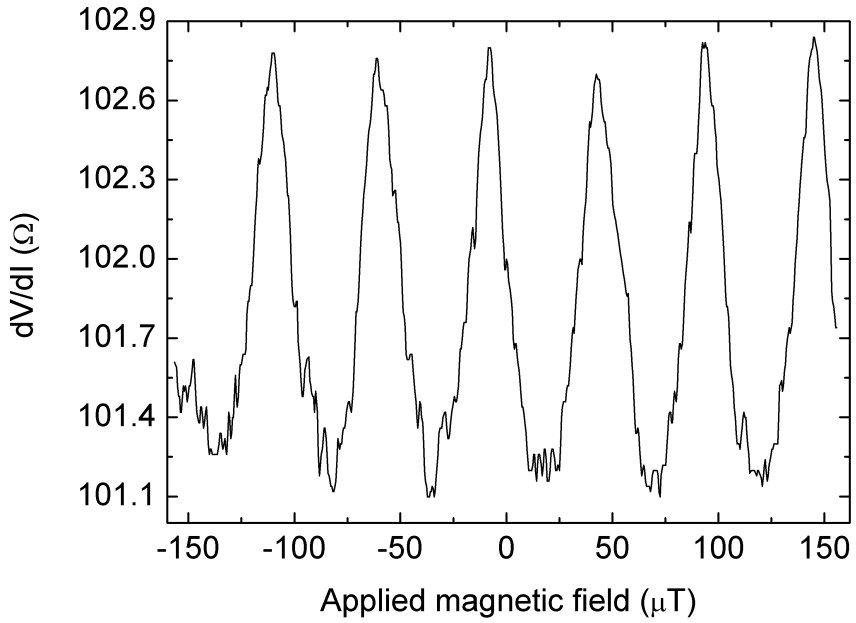

Figure 5.17: Magnetoresistance oscillations of the type D device taken at zero bias, also showing the periodic nature of the oscillations.

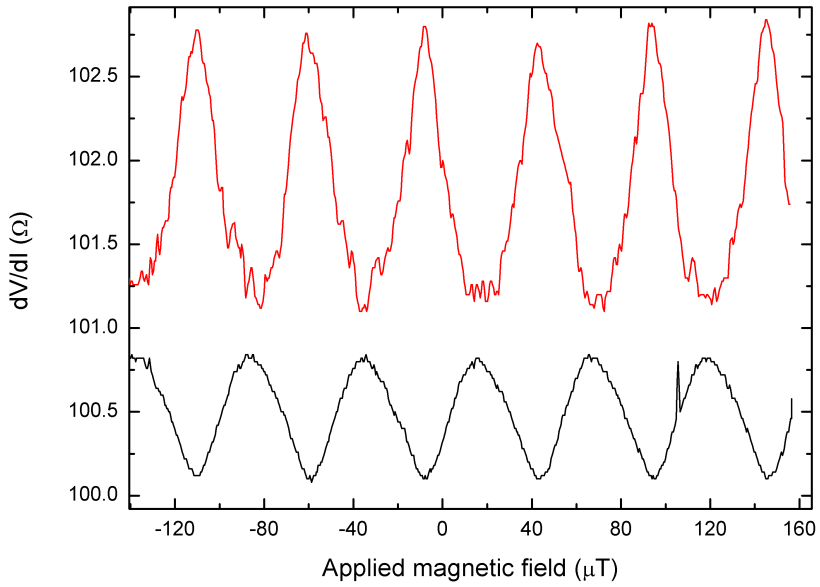

Figure 5.18: Highlighting the phase difference for the magnetoresistance measurements from figure 5.16 (black) and figure 5.17 (red). The lower resistance oscillations have been shifted 29.5Ω for clarity.

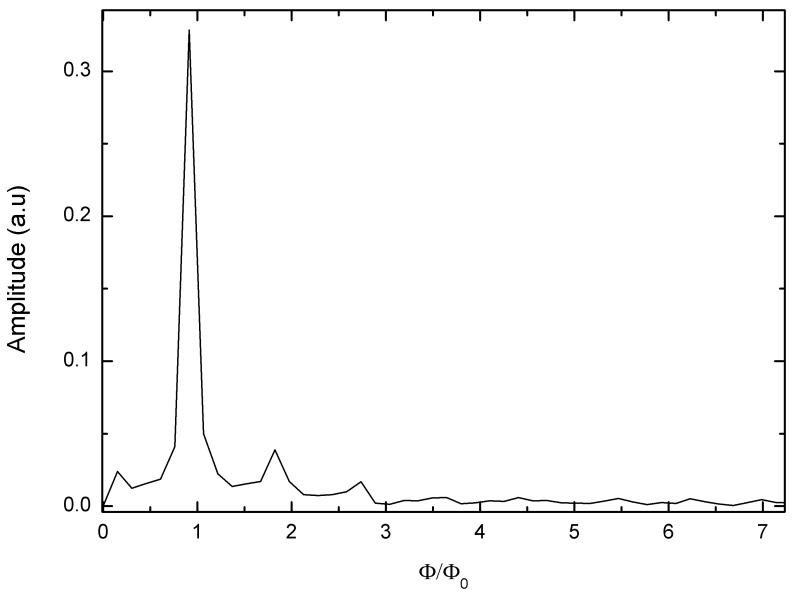

Figure 5.19: Fourier spectrum of the oscillations shown in figure 5.16 confirming the $\frac{h}{2e}$ periodicity

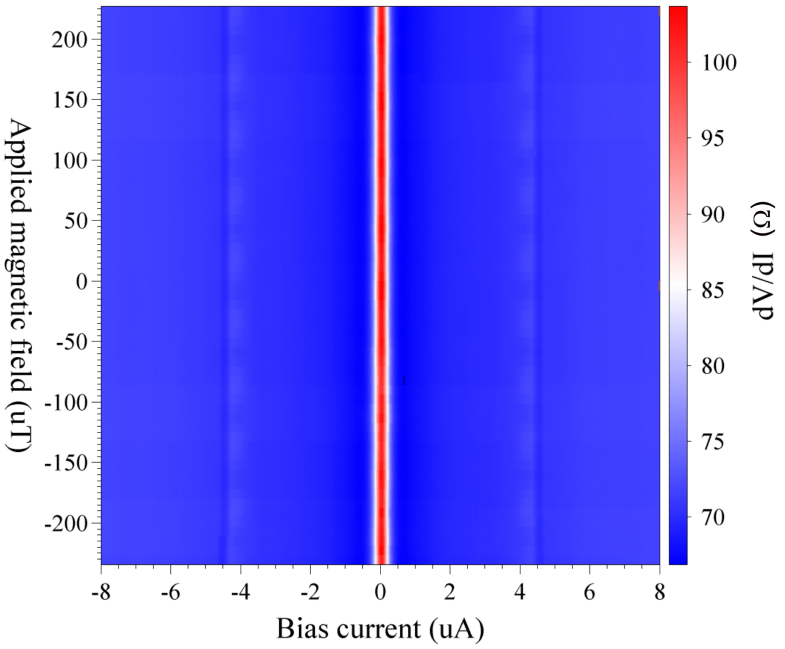

Figure 5.20: The differential resistance of the type D device was repeated at increments of magnetic field, from -235 to 235 μT. The oscillatory nature is made clearer in figure 5.21.

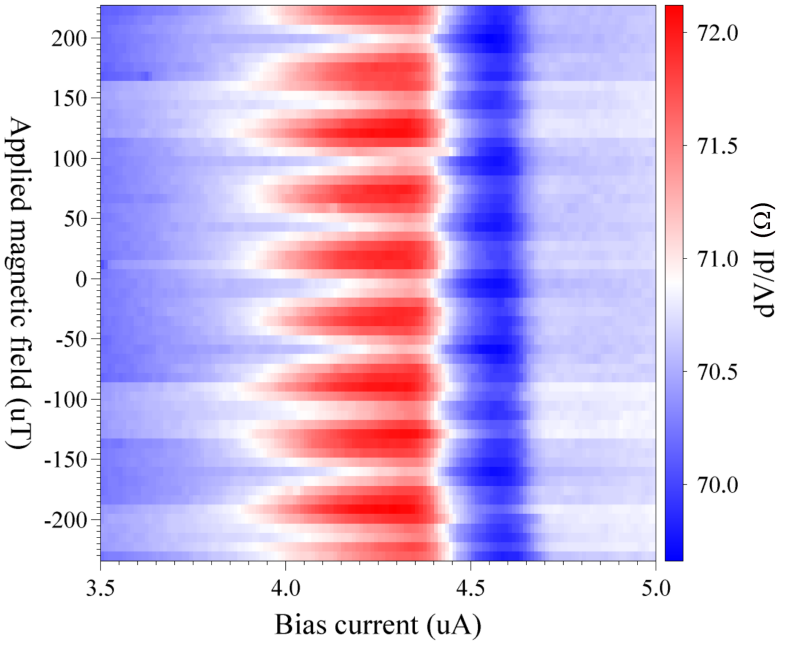

Figure 5.21: Magnetoresistance oscillations can be clearly seen from the differential resistance taken from 3.5 to 5 μA, repeated at magnetic field increments from -235 to 235 μT.

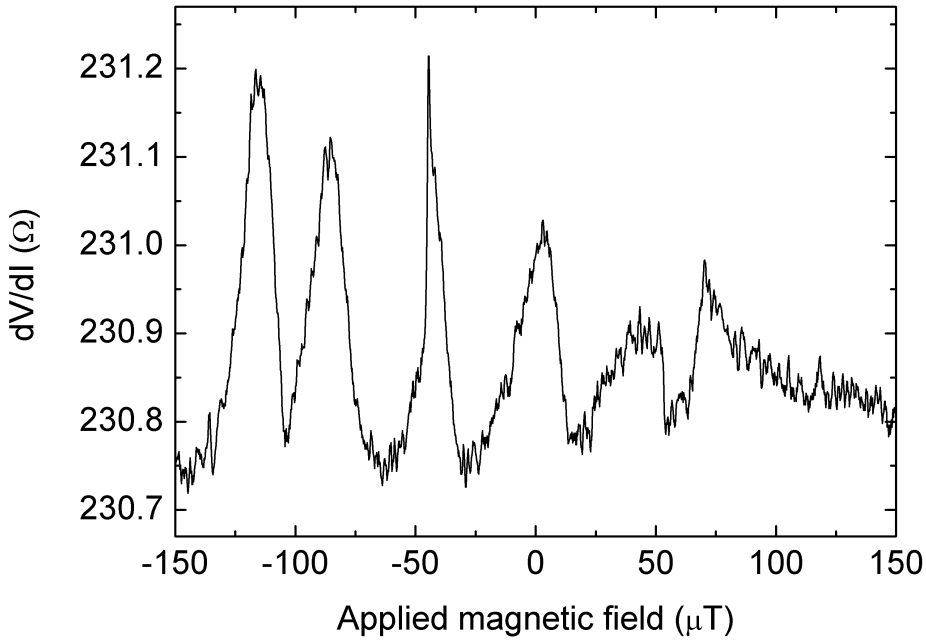

Figure 5.22: Magnetoresistance oscillations of the type C device, measured from -156 to 156 μT at 240mK. The magnetic field required for one oscillation is 50 μT.

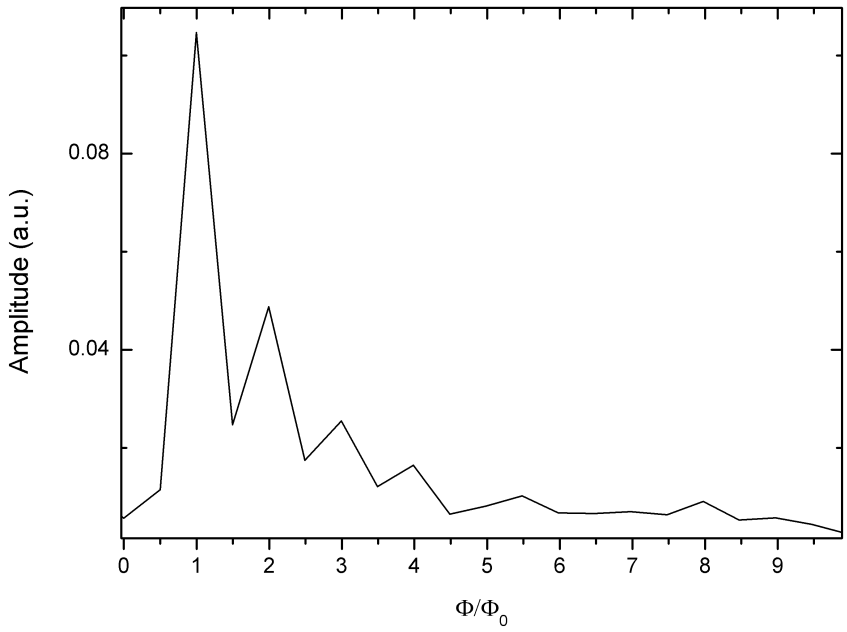

Figure 5.23: Fourier spectrum of the oscillations shown in figure 5.22 confirming the $\frac{h}{2e}$ periodicity

5.6.3 Applying high magnetic field to destroy oscillations: evidence for the dependence of the long range proximity effect on magnetic structure

The conductance oscillations above show conclusive evidence for the long range proximity effect, however one of the most important features of this experiment which distinguishes it from previous work, is to exploit the advantage of the geometrically confined magnetic structure by manipulating the magnetisation with the application of a magnetic field. This provides more information than previous experiments, as it can provide excellent evidence for the inhomogeneity of the magnetisation being the necessary generator of the triplet superconductivity. As discussed in *magnetic structure* in the *background* section, the magnetisation of the nickel disc can be forced into the hedgehog state by applying a strong magnetic field perpendicular to the sample. This allows the structure to be switched to a single domain state when the magnetic field is reduced to zero, destroying the inhomogeneous magnetisation. The magnetic field of $3T$ was applied perpendicular to the substrate, reduced to $0T$ and the measurements were repeated. The most interesting graphs to compare are figure 5.25 with 5.27 and figure 5.29 with **??** showing the $\frac{dV}{dI}$ measurements taken at increments of magnetic field from -235 to 235 μT. The results clearly show the oscillating nature of the peaks have disappeared, and as all variables were kept constant for both sets of data it is clear the effect has resulted from a change of the magnetic structure of the disc. It is important to note that for the *type C* device, the value of the differential resistance and its line shape (figure 5.36) were close to the low resistance interferometers as seen in *type A*, revealing a significant dependence on the discs' magnetic structure. It is also critical to note the vast differences between figures 5.29 and 5.31, concluding that the transition from vortex state to single domain state leads to the independence of the differential resistance on magnetic field, and the complete absence of the oscillatory behaviour.

Figure 5.32 shows as MFM image of the HyQUID taken after being measured in the cryostat and therefore after being exposed to the high field. This image shows

the disc in the single domain state, coinciding with the simulation of the magnetic structure with an applied magnetic field is discussed in the *background* section. The key conclusion from this is the possibility of having two different states available at zero applied field; the vortex state and the single domained state. The change of $\frac{dV}{dI}$ at varying magnetic fields is a vital result when testing the validity of the suggested theories and can provide an excellent progressive step in the field of the long range proximity effect that could not be provided by holmium for example.

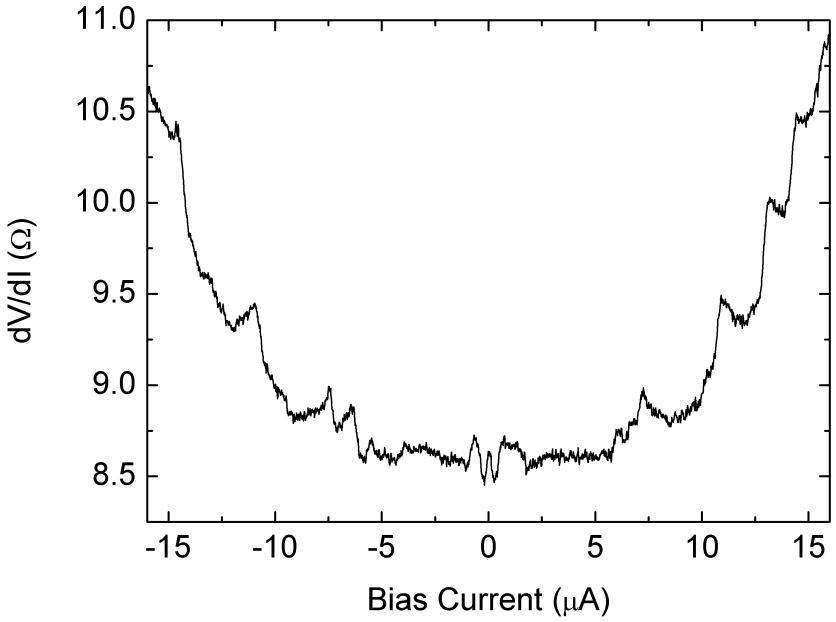

Figure 5.24: Differential resistance of the type B HyQUID measured at 240mK, taken from -16μA to 16μA.

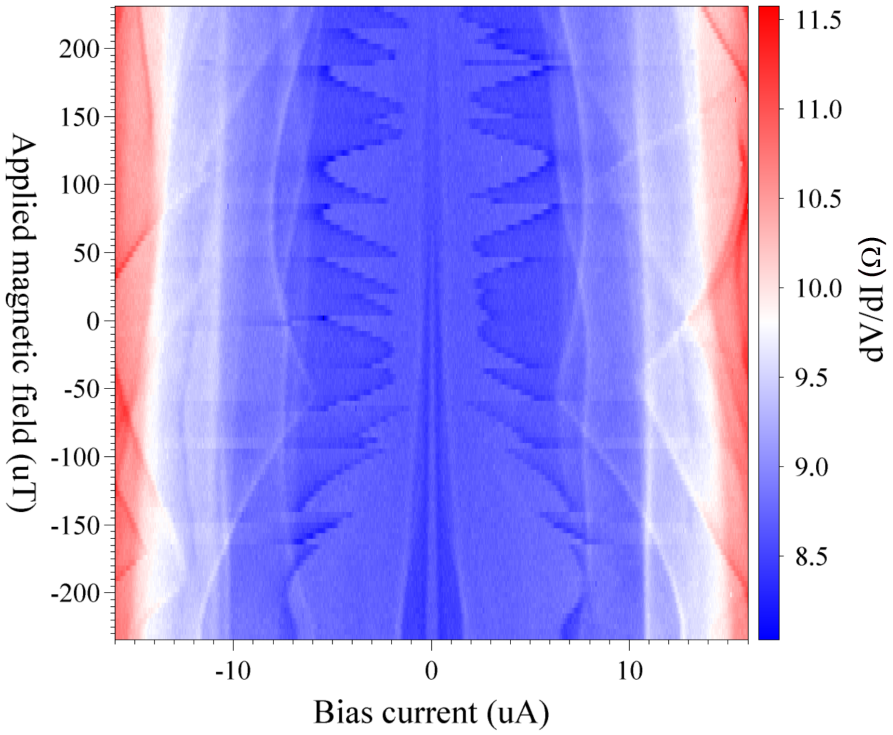

Figure 5.25: Image of 120 differential resistance curves taken in the same range as in 5.24, taken at equal increments of magnetic field from -234.75 to 234.75 μT.

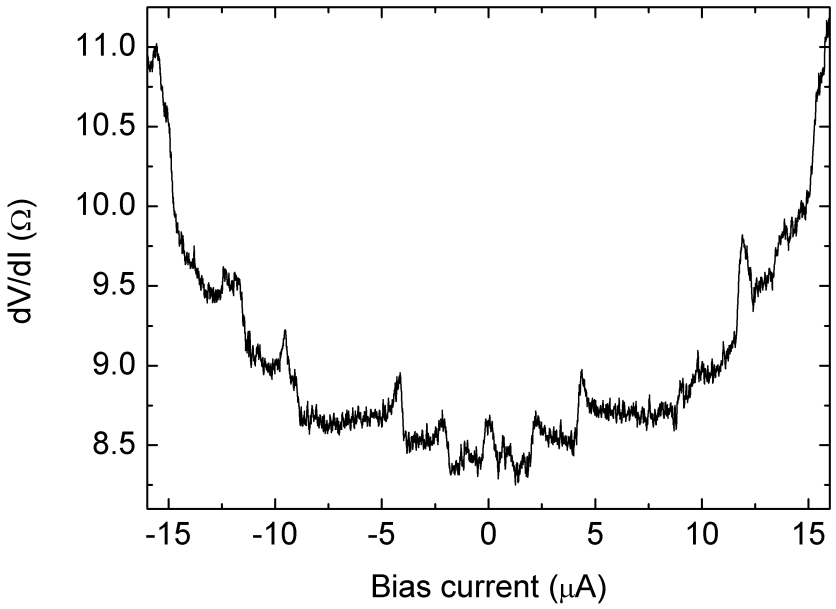

Figure 5.26: Differential resistance curve of the type B device measured at 240mK, taken using the same parameters as figure 5.24 after increasing the magnetic field to 3T and decreased back to 0T.

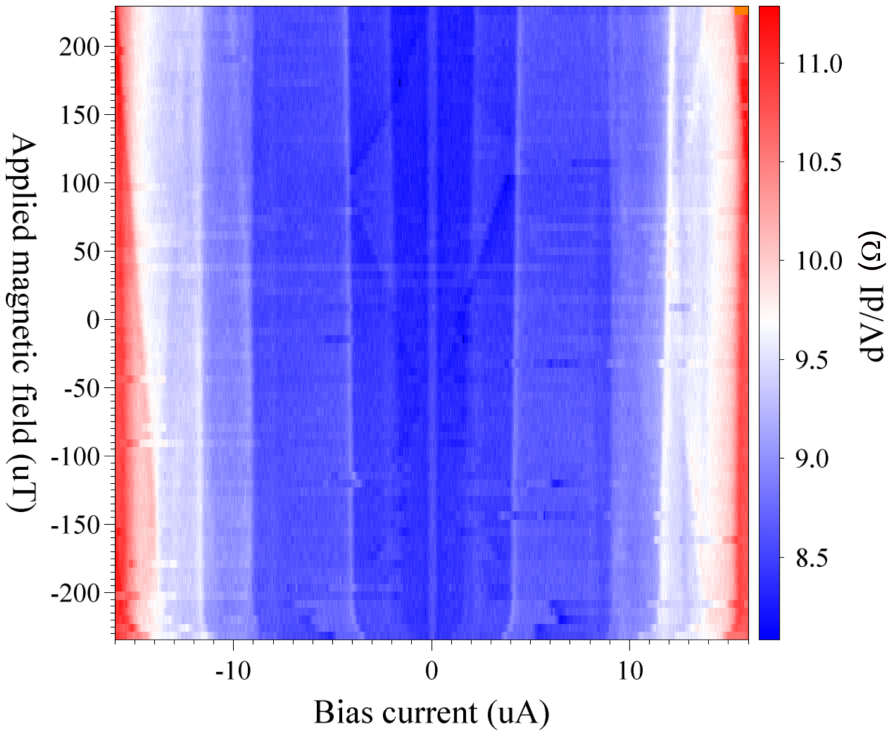

Figure 5.27: Repeated measurement taken from figure 5.25 after exposure to high field.

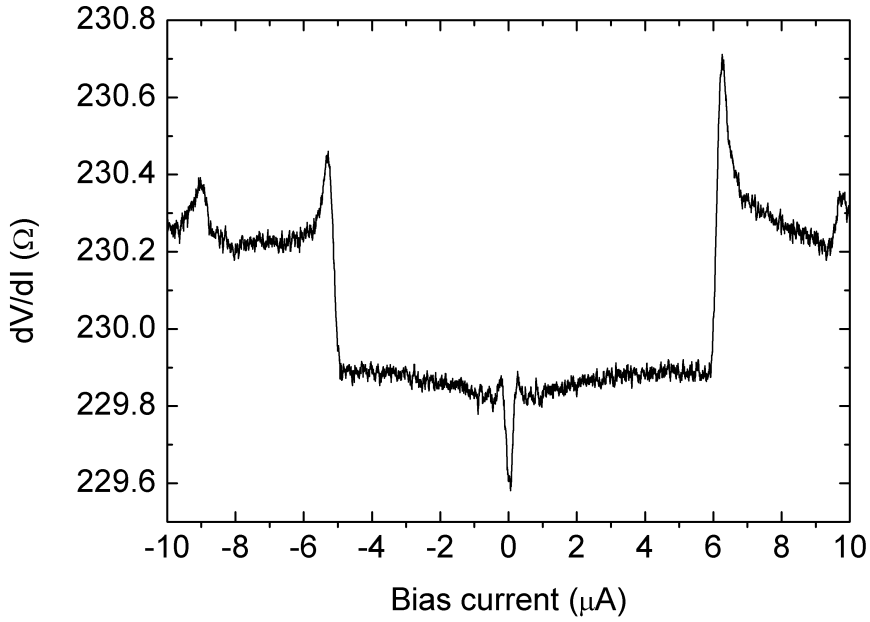

Figure 5.28: Differential resistance of the type C HyQUID measured at 240mK, taken from -10 to 10 μA, highlighting the minima at zero bias.

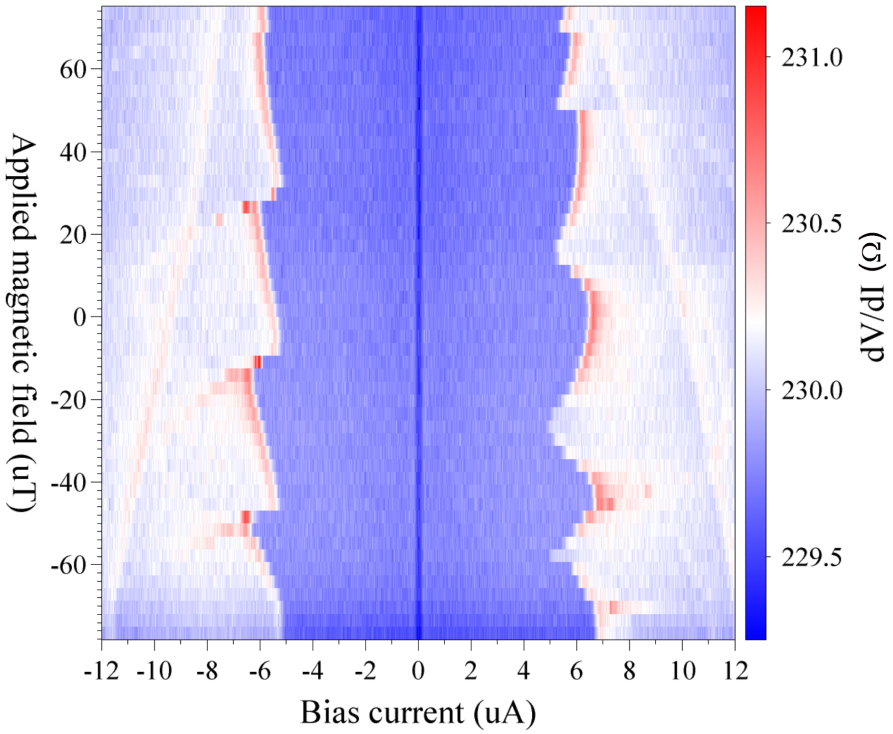

Figure 5.29: This 3D image represents figure 5.28 repeated at increments of magnetic field from -78 to 78 μT, showing the periodic nature of the oscillations.

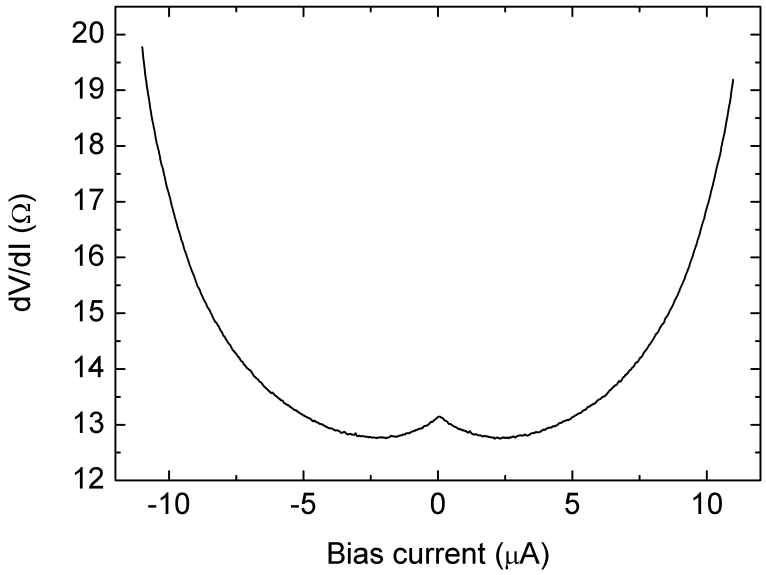

Figure 5.30: Repeated differential resistance of the type C device taken after exposing the sample to a high magnetic field. The remarkable effect of the high field can be seen by comparing the sample to figure 5.28.

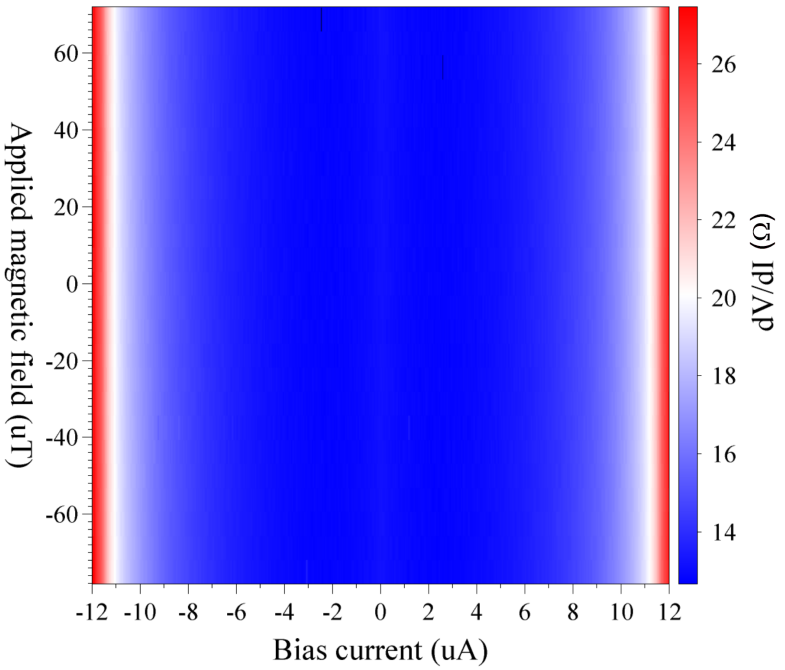

Figure 5.31: It is important to note the elimination of the oscillations after the sample was exposed to high field, and the measurement from figure 5.29 was repeated.

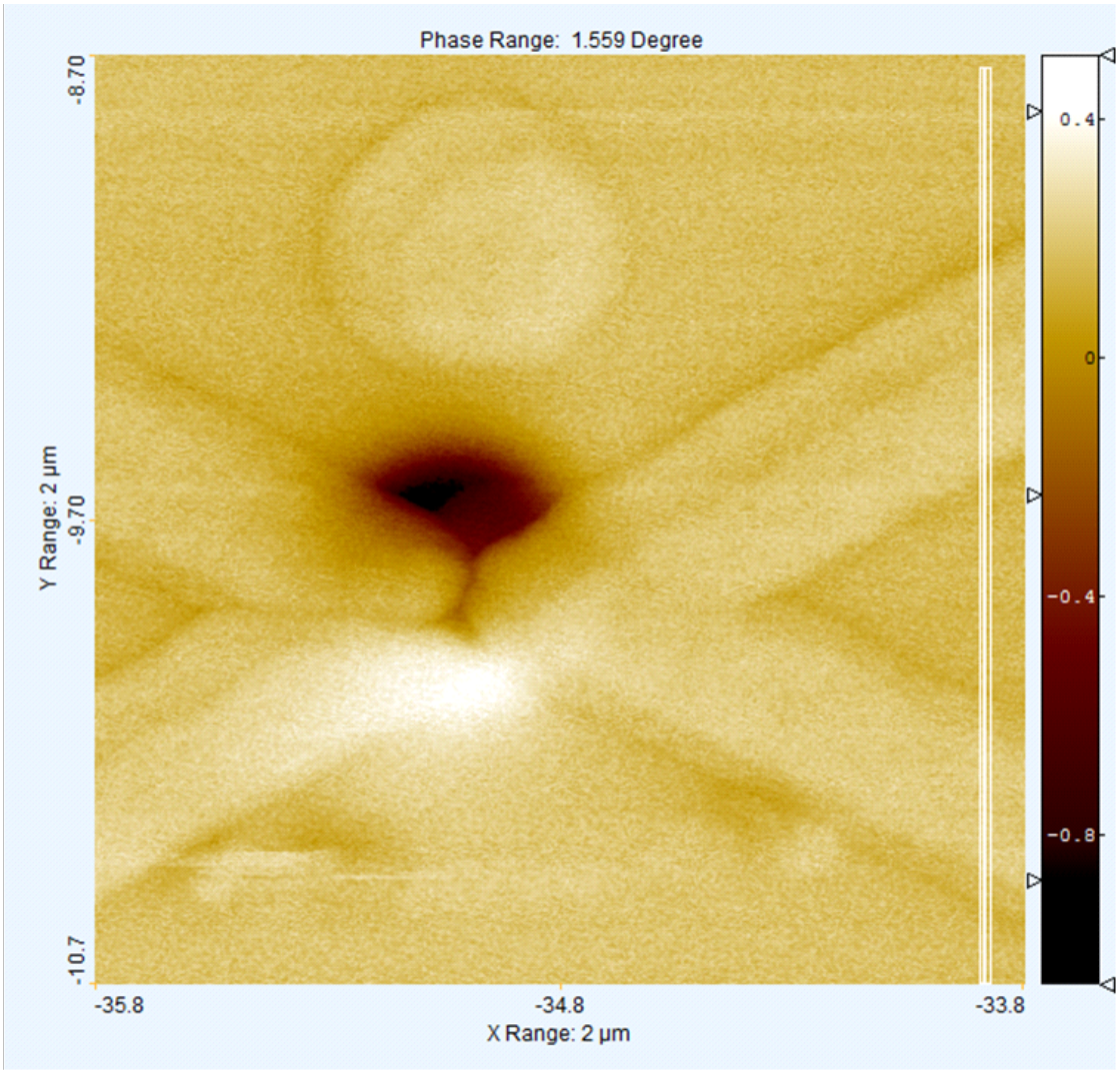

Figure 5.32: MFM image showing the local magnetisation of the type B HyQUID measured at room temperature with zero applied field, after the sample has been exposed to an external magnetic field of 3T. The nickel disc is 440nm in diameter and 21nm thick, and the black and white section shows a typical signal of a single domain state, with the magnetisation parallel to the surface of the substrate, pointing in the vertical direction. The scale bar on the right is the change of the cantilever phase. Note the disc seen at the top of the image is a product of the shadow evaporation technique and is made of aluminium so does not have the same signal as the nickel disc.

5.6.4 Analysis of the results obtained using the HyQUID

A useful comparison of the important information taken from each interference device including all necessary dimensions can be seen in table 5.1 below. The resistivity ρ of our nickel was about 18 $\mu\Omega$ cm, and using the value for $\rho l = 1.5 \times 10^{-11} \Omega cm^2$ for nickel (where l is the mean free path) calculates the mean free path to be $l = 8$nm with corresponding diffusion coefficient $D = \frac{v_F l}{3} \approx 25 cm^{-1}$ where v_F is the Fermi velocity. The ferromagnetic coherence length can then be calculated to be $\xi_F = 2nm$ that is two orders of magnitude less than the distance between the F/S contacts. However using the model suggested by Kalenkov et al [21], the coherence length in the disc can be calculated by considering the ferromagnetic disc as a normal metal, therefore exchanging the Curie temperature to the temperature of the sample, $T = 240mK$. Using $\xi_T = \sqrt{\frac{\hbar D}{k_B T}}$ gives the thermal coherence length of up to 110nm, which is now a feasible distance to detect experimentally.

A huge benefit with this HyQUID design is that the quantum conductance oscillations resulting from the long range proximity effect can be seen if the ferromagnet is less than the phase breaking length, $L_\phi = \sqrt{D\tau_\phi}$ (where τ_ϕ^{-1} is the phase breaking rate) even if it is longer than the thermal coherence length, and the critical current negligible. This situation is well known in Andreev interferometers with a non magnetic normal part [71] where it is a result of the difference in the characteristic length scales corresponding to kinetic properties such as conductance and thermodynamic characteristics such as critical current and temperature [72]. The conductance is contributed by quasiparticles within the energy range of about the Thouless energy $\delta\epsilon \approx \epsilon_{th} = \frac{\hbar D}{L_N^2}$, L_N is the distance between the superconducting contacts, while the Josephson current is contributed by the quasiparticles within $\delta\epsilon \approx k_B T$. As a result the conductance is phase coherent in SNS junctions with a distance between the N/S interfaces up to the phase breaking length L_ϕ while the Josephson current survives up to the coherence length ξ_T. Usually, at high enough temperatures the phase breaking length is larger than the coherence length and oscillations in the resistance survive up to much higher temperatures that the Josephson current [71].

HyQUID type	Disc diameter (nm)	L (nm)	L_N (nm)	$\frac{L_N}{L}$	Zero bias resistance (Ω)	Periodic oscillations
A	440	214	98	0.46	14.4	No
B	440	176	88	0.50	8.6	No
C	330	225	110	0.49	229.5	Yes
D	470	250	165	0.66	100.7	Yes

Table 5.1: Table comparing important values for the four HyQUID samples

It is important to note the variables that have contributed to the variety of observed effects have been considered in the *Analysis of results* section below. However, it is necessary to consider the differences in the differential resistance curves to observe these variations more clearly. The differential resistance $\frac{dV}{dI}$ of the interferometer is a sum of contributions from the three Ni/Al interfaces, $(\frac{dV}{dI})_B$, and the bulk of the disc, $(\frac{dV}{dI})_F$ giving $\frac{dV}{dI} \approx (\frac{dV}{dI})_F + \frac{3}{2}(\frac{dV}{dI})_B$.

The differential resistance curve for the type A HyQUID in its as-grown virgin magnetic state can be seen in figure 5.33. This is similar to the curve produced by the single SFS four point measurement and shows a zero bias resistance of 14 Ω, and the aluminium is forced into the normal state at the bias current peaks at -11μA and 11μA giving a normal resistance of 36 Ω. The particularly interesting feature of this curve is the peak at zero bias which is highlighted in figure 5.34, the contributions of which are discussed the later subsection. For an aluminium wire, the product of the critical current and the normal resistance are proportional to the superconducting energy gap; $I_cR_N \propto \Delta$. The value for I_cR_N for this sample is measured to be approximately 400μV, which coincides with the values of I_cR_N which has been measured experimentally for aluminium nanobridges to be between 200-600μV [73]. The structure of this curve including the zero bias peak shown in figure 5.34 was independent of magnetic field showing no observations of conductance oscillations and therefore showing no evidence of the long range proximity effect.

Figure 5.35 and figure 5.24 shows the $\frac{dV}{dI}$ for the type B HyQUID taken using an excitation current of 100nA, and varying the bias current between -70 to 70μA and -16 and 16μA, revealing the zero bias resistance of 8.6 Ω. Using the normal resistance of 20Ω the value of I_cR_N can be calculated to be approximately 400μV,

which shows the aluminium gap to be within the expected range. The interesting features become clear when comparing the graph to the above subsection; the first being between -1.07 and 1.76 μA. The zero bias feature on the *type A* device shows a single maximum at zero bias, however there are three maximas in the same region on the *type B* interferometer. This feature, along with the multiple peaks at -14.6, -10.9, -7.5, -6.4, 7.2, 10.9, 13.1 and 14.4μA are of particular interest, as these peaks would be the focal point when measuring the magnetic field dependence.

The most remarkable effects to note from the type C $\frac{dV}{dI}$ are the zero bias minima compared to the zero bias peaks in the other samples, and the particularly high resistance of the *type C* sample in comparison to *type A* device. This can be due to the high resistance of the interfaces; the contributions to these effects are discussed later in the results section.

The value of the bulk resistance and the resistance of the barriers in the normal state is estimated to be approximately 10 Ω and 150 Ω respectively. According to theory [11] both bulk and interface contributions are independent of the superconducting phase difference Φ, between the F/S contacts in the absence of an overlap of superconducting condensate wave functions induced by superconductors on the F side.

The most significant element of this graph are the clear peaks at 5μA. Figure 5.29 demonstrates the oscillatory nature of these peaks when repeating this $\frac{dV}{dI}$ at increments of magnetic field from -78 to 78 μT. The period of these oscillations is made clearer with the magnetoresistance curve provided in figure 5.22, and corresponds to the calculated period of 50 μT, so can be attributed to the coherent transport through the nickel.

The $\frac{dV}{dI}$ for the type D device was recorded from -20 to 20 μA and is shown in figure 5.37, and shows the critical current of the aluminium wires at 11 μA, together with the value of $R_N = 72\Omega$ to give values of $I_c R_N \approx 775\mu V$. The value of the bulk resistance $(\frac{dV}{dI})_F$ and the resistance of the barriers in the normal state $(\frac{dV}{dI})_B$ is estimated to be approximately 10 Ω and 35 Ω respectively. The first feature to note is the extremely large zero bias resistance peak, the magnitude of which is exclusive to this sample. This peak is interestingly similar to the $\frac{dV}{dI}$ curve seen

by Giroud *et al.* [13] discussed in the *background* section, and is explained in the *contributions to observed effects* subsection. The other notable features are the two peaks located at -4.2 and 4.2 μA. These three peaks are particularly important, as these were the main point of interest when measuring magnetic field dependence. The $\frac{dV}{dI}$ was repeated at increments of magnetic field and is shown in figure 5.20, with the peak oscillations made clearer by adjusting the scale in figure 5.21.

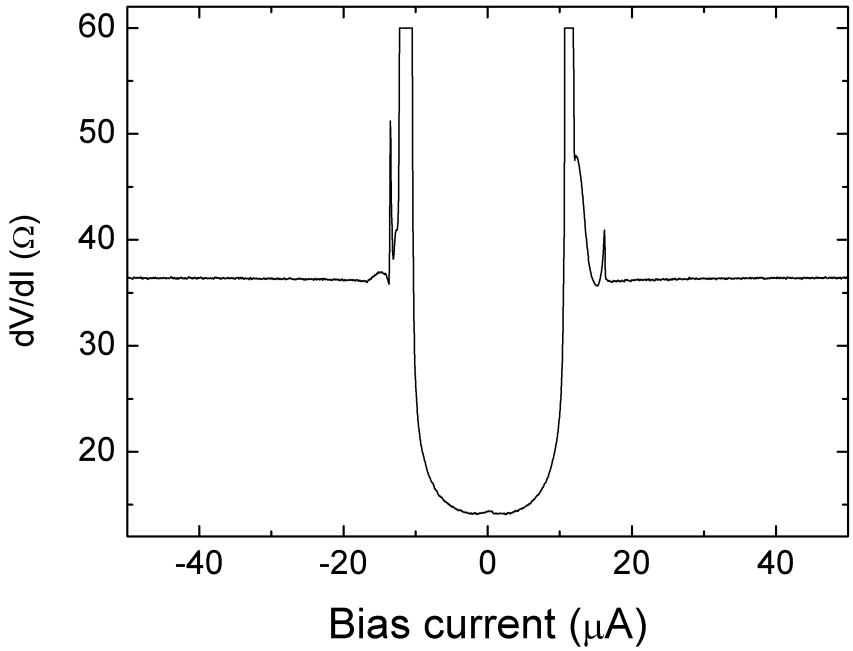

Figure 5.33: Differential resistance curve measured at 240mK, taken from the type A HyQUID using an excitation current of 100nA.

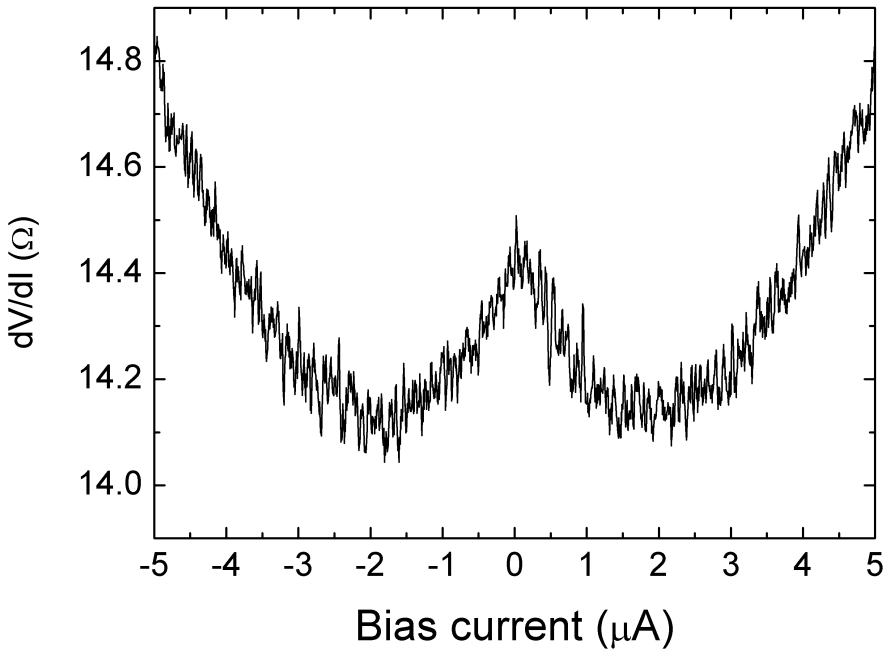

Figure 5.34: Differential resistance of the type A HyQUID highlighting the zero bias peak.

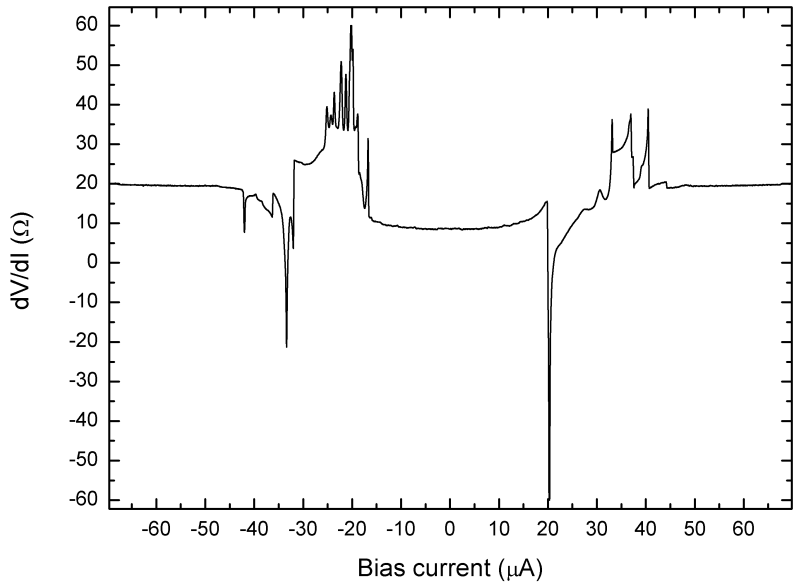

Figure 5.35: Differential resistance of the type B HyQUID from -70 to 70 μA, measured at 240mK.

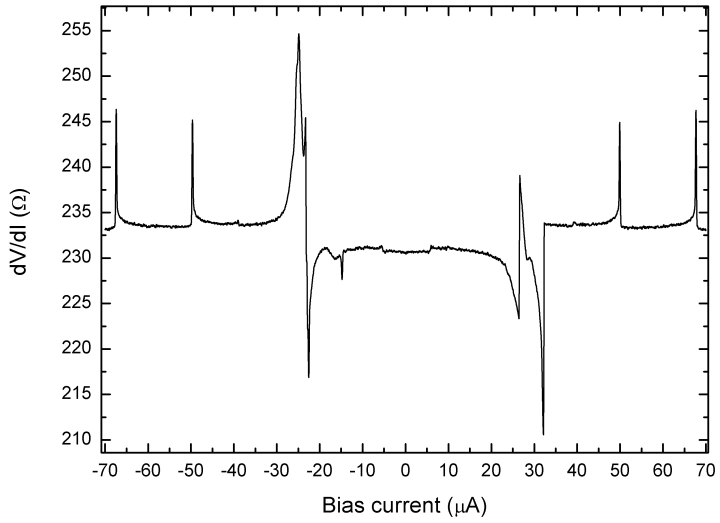

Figure 5.36: Differential resistance of the type C HyQUID taken from -70 to 70 μA, measured at 240mK.

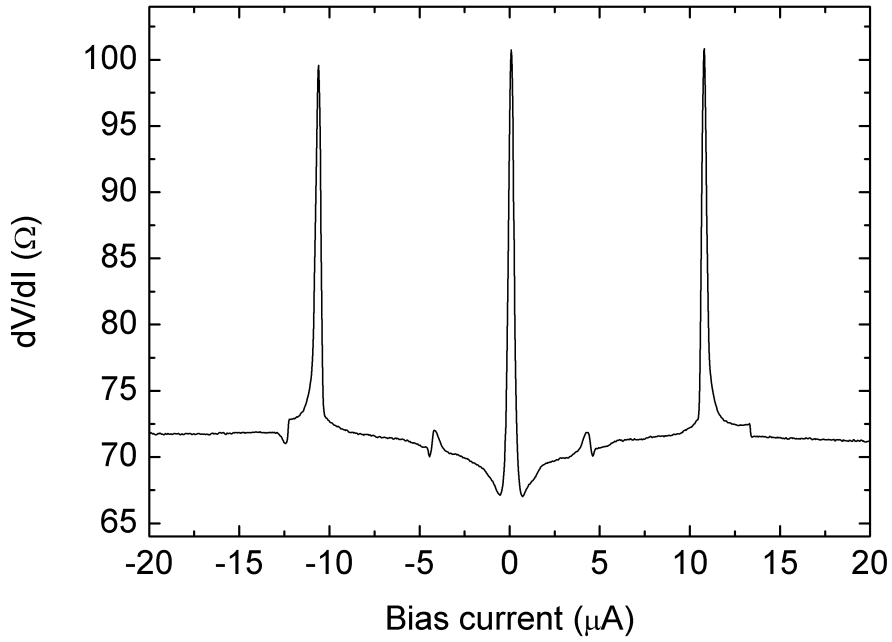

Figure 5.37: Differential resistance of the type D HyQUID measured at 240mK, taken from -20 to 20 μA and revealing an interestingly large zero bias peak.

5.7 Reciprocal proximity effect in SFS structures

The sample fabricated to investigate the reciprocal proximity effect can be seen in figure 5.38, and consists of a nickel disc 1μm in diameter and 30nm thick. Using the multiple evaporation technique described in the *fabrication* section, the aluminium leads 200nm wide and 40nm thick were evaporated onto the disc incorporating a loop area of $39\mu m^2$. It is important to note that the aluminium leads are continuous to ensure no barrier resistance was present within the aluminium. The $\frac{dV}{dI}$ was measured between $\pm 15\mu$A and can be seen in figure 5.39, and highlights three distinct resistances. From the graph, the critical current of the aluminium leads can be seen as 10.5μA, above which showing a normal resistance of 48 Ω. As expected, the resistance is zero at zero bias, however it is important to note the peaks at 0.72 μA, and the resistance above this value of 6.5Ω. This resistance is due to the normal resistance of the T-shaped aluminium covering the disc, which is affected by the underlying nickel. The nickel disc is likely to act as a heat sink due to its adhesion properties to the silicon which would explain the lack of hysteresis within the centre peaks.

Conductance oscillations were then measured in the interferometer formed from the normal T-shaped aluminium and superconducting aluminium loop with the application of the external magnetic field. The central region from figure 5.39 was repeated at 120 increments from -235 to 235 μT and forms the 2D graph shown in figure 5.40. The superconducting gap can be seen to oscillate as a function of phase difference across the normal aluminium; $\Delta \propto |\cos\frac{\varphi}{2}|$ where $\varphi = \frac{2\pi\phi}{\phi_0}$. Magnetoresistance measurements were then taken at zero bias, and at a fixed bias of 1.1μA, which can be seen in figure 5.41 and 5.43 respectively, showing the period of approximately 50μT related to the area of the loop.

Using the sample fabricated for measurements on the reciprocal proximity effect, it is possible to calculate the value the sheet resistance for the aluminium. Using the resistance taken from the $\frac{dV}{dI}$, and measuring the number of squares taken from the design $n_\square$, as $R_\square = R\ n_\square = 0.88\ \Omega/\square$ and using the film thickness of 40nm it is possible to calculate the resistivity as $\rho = R_\square\ t = 3.5 \times 10^{-8}\ \Omega$m. Using this

value for the resistivity, together with the thickness and area of the HyQUID, it is possible to calculate the resistance of the aluminium leads.

The important resistances to consider on the $\frac{dV}{dI}$ include the value above the critical current, and the value at zero bias. The resistance above the critical current, $R = R_{Al} + R_{FN}$ where R_{Al} is the resistance of the aluminium leads and R_{FN} is the resistance of the ferromagnet when the aluminium is in the normal state (The value of R_{FN} consists of the resistance of the SF barrier, $R_{Barrier}$, and the resistance of the bulk ferromagnet, R_{Bulk}, giving $R_{FN} = R_{Barrier} + R_{Bulk}$).

The value for the resistance at zero bias is equal to the resistance of the ferromagnet with the aluminium in the superconducting state; $R = R_{FS}$ (where $R_{FS} = R_{Barrier} = R_{Bulk}$). Using the value for the resistivity above, it is possible to calculate the value of the aluminium leads in the normal state, and therefore make estimates for the value of $\frac{R_{FS}}{R_{FN}}$. Using the values taken from the $\frac{dV}{dI}$ from each HyQUID, the values for $\frac{R_{FS}}{R_{FN}}$ are all greater than 1. These calculations allow comparisons to the results for SF samples using the point contact measurement technique [74].

From the $\frac{dV}{dI}$ in figure 5.39, it is possible to calculate the suppression of the superconducting gap caused by the ferromagnetic disc. As the gap is proportional to the product of the normal resistance and the critical current, then considering both the gap for the aluminium leads; Δ_{Al}, and the gap related to the aluminium covering the ferromagnetic disc; Δ_{Al}^{F}, then it is possible to calculate the suppression of the gap caused by the ferromagnet; $\frac{\Delta_{Al}}{\Delta_{Al}^{F}}$ to be over two orders of magnitude. This large suppression of the gap occurs on the S side with a clean interface, while the high barrier resistance seen on the HyQUID samples prevents the gap suppression. However, the increased barrier resistance suppresses the Andreev reflection, leading to an optimal value for the barrier resistance, and also explains why the samples with low resistance and the preliminary results on samples with a particularly high barrier resistance did not show any oscillations, and the oscillating samples presented in this project had intermediate resistances.

Considering the temperature dependence of the energy gap, a suppression of two orders of magnitude would not be visible at 240mK; the temperatures of the ^3He

cryostat used. It is therefore believed that gapless superconductivity [75] is observed in the aluminium due to the proximity of the ferromagnet. This effect has been investigated in the tunneling behaviour of Pb-Ni sandwiches [76] however this effect deserves further investigation.

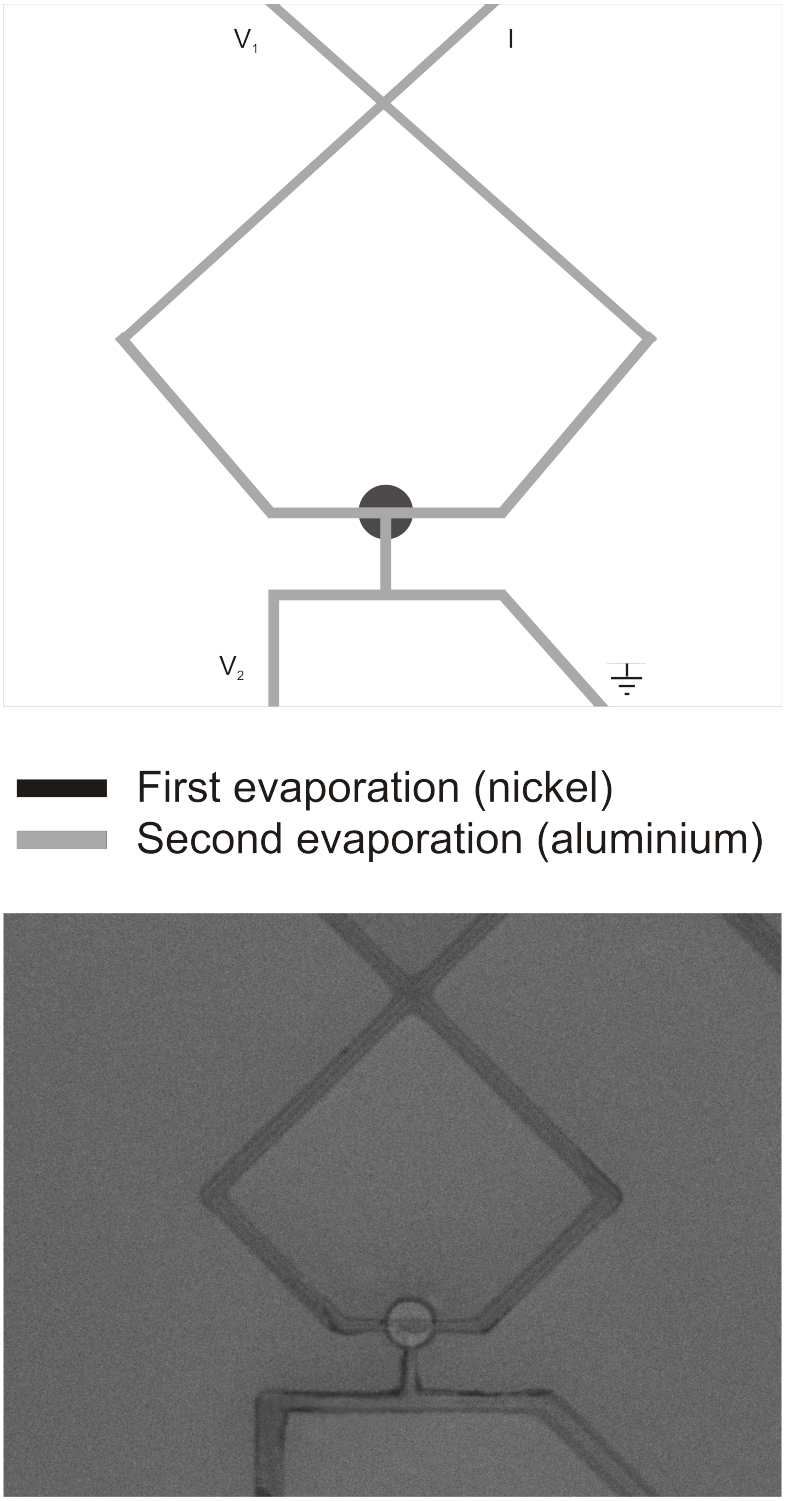

Figure 5.38: Schematic (above) and SEM image (below) of the interferometer used to investigate the reciprocal proximity effect, consisting of a nickel disc 30nm thick under continuous aluminium leads 40nm thick.

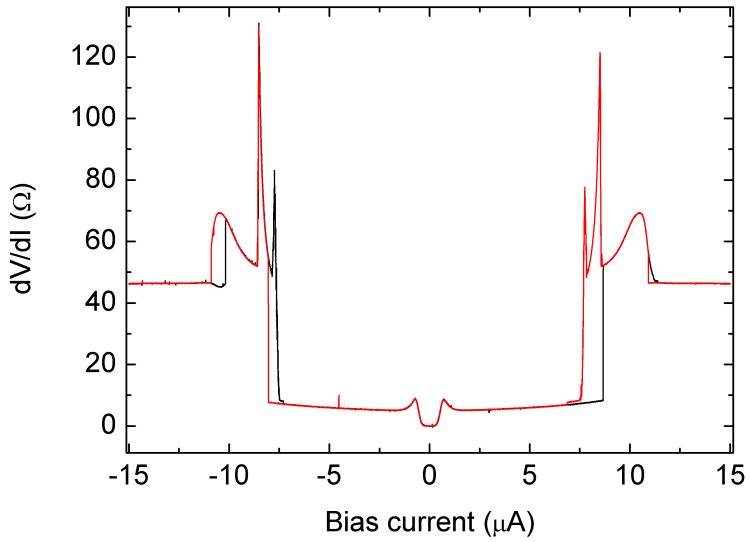

Figure 5.39: $\frac{dV}{dI}$ taken from the sample, showing three distinct resistances; superconducting at zero bias, 6.5Ω above 0.72μA and 48Ω above 10.5μA.

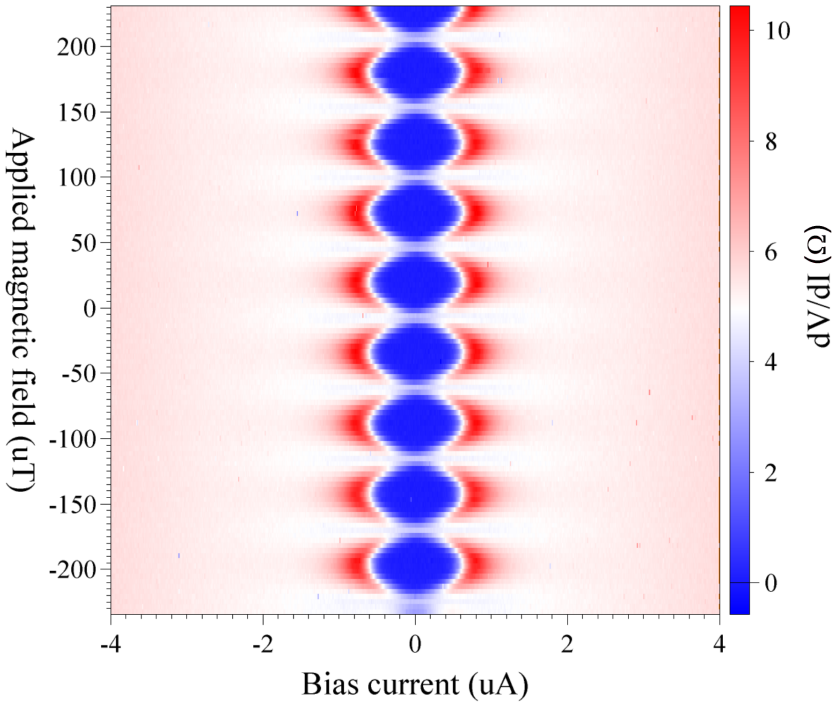

Figure 5.40: Central region from figure 5.39 repeated at increments from -235 to 235μT.

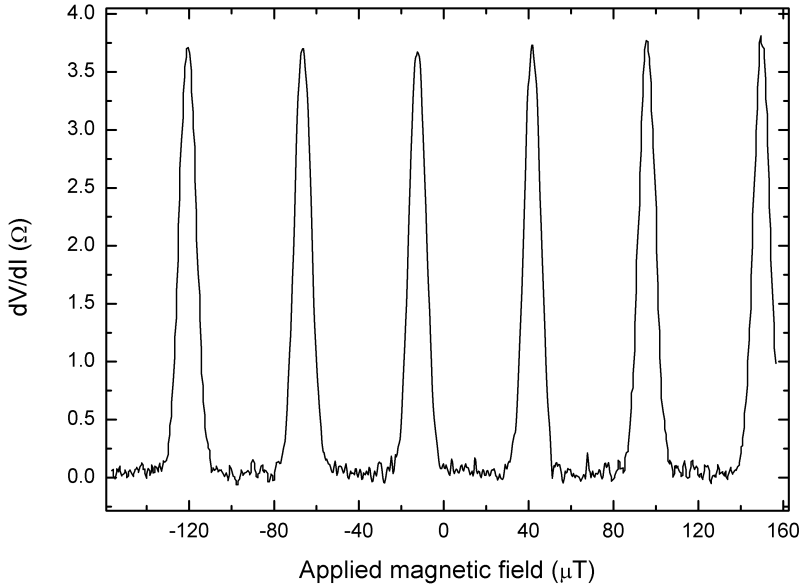

Figure 5.41: Magnetoresistance measurement taken from -156 to 156μT at zero bias.

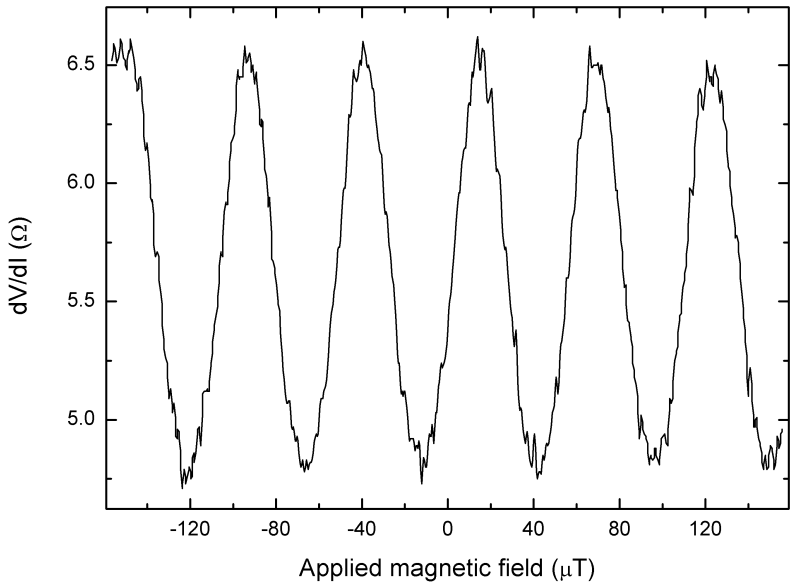

Figure 5.42: Magnetoresistance measurement taken from -156 to 156μT at a fixed bias of 1.1μA.

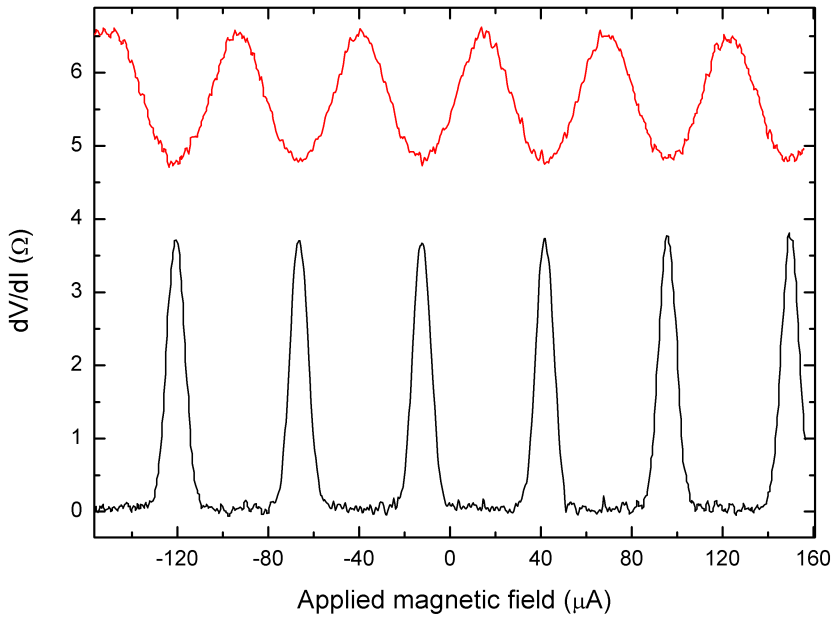

Figure 5.43: Highlighting the phase difference of the magnetoresistance measurements from figure 5.41 (black) and 5.43 (red).

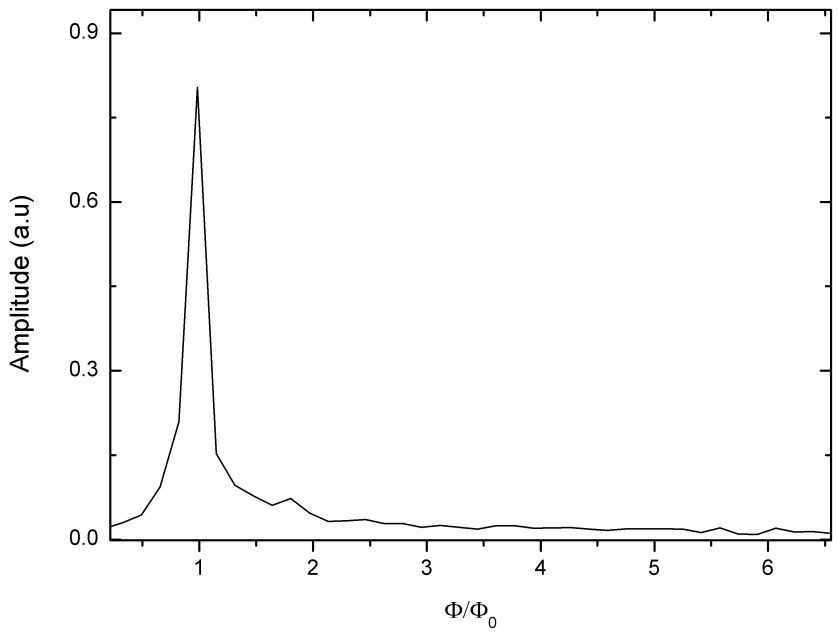

Figure 5.44: Fourier spectrum of the oscillations shown in figure 5.43 confirming the $\frac{h}{2e}$ periodicity

5.8 Discussion of results

The main aim of this thesis was to observe coherent electron transport through a hybrid SFS structure as a result of the long range proximity effect. The evidence for this effect can be seen in the conductance oscillations of the interference device presented in figure 5.16 of the previous subsection. These oscillations measured as a function of phase difference across the ferromagnet with a period relating to the superconducting flux quantum provides unambiguous evidence for the long range proximity effect. By designing the distance between superconducting contacts larger than the ferromagnetic coherence length, this effect can be explained with the presence of the predicted triplet pairs that are insensitive to the exchange field. This is generated in the presence of the inhomogeneity of the magnetisation of the interface. However the condensate function is odd in frequency and even in momentum, and therefore unlike other unconventional condensates is not destroyed by the presence of non-magnetic impurities; surviving much longer distances than the mean free path of the quasiparticles. It is important to compare these oscillations to the oscillations shown in figure 5.43 from the interference device used to measure the reciprocal proximity effect. The reciprocal proximity effect oscillations are clearly caused by the superconducting aluminium placed in contact with the ferromagnet, and by comparing the two interference devices the presence of superconducting pairs within the ferromagnet is evident.

The second important results to take into account, are the comparison of figure 5.29 and figure 5.31 which are identical measurements taken from an interference device before and after the application of an external magnetic field. As discussed in the background section, the magnetisation of the ferromagnetic disc can be changed from the vortex state to the single domain state after applying a magnetic field. As the inhomogeneous magnetisation is critical for the generation of triplet pairs, the oscillations could not survive this change in magnetisation, and these figures clearly shows this is the case.

Some effects proved challenging to explain, for example the varying shapes of each $\frac{dV}{dI}$ curve, and the observation of periodic oscillations given that the resistance was

non-zero, which has been seen in previous SNS structures, however the SFS system is much more complicated. Therefore further contributions need to be considered, including the bulk coherent effects suggested in the *background* section, the effect that arise due to the varying magnetisations of each disc, the non-coherent interface effects, the influence of the vortex core on the penetrating current, and the differences in the fabrication conditions of each sample. Each of these contributions are discussed in more detail below.

5.8.1 Interface effects

The differential resistance $\frac{dV}{dI}$ of the interferometer is a sum of contributions from the three Ni/Al interfaces $\frac{dV}{dI}_B$, and the contribution $\frac{dV}{dI}_F$ from the bulk of the ferromagnetic disc: $\frac{dV}{dI} \approx \frac{dV}{dI}_F + \frac{3}{2}\frac{dV}{dI}_B$.

It is important to note that the resistance of the samples showing oscillations was considerably larger than the majority of the samples with the same geometry that did not show oscillations. It was shown theoretically that most resistance anomalies reported in experiments can be explained by the contribution of the F/S interfaces [54]. In the limit in which the exchange splitting in the ferromagnet is much larger than the superconducting energy gap, it is necessary to consider the transport properties due to the combination of spin accumulation close to the interface, and Andreev reflection at the interface which can lead to either the enhancing or lowering of the resistance.

Considering a superconductor in contact with a material with spin-rotation symmetry such as a normal metal, an incoming electron with spin-up takes another electron with spin-down to form a Cooper pair with zero spin, and is retroreflected as a hole at the interface. Andreev reflection near the Fermi level conserves energy and momentum but does not conserve spin, as the incoming electron and the reflected hole occupy opposite spin bands. The change in spin bands associated with Andreev reflection causes a change in the conductance of SF junctions as the spin-up and spin-down bands are different. Many theoretical studies of Andreev reflection in SF junctions have been considered including [77] that show the transport properties of a SF junction are qualitatively different from the non

ferromagnetic case, as matching the spin polarised current in the ferromagnet to the spinless current in the s-wave superconductor involves the Andreev scattering process, increasing the resistance of the system. It has also been shown by [78] that the additional contact resistance resulting from the superconducting transition is caused by the necessity to match the spin polarised current in the F wire to the spinless current of the superconductor and is comparable to the resistance of a piece of F wire with a length equal to the spin relaxation length.

Direct spin injection was observed in 1985 [79] when a spin current was injected from a ferromagnetic microstructure into an underlying aluminium film, the first to experimentally demonstrate the coupling between electronic charge and spin at an interface between a ferromagnet and a normal metal. As the spin current into a superconductor vanishes at sufficiently low bias and temperature, a non equilibrium spin accumulation builds up on the ferromagnetic side in order to conserve the spin currents. The spin accumulation causes an additional boundary resistance which is of the order of the resistance of the ferromagnetic wire of a length of the spin flip diffusion length. It was shown that a non-equilibrium state of magnetisation due to a current flow of spin polarised electrons leads to a magnetoelectric driving force acting against the applied electric field, giving rise to a spin coupled interface resistance [80], therefore the resistance of the FS system should always be larger than that of the FN system. Investigations into the influence of the non equilibrium spin accumulation on the transport properties of a ferromagnetic single electron transistor found a significant enhancement of the magnetoresistance in the FNF junction [81]. In 2000, another study of the diffusive transport through FNF systems noticed the total conductance changes for different magnetic configurations due to the precession of the spin accumulation in the normal metal [82]. Some effects generated between the combination of spin accumulation and Andreev reflection in diffusive systems were discussed in [83]. They present a description of spin polarised transport in a mesoscopic FS system, showing that the spin reversal associated with Andreev reflection generates an excess spin density close to the interface leading to a spin contact resistance. They found the net spin current that is not allowed to enter the superconductor results

in the spin accumulation in the ferromagnet over a distance that the electron can diffuse before its spin direction is randomised; the spin flip length, λ_{sf}^{F}. Further calculations on the resistance of a diffusive ferromagnetic wire in contact with a superconducting reservoir [54] demonstrate that some of the previous experimental results of [52] and [13] can be understood by discarding the proximity effect, and explain the sign of the resistance change can be caused by the competition between spin accumulation causing the enhanced resistance and Andreev reflection causing the decrease in resistance. As the spin flip length is much larger than the exchange interaction length, they concluded that all coherent correlations in the ferromagnet are expected to be lost so they ignore the effects caused by the proximity effect. An interesting result included the value of the contact resistance that can have a positive or negative sign depending on the relative orientation of the ferromagnetic electrodes.

It was advances in technology that lead to experiments on the proximity effect to be performed on samples on the mesoscopic scale, with lengths smaller than the electron phase-breaking length that allowed significant information to be collected on the Thouless energy E_{Th}; the characteristic energy of the proximity effect and related to the sample length. An interesting effect resulting from the proximity effect is the return of the normal state resistance at low temperature. This reentrance effect on the transport properties near the SN interface has shown that the deviation of the resistance from its normal state value is strongly dependent on temperature and bias voltage. It has been explained that if the electron-electron interaction is negligible, the change in resistance ΔR, at zero voltage will be zero at T=0 [77] [84]. This will then decrease as the temperature is increased until a minimum value at the Thouless temperature $\frac{E_{Th}}{k_B} = \frac{\hbar D}{k_B L^2}$, and then increase to zero at $T >> \frac{\epsilon_c}{k_B}$ [11]. A similar dependence of (V) on bias voltage can be seen in [85]. An experimental study on the diffusive transport near the SN interface showing the reentrance effect as a function of both temperature and voltage can be seen in [71], and the reentrance effect can be seen in the amplitude of magnetoresistance oscillations in an Andreev Interferometer.

Combining the interesting effects found with samples on the mesoscopic scale with

the interest in SF junctions lead to the reentrance effect being observed in ferromagnets adjacent to superconductors [13]. The excess conductance induced by the proximity effect is shown to be a maximum at a temperature or bias voltage equivalent to the Thouless energy. The results from this experiments have already been discussed in figure 2.19 of the *background* section, however it is now necessary to highlight the zero bias peak which is strongly reminiscent of the reentrance effect caused by the proximity effect in the ferromagnet; the size of which showing a remarkable resemblance to the peak measured in figure 5.37.

It is important to note that the reentrance effect was not seen in previous samples with a low transmittance, and it has been shown that if the interface transmittance is low, the probability of Andreev reflection is reduced and the reentrance behaviour in the transport properties is shifted to lower energy scales [86]. This is an important issue to consider, as the size of the interface resistance can clearly play an important role in the effects seen in the resistance measurements.

It is important to note the samples that showed the oscillations had a particularly high resistance. From the SEM images of the measured samples, it can be seen that an increase in resistance can be expected from the geometrically confined leads, however it is also necessary to consider the increased barrier interface resistance. The Blonder-Tinkham-Klapwijk (BTK) model [87] presented an interesting theory in 1982 describing the cross over from metallic to tunnel junction behaviour by including a barrier of arbitrary strength at the interface. This paper, confined to SN junctions presented a unified treatment of both limits of a tunnel junction with a high barrier and a metallic junction with no barrier. It found that the excess current generated by Andreev reflection varies smoothly from the metallic case to zero for the tunnel junction, gaining a detailed insight into the conversion of normal current to supercurrent at the interface. The importance of the interface was considered by expanding the previous work on holmium with observations of spin triplet pairing [1] [17] by using Andreev reflection spectroscopy to study the properties of single S/F interfaces [88]. This paper studies the properties of a single SF interface formed with holmium and niobium to investigate the importance of the interface on the observation of spin triplet pairing. The information was

useful as the nature of the Andreev reflection spectroscopy using the point contact technique offers an ideal probe as the conductance of the contact and the SF interface resistance can be controlled by varying the tip pressure. They find unusual behaviour for the high contact resistance samples, and fit the spectra with a model used in a previous experiment [89] using the BTK equations modified for spin polarisation by Mazin [90]. The most interesting feature to note from their results is a feature also seen with a similar experiment carried out using the point contact Andreev reflection spectroscopy [91]. The zero bias conductance dip is recorded at high contact resistance resulting from a low tip pressure, and suggestions are made that the oxide layers at the surface are magnetic and some processes are suppressed until the oxide is punctured. It is also important to note that the zero bias dips decreased with an increase in tip pressure (decrease in resistance), and the results obtained from this paper also fit very well to the BTK model. It is therefore possible that the zero bias peaks seen in the differential resistance curves of the HyQUID seen in this project could possibly be caused by an oxide layer between S and F layers, which would also contribute to the increase in resistance of some samples.

5.8.2 Effects caused by applying external magnetic field

The resulting change in shape of the $\frac{dV}{dI}$ curve in figures 5.6 and 5.8 lead to the important issue of the suppression of superconductivity caused by the contact of ferromagnet with the superconductor.

The first discussion involves the suppression of the superconductivity in the superconductor caused by the magnetic exchange field from the ferromagnet. This is particularly important when considering the change in the discs' stray field resulting from the single domain state caused by the application and removal of the external magnetic field. Investigations in this area have recently included the control of the critical current in a superconductor by changing the magnetic state of a colossal magnetoresistance ferromagnet on an SF layered structure [92], and reports that the cobalt magnetisation can influence the critical current of a thin film of niobium in a niobium/cobalt bilayer [93]. This paper uses a pair of fer-

romagnetic layers with anti-parallel alignment at low field and parallel alignment at high field. With the anti-parallel alignment, the exchange interaction in the superconductor is reduced, reducing the pair breaking potential resulting in an increased T_c compared to the parallel alignment.

The second discussion involves the effect of the current injected into the superconductor from the ferromagnet, causing an out of equilibrium state of the superconductor; enhancing the quasiparticle density which leads to a depression of the superconducting properties. The density of quasiparticles falls exponentially at a length $l_D = \sqrt{D_Q \tau}$ where τ is the quasiparticle relaxation time and D_Q is the quasiparticle diffusion length. If the injected quasiparticles are spin polarised, the quasiparticle density may be enhanced relative to injection from a non magnetic metal because the spin flip relaxation time τ_S may be long compared with the unpolarised relaxation time τ.

The out of equilibrium configuration caused by spin injection was considered in [94], showing that spin polarised carriers injected into a metallic conductor will lead to a shift $\delta\zeta$ between the chemical potentials of carriers with opposite spins (where $\delta\zeta$ is on the order of $\alpha e E l_D$ where α is the degree of polarisation injection into the superconductor, e is the electron charge, E is the electric field intensity, and l_D is the spin diffusion length). As a result of $\delta\zeta$ there will be a large number of high energy quasiparticle states reducing the superconducting order parameter. The study of spin polarised injection leading to a suppression of the critical current has been investigated, mostly using thin layers of high temperature superconductors due to the low carrier density being more sensitive to quasiparticle injection and colossal magnetoresistance ferromagnets due to the high degree of spin polarisation.

This effect has been investigated in [95] that found the critical current of a superconducting film was strongly suppressed by a current flowing through a ferromagnetic film in the layered structure, caused by pair breaking associated with spin polarised carriers injected into the superconductor. This reduction would not be expected with an unpolarised current, which is confirmed with the control sample that replaced the ferromagnet with a gold layer. The effect of a strong suppression

in supercurrent by the injection of spin-polarised quasiparticles was also investigated by [96] [97]. This also concluded the creation of a local nonequilibrium state suppresses the superconducting order parameter, and the I_c suppression caused by the enhanced pair breaking of the spin polarised quasiparticles from the ferromagnet was an order of magnitude larger than in comparable devices replaced with a normal metal. A similar principle is also discussed in [98], that shows the effect of Joule heating can be neglected by using a pulsed current technique and in-situ thermometry. It has also been suggested that a quantum mechanical approach to investigating the critical current suppression found it was dependent on the polarisation of the injection current, the spin diffusion length in the superconductor, and the insulating barrier strength at the SF interface [99].

It is important to consider results from [100] when investigating the effect from changing the magnetisation of the disc. This paper presented low temperature measurements of spin valves consisting of aluminium and two cobalt injector electrodes placed within the spin diffusion length. From the spin valve signal, it was possible to determine the transition from parallel to anti-parallel alignment of these electrodes. The change in the spin valve voltage was due to the spin accumulation arising at the interfaces, when the spin polarised current in the ferromagnet is converted into a spinless one in the normal metal. They noted that the non equilibrium build up of spins at the interface leads to a difference in the electrochemical potential for the spin up and spin down electrons that decay over the spin relaxation length.

A similar effect was seen in [101], after studying the spin accumulation in an aluminium island with the injection of a spin current from four cobalt electrodes that were connected to the island through transparent tunnel barriers. They were able to control the magnetisation of the individual electrodes by fabricating them with different widths, and exploiting the shape anisotropy when applying an external magnetic field. From the measurement of the amplitude of the spin accumulation, they were able to detect the magnetic configurations of these electrodes, noting that they detect an increase in the signal with an antiparallel configuration compared to the parallel alignment, and identify the spin relaxation length to be 400

±50 nm at low temperature.

5.8.3 Varying magnetic structures

The magnetic structure of the discs with the aid of the MFM images have been discussed in the previous subsection, however the effect of the varying structures on the observation of the long range proximity effect is a vital question to answer. The possible configurations of the disc include the vortex state, the multi domain vortex state, and the single domain. It is important to emphasise the triplet configuration is dependent on the inhomogeneous nature of the disc, being either the vortex or the closure domain configuration. If the disc was therefore in the single domain state the resulting homogeneous S/F/S structure means the differential action of the ferromagnetic exchange field will create a spatially varying phase, resulting in the oscillatory damping of the critical current over a few nanometers and not show any long range coherent effects [18]. If the disc is in the multi domained vortex state, the situation is considered in the same way as if in the vortex state with the same outcome. The presence of a domain wall does not effect, and is even used to help explain the long range effect, for example by Kadigrobov *et al.* [16], and does not alter the underlying physics of the formation of triplet pairs. With this formation however, the position of the domain walls relative to the superconducting contacts could help explain the reproducibility of the results.

The magnetic structure of mesoscopic ferromagnets is heavily dependent on geometry. The disc in sample four shown in figure 5.15 is not perfectly round, comprising of a flat edge caused by the excess resist remaining on the germanium before evaporating. This is therefore likely to define the location of the domain walls, the placement of which relative to the superconducting leads could prove to be a major contributing factor as discussed above.

Dubonos *et al.* [102] report a change in magnetisation with the onset of superconductivity on studies of SF structures. They describe the effect due to the movement of domains within the ferromagnet caused by the screening of the domains stray fields by the superconductor. This was investigated with the use of a Hall probe to observe changes in the magnetic field around the submicron struc-

tures, and suggested this would cause the change in resistance changes in previous electron transport measurements [51] as this depends on the local direction of magnetisation with respect to the measuring electrical current leading to anisotropic magnetoresistance (AMR).

Previous results on SF structures were then repeated and published in [103] that establish the changes in resistance was not due to a redistribution of magnetic domains. This was achieved by ensuring that the measuring current did not pass through the SF interface, and by noting that the magnitude of the observed effects was more than an order of magnitude larger than the effect of AMR. This was then extended by choosing a superconductor with a higher critical field, and observing this large effect even when the ferromagnet is magnetised uniformly with the absence of domain walls. This therefore lead to the conclusion that the long range triplet pair correlations generated at the SF interface is the most likely explanation for this increased conductance in the previous electron transport measurements.

Chapter 6

Conclusion and future direction

The main aim of this project was to provide an experimental study of the superconducting proximity effect in ferromagnetic disc-shaped mesoscopic conductors in search for superconducting phase-coherent electron transport caused by the inhomogeneous magnetisation of the ferromagnetic disc.

This work is part of an international effort to observe long range penetration of superconductivity into strong ferromagnetic conductors ignited by theoretical investigations that suggested magnetic inhomogeneities at the interface will generate triplet pairs that are insensitive to the exchange field and elastic electron scattering at defects and impurities. These pairs are able to penetrate into the ferromagnet up to the thermal coherence length ξ_T, which is orders of magnitude larger than the ferromagnetic coherence length ξ_F.

Previous experiments on this subject have all been differentiated by their varying magnetic inhomogeneities. This project is the first to investigate strong mesoscopic ferromagnets in the search for the long range proximity effect, using nickel discs that have been nano-engineered using modern lithographic techniques. Due to the competition between the magnetostatic and quantum mechanical exchange interaction, the ground state magnetisation of the discs is the magnetically inhomogeneous vortex.

The pioneering results of this project feature a flux biased interference device, where conduction oscillations measured as a function of phase difference across a ferromagnet with a period relating to the superconducting flux quantum provides

unambiguous evidence of the long range proximity effect. By choosing the distance between the superconducting contacts to be much larger than the singlet order parameter penetration depth, and by analysing the results taken after changing the magnetic structure of the disc, it is possible to discard the conventional proximity effect and conclusively explain the oscillations as due to the long-range penetration of the triplet component that is generated in the presence of the inhomogeneous magnetisation. One of the major advantages of this system is that coherent transport can be observed at distances larger than the thermal coherence length, as long as the separation between the superconducting leads remains shorter than the phase breaking length.

An important technological advance involving the fabrication of the SFS systems was derived in this project. Many challenging problems including the alignment of the disc between the superconducting leads, the interface resistance between the superconductor and the ferromagnet, and the stray field from the excess material were overcome with the development of an improved shadow evaporation technique. This unique solution incorporated a thin germanium layer which allowed the re-exposure of selected areas that generates a very controlled undercut; eliminating all the stray field from the nearby areas.

Further experiments should be undertaken to ensure a clearer understanding of a variety of contributions to the effects observed, including the varying magnetic structure of the disc, the placement of the domain walls relative to the superconducting contacts, and the contributions of the interface resistances on the observation of the oscillations. A step in this direction has already been made by the group at Royal Holloway that has taken advantage of the strong geometric dependence of domain wall placement in mesoscopic magnets by using a triangular shape ferromagnet instead of a circular disc. This can force three domain walls to the three vertices of the triangle and the lead placement can be arranged accordingly. A similar effect could be achieved by varying the ferromagnetic structure in the HyQUID of similar design, for example using a ferromagnetic anti-vortex seen in nickel crosses. One of the main benefits of using the type of mesoscopic magnets used in this project is the ability to control the magnetic structure of

the ferromagnet, and to compare the results after changing the magnetisation. As the magnetic structure of the disc can be altered using a smaller magnetic field if it is applied in plane, it would be useful to optimise the experimental setup to incorporate a parallel magnetic field, allowing a homogeneous state to be achieved below the critical field of aluminium. This ability will provide a much clearer understanding of the theoretical models suggested, which has not been possible with some of the previous experiments.

Simple improvements include the use of a high purity nickel to increase the mean free path, and carrying out the measurements at lower temperature. Steps for both of these improvements have already been implemented and show great potential. The theoretical calculations have shown that the coherence length of the ferromagnet is dependent on the temperature of the sample, and the lower temperatures of a dilution refrigerator may even lead to the observation of the critical current. It would also be beneficial to extend the research into the phase periodic reentrance into the superconducting state from the gapless superconductor, and to fully investigate the nature of the interface transparency between the superconductor and the ferromagnet, which could be achieved with further development of the fabrication process.

The work carried out in this thesis has built on previous knowledge and progressed this fast growing subject. By applying the few suggested amendments, a more detailed understanding of the physics of the long range proximity effect can be attained. Some of these are already in progress, and I look forward to these results with eager anticipation.

Bibliography

[1] Sosnin, I., Cho, H., Petrashov, V. T., and Volkov, A. F. *Phys. Rev. Lett.* **96**, 157002 (2006).

[2] Keizer, R. S., Goennenwein, S. T. B., Klapwijk, T. M., Miao, G., Xiao, G., and Gupta, A. *Nature* **439**(7078), 825–827 (2006).

[3] Wachowiak, A., Wiebe, J., Bode, M., Pietzsch, O., Morgenstern, M., and Wiesendanger, R. *Science* **298**(5593), 577–580 (2002).

[4] Shinjo, T., Okuno, T., Hassdorf, R., Shigeto, . K., and Ono, T. *Science* **289**(5481), 930–932 (2000).

[5] Mironov, V. L., Ermolaeva, O. L., Gusev, S. A., Klimov, A. Y., Rogov, V. V., Gribkov, B. A., Udalov, O. G., Fraerman, A. A., Marsh, R., Checkley, C., Shaikhaidarov, R., and Petrashov, V. T. *Phys. Rev. B* **81**, 094436 Mar (2010).

[6] Rose-Innes, A. and Rhoderick, E. *Introduction to superconductivity*. Pergamon Press, (1978).

[7] Checkley, C. *Andreev Interferometry of Flux Qubits Driven By Radio Frequency Field*. PhD thesis, Royal Holloway, University of London, (2009).

[8] Petrashov, V. T., Antonov, V. N., Delsing, P., and Claeson, R. *Phys. Rev. Lett.* **70**, 347–350 Jan (1993).

[9] Petrashov, V. T., Antonov, V. N., Delsing, P., and Claeson, T. *JETP Lett.* **60**, 589–594 (1994).

[10] Petrashov, V. T., Antonov, V. N., Delsing, P., and Claeson, T. *Phys. Rev. Lett.* **74**, 5268–5271 (1995).

[11] Nazarov, Y. V. and Stoof, T. H. *Phys. Rev. Lett.* **76**, 823–826 Jan (1996).

[12] Eschrig, M. *Physics Today* **64**, 43 (2011).

[13] Giroud, M., Courtois, H., Hasselbach, K., Mailly, D., and Pannetier, B. *Phys. Rev. B* **58**, R11872–R11875 (1998).

[14] Bergeret, F. S., Volkov, A. F., and Efetov, K. B. *Phys. Rev. Lett.* **86**, 4096–4099 (2001).

[15] Houzet, M. and Buzdin, A. I. *Phys. Rev. B* **76**, 060504 (2007).

[16] Kadigrobov, A., Shekhter, R. I., and Jonson, M. *Europhysics Letters* **54**(3), 394 (2001).

[17] Robinson, J. W. A., Witt, J. D. S., and Blamire, M. G. *Science* **329**(5987), 59–61 (2010).

[18] Robinson, J. W. A., Barber, Z. H., and Blamire, M. G. *Appl. Phys. Lett.* **95**, 192509 (2009).

[19] Khaire, T. S., Khasawneh, M. A., Pratt, W. P., and Birge, N. O. *Phys. Rev. Lett.* **104**, 137002 (2010).

[20] Visani, C., Sefrioui, Z., Tornos, J., Leon, C., Briatico, J., Bibes, M., Barthelemy, A., Santamaria, J., and Villegas, J. E. *Nature Physics* **8**, 539543 (2012).

[21] Kalenkov, M. S., Zaikin, A. D., and Petrashov, V. T. *Phys. Rev. Lett.* **107**, 087003 Aug (2011).

[22] Bader, S. D. *Rev. Mod. Phys.* **78**, 1–15 Jan (2006).

[23] Kim, D.-H., Rozhkova, E. A., Ulasov, I. V., Bader, S. D., Rajh, T., Lesniak, M. S., and Novosad, V. *Nature Materials* **9**, 165171 (2009).

[24] Bardeen, J., Cooper, L. N., and Schrieffer, J. R. *Phys. Rev.* **106**, 162–164 Apr (1957).

[25] Bardeen, J., Cooper, L. N., and Schrieffer, J. R. *Phys. Rev.* **108**, 1175–1204 Dec (1957).

[26] Blundell, S. *Magnetism in condensed matter.* Oxford University Press, (2001).

[27] Bleaney, B. I. and Bleaney, B. *Electricity and Magnetism.* Oxford University Press, (1976).

[28] Bitter, F. *Phys. Rev.* **41**, 507–528 (1932).

[29] Tejada, J., Chudnovsky, E. M., del Barco, E., Hernandez, J. M., and Spiller, T. P. *Nanotechnology* **12**(2), 181 (2001).

[30] Eschrig, M., Kopu, J., Cuevas, J. C., and Schön, G. *Phys. Rev. Lett.* **90**, 137003 (2003).

[31] Ana-Vanessa Jausovec, G. X. and Cowburn, R. P. *Appl. Phys. Lett.* **88**(052501) (2006).

[32] Voltairas, P., Fotiadis, D., and Massalas, C. *Journal of Magnetism and Magnetic Materials* **217**(13) (2000).

[33] Metlov, K. L. and Guslienko, K. Y. *arXiv:cond-mat/0110037v1* (2008).

[34] Guslienko, K. Y. and Novosad, V. *J. Appl. Phys.* **96** (2004).

[35] Cowburn, R. P., Koltsov, D. K., Adeyeye, A. O., Welland, M. E., and Tricker, D. M. *Phys. Rev. Lett.* **83**, 1042–1045 Aug (1999).

[36] A. Lebib, S. P. Li, M. N. and Chen, Y. *J. Appl. Phys.* **89**(3892) (2001).

[37] Ross, C. A., Hwang, M., Shima, M., Cheng, J. Y., Farhoud, M., Savas, T. A., Smith, H. I., Schwarzacher, W., Ross, F. M., Redjdal, M., and Humphrey, F. B. *Phys. Rev. B* **65**, 144417 Mar (2002).

[38] Fraerman, A. A. and Udalov, O. G. *Phys. Rev. B* **77**, 094401 Mar (2008).

[39] Bruno, P., Dugaev, V. K., and Taillefumier, M. *Phys. Rev. Lett.* **93**, 096806 Aug (2004).

[40] Neubauer, A., Pfleiderer, C., Binz, B., Rosch, A., Ritz, R., Niklowitz, P. G., and Böni, P. *Phys. Rev. Lett.* **102**, 186602 May (2009).

[41] *http://math.nist.gov/oommf/.*

[42] de Gennes, P. G. *Rev. Mod. Phys.* **36**, 225–237 (1964).

[43] Annett, J. F. *Superconductivity, Superfluids and Condensates*. Oxford University Press, (2003).

[44] Andreev, A. F. *JETP* **19**, 1228 (1964).

[45] Fulde, P. and Ferrell, R. A. *Phys. Rev.* **135**, A550–A563 Aug (1964).

[46] Larkin, A. I. and Ovchinnikov, Y. N. *J. Exptl. Theoret. Phys. (U.S.S.R)* **20**, 1136–1146 (1964).

[47] A.I. Buzdin, L. B. and Panyukov, S. *JETP Lett.* **35**, 178–180 (1982).

[48] Demler, E. A., Arnold, G. B., and Beasley, M. R. *Phys. Rev. B* **55**, 15174–15182 Jun (1997).

[49] Kontos, T., Aprili, M., Lesueur, J., and Grison, X. *Phys. Rev. Lett.* **86**, 304–307 Jan (2001).

[50] Blum, Y., Tsukernik, A., Karpovski, M., and Palevski, A. *Phys. Rev. Lett.* **89**, 187004 Oct (2002).

[51] Petrashov, V. T., Antonov, V. N., Maksimov, S. V., and Shalkhaldarov, R. S. *JETP* **59**, 551 (1994).

[52] Petrashov, V. T., Sosnin, I. A., Cox, I., Parsons, A., and Troadec, C. *Phys. Rev. Lett.* **83**, 3281–3284 (1999).

[53] Aumentado, J. and Chandrasekhar, V. *Phys. Rev. B* **64**, 054505 (2001).

[54] Belzig, W., Brataas, A., Nazarov, Y. V., and Bauer, G. E. W. *Phys. Rev. B* **62**, 9726–9739 (2000).

[55] Volkov, A. F., Bergeret, F. S., and Efetov, K. B. *Phys. Rev. Lett.* **90**, 117006 (2003).

[56] Petrashov, V. T., Sosnin, I. A., Cox, I., Parsons, A., and Troadec, C. *Journal of Low Temperature Physics* **118**, 689–698 (2000).

[57] Bergeret, F. S., Volkov, A. F., and Efetov, K. B. *Rev. Mod. Phys.* **77**, 1321–1373 (2005).

[58] Eschrig, M. and Lofwander, T. *Nat Phys* **4**, 138–143 (2008).

[59] Ryazanov, V. V., Oboznov, V. A., Rusanov, A. Y., Veretennikov, A. V., Golubov, A. A., and Aarts, J. *Phys. Rev. Lett.* **86**, 2427–2430 Mar (2001).

[60] Khasawneh, M. A., Pratt, W. P., and Birge, N. O. *Phys. Rev. B* **80**, 020506 (2009).

[61] Tomasch, W. J. *Phys. Rev. Lett.* **16**, 16–19 (1966).

[62] McMillan, W. L. and Anderson, P. W. *Phys. Rev. Lett.* **16**, 85–87 (1966).

[63] Rowell, J. M. and McMillan, W. L. *Phys. Rev. Lett.* **16**, 453–456 (1966).

[64] Rowell, J. M. *Phys. Rev. Lett.* **30**, 167–170 (1973).

[65] Dolan, G. J. *Appl. Phys. Lett.* **31**, 337 (1977).

[66] Ana-Vanessa Jausovec, G. X. and Cowburn, R. P. *Appl. Phys. Lett.* **88**(052501) (2006).

[67] Waeyenberge, B. V., Puzic, A., Stoll, H., Chou, K. W., Tyliszczak, T., Hertel, R., Fahnle, M., Bruckl, H., Rott, K., Reiss, G., Neudecker, I., Weiss, D., Back, C. H., and Schutz, G. *Nature* **444**, 461–464 (2006).

[68] Guslienko, K. Y., Han, X. F., Keavney, D. J., Divan, R., and Bader, S. D. *Phys. Rev. Lett.* **96**, 067205 Feb (2006).

[69] Yamada, K., Kasai, S., Nakatani, Y., Kobayashi, K., Kohno, H., Thiaville, A., and Ono, T. *Nature Materials* **6**, 270–273 (2007).

[70] Scholz, W., Guslienko, K., Novosad, V., Suess, D., Schrefl, T., Chantrell, R., and Fidler, J. *Journal of Magnetism and Magnetic Materials* **266**(12), 155 – 163 (2003).

[71] Charlat, P., Courtois, H., Gandit, P., Mailly, D., Volkov, A. F., and Pannetier, B. *Phys. Rev. Lett.* **77**, 4950–4953 Dec (1996).

[72] Lambert, C. J. and Raimondi, R. *Journal of Physics: Condensed Matter* **10**(5), 901 (1998).

[73] R. Vijay, E. M. Levenson-Falk, D. H. S. I. S. *arXiv:1005.1110v1* (2010).

[74] Soulen, R. J., Byers, J. M., Osofsky, M. S., Nadgorny, B., Ambrose, T., Cheng, S. F., Broussard, P. R., Tanaka, C. T., Nowak, J., Moodera, J. S., Barry, A., and Coey, J. M. D. *Science* **282**(5386), 85–88 (1998).

[75] Abrikosov, A. *Fundamentals of the Theory of Metals*. Elsevier Science Ltd, (1988).

[76] Hauser, J. J. *Phys. Rev.* **164**, 558–565 (1967).

[77] Beenakker, C. W. J. *Phys. Rev. B* **46**, 12841–12844 Nov (1992).

[78] Falko, V., Lambert, C., and Volkov, A. *JETP Letters* **69**, 532–538 (1999).

[79] Johnson, M. and Silsbee, R. H. *Phys. Rev. Lett.* **55**, 1790–1793 (1985).

[80] Gijs, M. A. and Bauer, G. E. *Advances in Physics* **46**(3-4), 285–445 (1997).

[81] Brataas, A., Nazarov, Y. V., Inoue, J., and Bauer, G. E. W. *Phys. Rev. B* **59**, 93–96 Jan (1999).

[82] Huertas Hernando, D., Nazarov, Y. V., Brataas, A., and Bauer, G. E. W. *Phys. Rev. B* **62**, 5700–5712 Sep (2000).

[83] Jedema, F. J., van Wees, B. J., Hoving, B. H., Filip, A. T., and Klapwijk, T. M. *Phys. Rev. B* **60**, 16549–16552 Dec (1999).

[84] Lambert, C. J. *Journal of Physics: Condensed Matter* **3**(34), 6579 (1991).

[85] Volkov, A., Allsopp, N., and Lambert, C. J. *Journal of Physics: Condensed Matter* **8**(4), L45 (1996).

[86] Yip, S. *Phys. Rev. B* **52**, 15504–15508 Dec (1995).

[87] Blonder, G. E., Tinkham, M., and Klapwijk, T. M. *Phys. Rev. B* **25**, 4515–4532 (1982).

[88] Usman, I. T. M., Yates, K. A., Moore, J. D., Morrison, K., Pecharsky, V. K., Gschneidner, K. A., Verhagen, T., Aarts, J., Zverev, V. I., Robinson, J. W. A., Witt, J. D. S., Blamire, M. G., and Cohen, L. F. *Phys. Rev. B* **83**, 144518 Apr (2011).

[89] Bugoslavsky, Y., Miyoshi, Y., Clowes, S. K., Branford, W. R., Lake, M., Brown, I., Caplin, A. D., and Cohen, L. F. *Phys. Rev. B* **71**, 104523 Mar (2005).

[90] I. I. Mazin, A. A. G. and Nadgorny, B. *Journal of Applied Physics* **89** (2001).

[91] Yates, K. A., Cohen, L. F., Ren, Z.-A., Yang, J., Lu, W., Dong, X.-L., and Zhao, Z.-X. *Superconductor Science and Technology* **21**(9), 092003 (2008).

[92] Allsworth, M., Chakalov, R., Mikheenko, P., Colclough, M., and Muirhead, C. *Applied Superconductivity, IEEE Transactions on* **13**(2), 2849 – 2852 june (2003).

[93] Kinsey, R., Burnell, G., and Blamire, M. *Applied Superconductivity, IEEE Transactions on* **11**(1), 904 –907 mar (2001).

[94] Aronov, A. G. *Journal of Experimental and Theoretical Physics Letters* **24**, 32 Aug (1976).

[95] Vas'ko, V. A., Larkin, V. A., Kraus, P. A., Nikolaev, K. R., Grupp, D. E., Nordman, C. A., and Goldman, A. M. *Phys. Rev. Lett.* **78**, 1134–1137 Feb (1997).

[96] Dong, Z. W., Ramesh, R., Venkatesan, T., Johnson, M., Chen, Z. Y., Pai, S. P., Talyansky, V., Sharma, R. P., Shreekala, R., Lobb, C. J., , and Greene, R. L. *Appl. Phys. Lett* **71** Feb (1997).

[97] Lee, K., Wang, W., Iguchi, I., Friedman, B., Ishibashi, T., and Sato, K. *Appl. Phys. Lett.* **75**, 1149 (1999).

[98] Yeh, N.-C., Vasquez, R. P., Fu, C. C., Samoilov, A. V., Li, Y., and Vakili, K. *Phys. Rev. B* **60**, 10522–10526 Oct (1999).

[99] Sun, G., Zheng, Z., Xing, D. Y., Dong, J., and Wang, Z. D. *Journal of Physics: Condensed Matter* **13**(4), 627 (2001).

[100] Zou, J., Sosnin, I., and Petrashov, V. T. *Appl. Phys. Lett.* **89**, 023505 Oct (2006).

[101] Costache, M. V., Zaffalon, M., and van Wees, B. J. *Phys. Rev. B* **74**, 012412 Jul (2006).

[102] Dubonos, S. V., Geim, A. K., Novoselov, K. S., and Grigorieva, I. V. *Phys. Rev. B* **65**, 220513 (2002).

[103] Nugent, P., Sosnin, I., and Petrashov, V. T. *Journal of Physics: Condensed Matter* **16**(49), L509 (2004).